Centro Brasileiro de Pesquisas Físicas

DOCTORAL THESIS

Astrid Carolina Pereyra Alí

Growth and doping of Mn_xO_y thin films on copper (111)

Supervisor: Prof. Dr. Fernando Stavale

Study programme: Physics

Rio de Janeiro 2022

CBPF
Centro Brasileiro de Pesquisas Físicas
UNIDADE DE PESQUISA DO MCTIC

MINISTÉRIO DA
CIÊNCIA, TECNOLOGIA,
INOVAÇÕES E COMUNICAÇÕES

PÁTRIA AMADA
BRASIL
GOVERNO FEDERAL

"GROWTH AND DOPING OF MnxOy THIN FILMS ON COPPER (111)"

ASTRID CAROLINA PEREYRA ALÍ

Tese de Doutorado em Física apresentada no Centro Brasileiro de Pesquisas Físicas do Ministério da Ciência Tecnologia e Inovação. Fazendo parte da banca examinadora os seguintes professores:

Fernando Loureiro Stavale Junior – Presidente/Orientador/CBPF

Abner de Siervo - UNICAMP

BArchanjo

Braulio Soares Archanjo - INMETRO

Edmar Avellar Soares - UFMG

Luiz Carlos Sampaio Lima – CBPF

Rio de Janeiro, 20 de maio de 2022.

Centro Brasileiro de Pesquisas Físicas
Rua Doutor Xavier Sigaud, 150, URCA, Rio de Janeiro, Brasil
Tel.: +55 21 2141-7100 CEP:22290-180
http://www.cbpf.br

AUTHOR'S DECLARATION

I declare that the work in this dissertation was carried out in accordance with the requirements of the Brazilian Center for Research in Physics degree program. Except where indicated by specific reference in the text, the work is the candidate's own work. Work done in collaboration with, or with the assistance of, others, is indicated as such. Any views expressed in the dissertation are those of the author.

SIGNED: .... DATE: ....

DEDICATION AND ACKNOWLEDGEMENTS

I am dedicating this thesis to God for taking care of my family and friends. For all the blessings He has given me and for allowing me to fulfill my dreams. My life is always in his hands.

I also dedicate this work to my beloved family who have meant and continue to mean so much to me. To my mother Bonnie and my father Juan whose love for me knew no bounds and, who taught me the value of hard work. To my brother Juan Carlos, who makes me laugh with his "bad" jokes. I am grateful for all the love and understanding they give me and I will always cherish that feeling. Also to all my pets: Lobo (†), Thomas (†), Noona (†), Mamut (†), Scott (†), Lassie (†), Lita, Lila and Negrita. I will never forget you.

To my supervisor Dr. Fernando Stavale for his guidance and all support in this work. For his patience and the opportunity to teach me in all these years. Thanks a lot.

To Dr. Emilia Annese for all her guidance and teachings in the initial part of this thesis.

To CBPF professors for the knowledge transmitted in the subjects. To Brazil government for funding the CAPES scholarship and to CBPF for supporting the development of this work. Especially to Dr. Alexandre Mello de Paula Silva for the availability of equipment of the LabSurf.

To Denise Toledo for being a great mentor and friend when I needed help the most.

To MereLuce Sales for being the way she is. For giving me good advices, her help and friendship. And for the opportunity to know the girls "Nicolle and Fanny". May God bless you always.

To my colleagues from the Laboratory 112-D. Especially Pablo, Guilherme, Rubem, Jade, Bianca for their help and support.

To Cynthia, Marco and John for the friendship we have despite the years.

To my friends from "Agoraios" because talking to you is always pleasant at all times. I never stop laughing.

And finally I want to thank SHINee for being one of the pillars of my life. Because I am never alone when I listen to them. I always support you: Onew, Jonghyun, Key, Minho and Taemin. SHINee fighting!

ABSTRACT

Manganese plays a fundamental role in photosynthesis because it contributes with Mn^{2+} in the critical redox reaction of the water-oxidizing complex [1]. To work as reducing agent the manganese has to assume its oxidized form [2]. In particular, in photosynthesis an important role is played by cluster of calcium doped manganese oxide (Mn-Ca-O) that provides electrons for the reaction or assists the light harvesting [3]. To tune the manganese oxide electronic properties we may play with its crystallographic structure or reduce it to nanoparticles and thin film. In this study, we are interested on prepare well-defined manganese oxide surface and modulated their electronic and structural properties by cobalt doping.

To this end, we fabricated manganese oxide thin films on oriented metallic substrate (copper) by depositing Mn using e-beam evaporation (EBE) technique and varying growth parameters such as partial oxygen pressure, $p(O_2)$, and thickness. The electronic properties were investigated by X-ray and Ultraviolet photoelectron (XPS/UPS), X-ray absorption (XA) and Resonant Photoemission (ResPE) spectroscopies. The crystallographic structures were established by Low energy electron diffraction (LEED) and the morphology was probed by Atomic force (AFM).

Among manganese oxides, a special role is played by Mn_3O_4 and MnO films deposited on metallic substrates to avoid their insulating nature. Both Mn_xO_y are obtained in particular growth conditions: deposition and post-annealing at the same $p(O_2)$: $\sim 5 \times 10^{-7}$ and $\sim 5 \times 10^{-8}$ mbar to for Mn_3O_4 and MnO, respectively.

XPS/UPS measurements were made to find the oxidation state and verify the formation of different Mn_xO_y. Mn_3O_4 and MnO on Cu(111) organizes in different structures depending on the film thickness as observed by LEED.

The results of Mn_3O_4 films doped with cobalt were obtained in a different substrate - Au(111). We opted to use Au instead Cu surface because of binding energy overlap between O *KLL* and Co $2p$ core-level photoemission. We explored different conditions to obtain the doped system, until similar LEED features (to pure Mn_3O_4) were found. The thin films were prepared by depositing alternating layers of Mn_xO_y, Mn and Co. This recipe is crucial to the development of the doped system because upon the doping, our results suggest that the inclusion of Co in the thin film does not change its electronic and crystallographic structures. XAS and ResPES measurements were performed in PGM beamline in the *Laboratório Nacional de Luz Síncrotron (LNLS)*, Campinas, Brazil.

Keywords: thin films, MnO, Mn_3O_4, electronic properties, crystallographic structure, dopant.

RESUMO

O papel desempenhado por íons Mn^{2+} na reação de redução do complexo oxidante da água faz com que o manganês tenha um papel fundamental na fotossíntese [1]. Neste processo, o papel redutor do manganês leva a formação do oxido de manganês [2].

Estruturas dopadas também são de interesse na fotossíntese, por exemplo o papel desempenhado por clusters de óxido de manganês dopados com cálcio (Mn-Ca-O) que fornecem elétrons para a recão e que favorecem na captação de luz solar [3].

As propriedades eletrônicas do óxido de manganês podem ser modificadas alterando sua estrutura cristalográfica ou reduzindo sua dimensionalidade (nanopartículas e filmes finos). Neste estudo, estamos interessados em preparar superfícies de óxido de manganês bem definida e modular sua estrutura eletrônica bem como propriedades estruturais através da dopagem com cobalto.

Para este fim, fabricamos filmes finos de óxido de manganês sobre um substrato metálico orientado (cobre) depositando Mn, usando a técnica de evaporação de feixe de elétrons (EBE) e variando os parâmetros de crescimento como pressão parcial de oxigênio, p(O2) e espessura do filme. As propriedades eletrônicas foram investigadas por diferentes espectroscopias: fotoelétrons por raios X e luz ultravioleta (XPS/UPS), absorção de raios X (XAS) e a fotoemissão ressonante (ResPES). As estruturas cristalográficas foram estudadas pela difração de elétrons de baixa energia (LEED) e a morfologia dos filmes foi sondada via microscopia de força atômica (AFM).

Entre os óxidos de manganês, particular atenção foi dedicada ao Mn_3O_4 e MnO, que foram depositados em substratos metálicos para evitar sua natureza isolante. Ambos ${}_{x}O_{y}$ são obtidos em condições de crescimento particular: deposição e recozimento na mesmo p(O2): $\sim 5 \times 10^{-7}$ and $\sim 5 \times 10^{-8}$ mbar para Mn_3O_4 e MnO, respectivamente.

As medidas de XPS/UPS foram feitas para determinar o estado de oxidação e verificar a formação de diferentes Mn_xO_y. A depender da espessura do filme, diferentes estruturas de Mn_3O_4 e MnO sobre Cu(111) são obtidas, como observamos com o LEED.

Os resultados dos filmes de Mn_3O_4 dopados com cobalto foram obtidos em um substrato diferente - Au(111). Esta escolha deve-se à sobreposição entre as energias de ligação do elétron auger do oxigênio (O KLL) e dos orbitais do Co $2p$. Foram explorados diferentes condições para obter o sistema dopado, até ser observado características LEED semelhantes ao filme não dopado. Os filmes foram preparados depositando-se alternadas camadas de Mn_xO_y, Mn e Co. Este passo é fundamental para o desenvolvimento do sistema dopado, pois neste cenário nosso resultado sugere que a inclusão de Co não altera as estruturas eletrônicas e cristalográficas dos filmes. As medidas de XAS e ResPES foram feitas na linha de luz PGM do Laboratório Nacional de Luz Síncrotron (LNLS), em Campinas, Brasil.

Palavras-chave: filmes finos, MnO, Mn_3O_4, propriedades eletrônicas, estrutura cristalográfica, dopante.

LIST OF PAPERS

This thesis is based on the following papers:

I. **Mn_3O_4 thin Film on Cu (111): Modulating Electronic Structure through Film–Substrate Interaction**
Emilia Annese, **Astrid Alí**, Jade Barreto, Fernando Stavale. The Journal of Physical Chemistry C 124 (28), 15162-15170. DOI: https://doi.org/10.1021/acs.jpcc.0c01961

II. **Unraveling hausmannite (Mn3O4) thin films surface structure by X ray linear dichroism**
Emilia Annese, **Astrid Alí**, Jade Barreto, Guilherme Felix, Fernando Stavale. Applied Surface Science 578, 151944. DOI: https://doi.org/10.1016/j.apsusc.2021.151944

III. **The structure of Mn3O4 (110) thin films**
Rubem Caetano, **Astrid Alí**, Jade Barreto, Guilherme Félix, Maria I Ramos, Braulio S Archanjo, Carlos A Achete, Emilia Annese, Fernando Stavale.
DOI: https://doi.org/10.1016/j.susc.2022.122062

CONTENTS

LIST OF TABLES

LIST OF FIGURES

FIGURE **Page**

CHAPTER 1

INTRODUCTION

1.1 Introduction

Alternative energies with less environmental impact have been explored, that is, clean and renewable energies [5]. To date, harvesting from solar energy sources such as wind, water and biomass has made considerable progress. But this is not the answer to the problem of a future scarcity of clean and renewable energies or fossil fuels [6].

Alternatively, the development of artificial photosynthetic systems could offer means to use solar energy to produce clean fuels but it is actually a long-standing challenge [5, 7]. The natural conversion of solar into chemical energy carried out by plants and photosynthetic bacteria is due to complex chemical reactions where recent advances have shown the presence of a manganese-calcium cluster (complex) [8]. An analysis of crystallographic structures reveal that this complex, bounded to protein groups may promote the biological water oxidation and develop catalysts for artificial photosynthesis [3]. This cluster originates from $Mn^{3+,4+}$ charge transfer reactions [2, 9].

Another important benefit of manganese oxides is its use and great importance in the manufacture of battery industry. Li-ion batteries have dominated the electronic devices industry since their development as a primary source [10], but the abundance of lithium, its cost, and the lack of an appropriate cathode to improve high energy density are an imminent concern. In recent years, batteries using rare earths such as sodium-ion or rechargeable magnesium battery (rMB) have received a lot of attention.

MnO_2 with Mn^{+4} has been one of the first and few cathodes that have worked in conjunction with rMB. This is because manganese dioxide is easy to synthesize and is widely used in dry cells due to its cell capacity [10, 11]. It is also known to be an promising positive electrode and excellent catalyst for the oxidation of CO onto CO_2 at low temperatures [12, 13].

Therefore, Mn valence state and relative concentration appears to play a pivotal role on a number of physical and chemical phenomena. For this reason, we have investigated in this doctorate thesis the formation of well-defined MnO and Mn_3O_4 thin film surfaces to serve as model systems for further chemical reactivity studies. Additionally, we have also explored Mn_3O_4 films doping using cobalt in order to modulate the bare oxide surface properties. This later may be potentially used to investigate the role of dopants on the oxide film electronic properties.

Manganese oxide belongs to a class of transition metal oxide (TMO) semiconductors characterized by its optical, electrical and magnetic properties that are generally depend on the oxide density of intrisinc defects (i.e.: vacancies, intersitial and dislocations) [14, 15].

Most of the TMOs are semiconductors and characterized by having partially filled d states and more than one oxidation state (mixed valence) that favores redox reactions. They are commonly used as cathodes in electrochemical systems [16] and their conduction band is formed by the metal d orbital and oxygen $2p$ level [14]. Transition metals have a high storage capacity. However, due to their low conductivity, these materials show a low perfomance in catalytic activity. To improve on this "defect", TMOs can be doped with other metals such as cobalt for example or mixed with carbon-based materials [17].

In reactions like water oxidation or oxygen reduction in batteries, it has been observed that the presence of oxygen vacancies and active sites in MnO and Mn_3O_4 improves their reactivity [18, 19]. Their low conductivity and almost insulating nature in bulk form was mentioned previously as a problem. Another way, different from doping, to avoid this inconvenience is by preparing samples consisting of few atomic layers [20]. There are different ways of sample preparation like calcination process [18, 21], precipitation or solvothermal route [22, 23], as well as the deposition of thin films [20, 24].

In this work, we aim to fabricate the thermodynamically stable MnO and Mn_3O_4 thin films on single crystal Cu (111) surface as function of growth parameters. Mn oxides manifest in several crystallographic structures and in each of them Mn exhibit different oxidation states in our study. One way to identify their oxidation state and thickness is by x-ray photoemission spectroscopy (XPS) or Low energy electron diffraction (LEED) techniques. Furthermore, we attempt to modify the electronic and chemical properties of Mn_3O_4 films by introduction of dopants. This procedure may help tuning the band gap energy and modify the optical and electronic properties [25]. For the fulfillment of this work we have the following objectives and methodology.

1.2 Objectives

The main objective of the doctoral project is the fabrication and characterization of undoped and doped manganese thin films oxide supported on metal surfaces (either Cu or Au). The electronic and crystallographic structure of these films were investigated by several experimental techniques such as XPS, UPS, LEED, XAS and ResPES.

The specific objectives are:

1. Literature review of MnO and Mn_3O_4 (chapter 2) and the experimental techniques (chapter 3).
2. Analysis of the copper substrate used as reference before the thin films (chapter 3).
3. Fabrication of MnO and Mn_3O_4 thin films by varying growth parameters (p(O_2) and thickness) at deposition time. We focus our study in MnO (chapter 4) and Mn_3O_4 (chapter 5).
4. Tuning the electronic properties of the Mn oxides film by introducing cobalt as a dopant: Co - Mn_3O_4 (chapter 6).
5. Global summary of all previous results as a final approach (chapter 7).

1.3 Methodology

Our methodology is based on the objectives mentioned above, therefore it will be divided in six chapters without considering the introduction and conclusion chapters. Each chapter will set a specific topic, although the first two chapters show more theoretical issues and the last four the results obtained.

In chapter 2, we focus on literatura review. This chapter summarizes the results about growth, structure and electronic properties of manganese oxide thin films on metallic substrates as found in the literature. Particular attention will be given to the difference in the crystallographic and electronic structure of MnO (section 2.2) and Mn_3O_4 (section 2.3). Next, we will report a summary about doped manganese oxide films, their main distinctions and uses (section 2.4).

For chapter 3, we will discuss the main focus in the theoretical background i.e. the physical principles of experimental techniques used to characterize the films like XPS, UPS, LEED, XAS and ResPES. We then opted to do an analysis of the substrate as a guide for future analyses (MnO and Mn_3O_4).

The growth of MnO thin films on Cu (111) at p(O_2): 5×10^{-8} at room temperature and as a function of thickness will be devoped in chapter 4. The oxidation state of films will be determinated by XPS and the different phases founded by LEED patterns. We will investigate the valence band of two MnO films with different phases.

In chapter 5, we will study the growth of Mn_3O_4 thin films on Cu (111). We will discuss about Mn_3O_4 films deposited on clean Cu (111) at RT. Several films with different thickness were deposited at p(O_2): 5×10^{-7} mbar. As we studied for MnO, we will understand the electronic properties of Mn_3O_4, the same techniques used for the previous chapter will be used for the analysis of Mn_3O_4.

In the following chapter, we focus on valence band (BV) study of Mn_3O_4 by Resonance photoemission (ResPES). We will develop a detailed study of the valence band of two Mn_3O_4 films on Cu (111) with different thicknesses. First, we will confirm the Mn_3O_4 formation of both films and their surface structures. Next, we will focus on the main context of the chapter, the valence band. We will use, as in previous chapters, the techniques of XAS and REsPES to describe in detail the contributions and dependencies in BV, the results will be shown for both films in a comparative way.

The comparison between doped an undoped Mn_3O_4 on Au (111) will be discussed in chapter 7. First, the deposition of cobalt-doped Mn_xO_y thin films on Au(111) by varying the concentration of the dopant. Second, the characterization of doped thin films by the techniques mentioned before. We compare the morphological, structural and chemical composition with the results obtained in chapter 5 and 6.

Finally in chapter 9, we will discuss our results and we will present the perspectives of this work.

CHAPTER 2

LITERATURE REVIEW

2.1 Introduction

The functionality of TMOs has been investigated in different thermal, electrocatalytic or photocatalytic reactions such as the activation of simple molecules (O_2 [26, 27], H_2O [28] and CO_2 [29]). TMOs can be used as a replacement for noble metals due to his later demand, high price and abundance. One of the most important and current interests in oxide catalysis is the direct conversion of hydrocarbons into other more valuable products, which would lead to a better use of abundant gas resources [30]. Some TMOs with several oxidation states are recognized to be a good material for supercapacitors or batteries.

The electronic properties of transition metal oxides "TMOs" change depending on their shape and size: i.e. bulk, thin film or nanoparticle [24]. For applications like catalysis or batteries sources, the surface termination and electronic structure of a material with few monolayers play an important role rather than bulk properties [31]. Consequently we are partially interested in TMO thin films.

Their formula is A_xB_y where "A" is the transition metal and "B" is oxygen. These materials can be classified like ferromagnetic (CrO_2), anti-ferromagnetic (CoO, MnO), ferrimagnetic (Fe_3O_4), paramagnetic (Mn_3O_4) and ferroelectric (double oxides like $BaTiO_3$).

Among M_xO_y systems, the oxides with M=Mn such as MnO, Mn_3O_4, Mn_2O_3 and MnO_2 are know to be the stoichiometric stable phases, characterized by distinct crystallographic structure [15]. It is well known that the higher is their oxidation state, the more stable is the system [32], i.e. the Mn_2O_3 and the Mn_3O_4 are energetically and structurally more favourable than MnO [20].

The low conductivity or insulating nature of bulk TMOs was mentioned previously as a problem. Another way, different from doping, to avoid this inconvenience is by using samples consisting of few atomic layers [20]. Thus, to be control of sample thickness, we are interested on deposition of thin films [20, 24].

Among all the preparation methods mentioned before, we are concerned on the oxide thin film deposition based on metal vapour deposition in presence of p(O_2). The partial oxygen pressure during the growth and post-annealing is one of the important parameter to control the oxide phase for samples. Therefore, depending on p(O_2) different surface structures and chemical composition can be obtained [24].

The growth of epitaxial Mn_xO_y thin films depends on how the atoms are arranged on a metal surface i.e. there is a dependency with the lattice parameter of the substrate. The mismatch between the thin film and the substrate helps to understand the favorable growth of some Mn_xO_y, so different substrates with different lattice parameter were found in the literature. Up to now, Mn oxides were deposited on several metallic substrate such as Ag(001) [4, 20, 24, 33–37], Rh(111) [38], Rh(100) [39], Pt(111) [40, 41], Pd(100) [42–44] and Au(111) [45, 46].

A way to establish the chemical composition of the thin film oxides is by photoelectron emission measurement that is sensitive to the Mn oxidation state, its chemical surrounding at the surface. Ilton *et al* have reported about the determination of manganese states by using XPS for oxides and hydroxides [47]. In particular, the analysis of Mn $2p_{3/2}$ whose binding energy increases as a function of its oxidation state. However, when the experimental resolution is not sufficient to distinguish the binding energy of two Mn oxidation state other features in photoemission spectrum may help in disentangling one oxide from the others [48]. In this sense, the oxidation state can be identified with three features:

- The binding energy of Mn $2p_{3/2}$.
- The location of satellites above Mn $2p_{3/2,\,1/2}$ at specific binding energy.
- The Mn $3s$ multiplet splitting.

The satellites are caused by the contributions of charge transfer states to the ground state contribution [49]. The Mn 3s split occurs due to the interaction between $3s$ and $3d$ states [50]. The importance of Mn $3s$ has been discussed in some references such [51].

As a reference we filled the table 2.1 with the representative binding energy of Mn 2p, the Mn $3s$ splitting and difference energy between Mn $2p$ main peak and satellite of several Mn_xO_y as present in the literature [20, 42, 48, 52]. The table 2.1 shows that Mn $3s$ splitting decrease even as oxidation state increase.

Oxide	Oxidation state	Mn $2p_{3/2}$ (eV)	Δ E (Sat) (eV)	Δ E (Mn 3s) (eV)
MnO	2+	641.0	5.4	5.9 - 6.2
Mn_3O_4	2+, 3+	641.5	11.3	5.1 - 5.7
Mn_2O_3	3+	641.9	10.5	5.4 - 5.7
MnO_2	+4	642.6	11.9	4.5 - 4.7

Table 2.1: Approximate values found in literature for different Mn_xO_y with their respective oxidation state, $2p_{3/2}$ peak position, distance between satellite to the main peak and the Mn 3s multiplet splitting.

In addition to XPS, there are another techniques like UPS, LEED, XAS and RPES that give information about growth and structure of thin films. All these techniques will be used in the experimental part and that we will explain one by one in chapter 3. Although our results are based on thin films, the Figure 2.1 shows the structures of MnO (left) and Mn_3O_4 (right) in bulk crystals and our expectation is that the films system may resemble, at least a thick film, their bulk counter parts. Clear differences are appreciated as Mn^{2+} occupies tetrahedral and octahedral sites in Mn_3O_4 and MnO, respectively as shown in Figure 2.1.

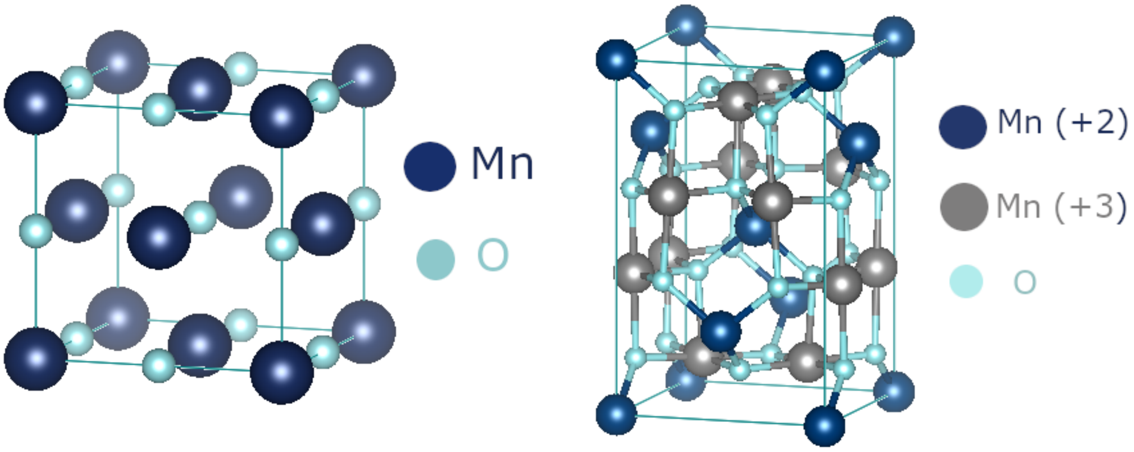

FIGURE 2.1. (Left) Unit cell type rock-salt of MnO with lattice constant of 4.44 Å. (Right) Tetragonal unit cell of Mn_3O_4 spinel with lattice constant of $a = b = 5.76$ Å and $c = 9.47$ Å [53].

2.2 MnO

MnO has a cubic rock-salt structure with Mn (2+) ions localized in octahedral sites at room temperature. Each cubic unit cell has four Mn^{2+} and four O^{2-} and its lattice constant is 4.44 Å [54], see Figure 2.1. MnO bulk phase is of relative importance in magnetic studies and is know to display an antiferromagnetic behavior with a Néel temperature near of 120 K, that changes to a paramagnetic state above this temperature [24]. Its surface properties have been investigated previously exploring MnO single crystals as well as thin films as follows.

Kundu *et al* studied how the structural and chemical properties of Mn_xO_y changes by varying $p(O_2)$ from $9x10^{-9}$ to $5x10^{-7}$ mbar [24]. They prepared MnO films on Ag(001) by optimizing post-annealing procedure by playing with the pressure in three subsequent steps: UHV, $p(O_2)= 1x10^{-8}$ mbar and finally in UHV again. Two different surface structures were found by LEED, as seen in Figure 2.2 (Left). In panel (a) the square LEED pattern is associated to clean Ag(001) substrate. In the other panels they obtained the reconstruction of Mn oxides: (b) MnO(001) with structure (1x1) at $p(O_2)= 1x10^{-8}$ mbar; (c-d) and Mn_3O_4 reconstruction (2x2) at $3x10^{-8}$ and $5x10^{-7}$ mbar. "As a result, two types of oxides were found as a function of p(O2)".

XPS measurements were used to distinguish the oxide thin films stoichiometry. The Mn $2p$ spin-orbit splitting of films grown with $p(O_2)$ above 3×10^{-8} mbar is 11.7 eV, this value in blue and green spectra is associated to Mn_3O_4. The red spectra relative to the film prepared at 1×10^{-8} mbar present Mn $2p_{3/2}$ binding energy shifted of 0.5 eV downward, and it is associated to MnO, with Mn^{2+} as oxidation state. A satellite peaks is located at 6.12 eV and 10.1 eV of the main peak at $1x10^{-8}$ mbar and $3x10^{-8}$ - $5x10^{-7}$ and this is characteristic for MnO and Mn_3O_4, respectively [24]. All their results matching with the literature, see Table 1. "As a result, the two types of oxides were identified by XPS".

Now we will focus on another feature capable of identifying manganese oxides, the Mn $3s$ splitting. Muller *et al* studied the growth of MnO (001) film deposited on a silver metallic substrate Ag(001) with lattice parameter of 2.89 Å. To get epitaxial films, they deposited several manganese films by varying the oxygen pressure $p(O_2)$. But finally, they use a low $p(O_2)$ like $\sim 2x10^{-8}$ mbar at room temperature to promote the growth of MnO, and then annealed in UHV at different temperatures between 300 to 1000 K. A lattice mismatch between substrate and film was found close to ~ 9% [20]. The lattice mismatch in epitaxial systems can be related to interfacial strain effects that can modify the physical properties of the system [4].

The characterization of the MnO films was determinate by XPS looking at Mn $3s$ and Mn $2p$ core level. Figure 2.3 shows the Mn $3s$ spectra of MnO bulk and thin films by varying the annealing temperature. In MnO bulk crystal the splitting is 6.15 eV and it is used as reference in Table 2.1. The films grown at several temperatures have no shown changes about the splitting,

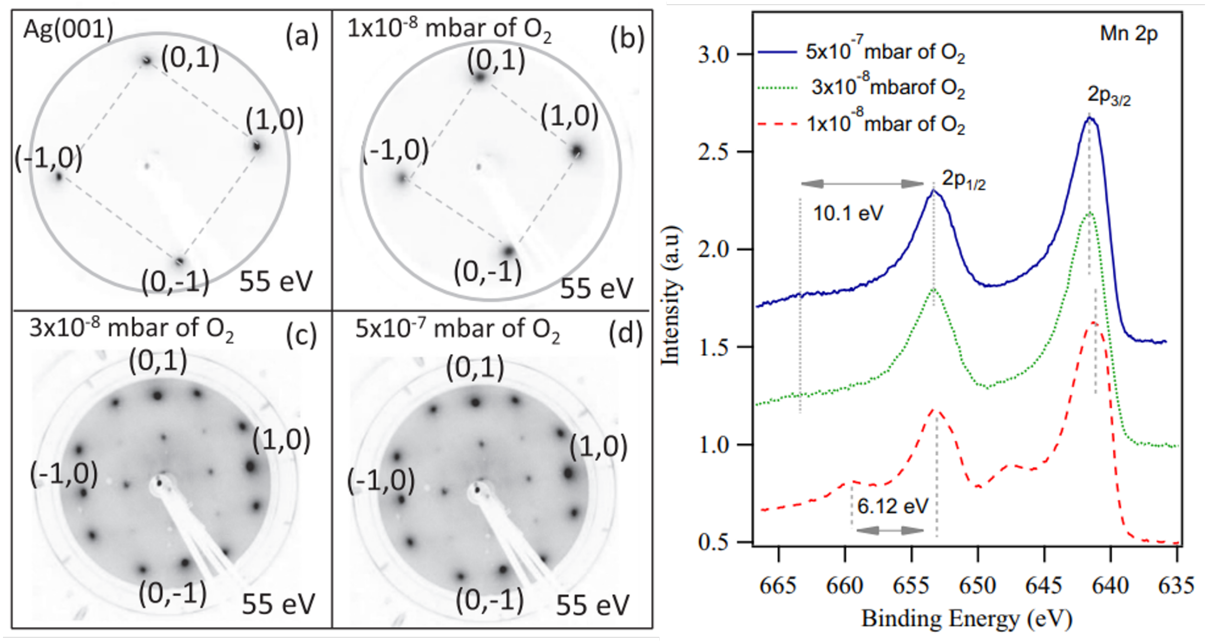

FIGURE 2.2. (Left) LEED pattern at 55 eV of (a) clean Ag(001) (dashed square represents unit cell), and 10 ML of MnO (b) and Mn_3O_4 (c,d). (Right) Mn 2*p* high resolution (HR) spectra at different p(O_2). At low and high pressure, the formation of MnO (red) and Mn_3O_4 (blue and green). Adapted from [24].

and in all cases was found to be in the range of 6.1-6.2 eV. The intensity of Mn 3*s* is higher at 300 K, that means the surface substrate is completely covered. By increasing the temperature, the intensity of the peak Ag 4*s* (substrate) increases since part of the film has been removed [20]. The intensity ratio of the peaks was no reported in this work because the overlapping between Ag 4*s* and Mn 3*s*. And Mn 2*p* has not shown any change as a function of temperature. "As a result, Mn 3*s* splitting does not change as a function of annealing".

Different structures depending on pressure and temperature can be found by LEED like a plane (001) or a surface polar (111) or a mixed phases containing MnO and Mn_3O_4 for example. We already mentioned the plane (001) in the review for Muller's research [20]. More information of mixed phases can be founded in the next reference [55]. For now, we will briefly focus on the polar plane (111) as the following references [41, 43, 56].

According to DFT study [57], the plane (111) is the most stable with the (2x2) reconstruction. For Allegretti *et al* using a p(O_2) above 10^{-7} mbar and low temperatures (350 K), a well ordered and stable MnO (001) on Pd (100) was grown with a mismatch near ~ 14% [43]. But by increasing the annealing temperature (above 873 K) in UHV or $1x10^{-7}$ mbar, they found that the plane (100) transform into (111) with a reconstruction of (2x2) as expected by DFT. "As a result, changing the

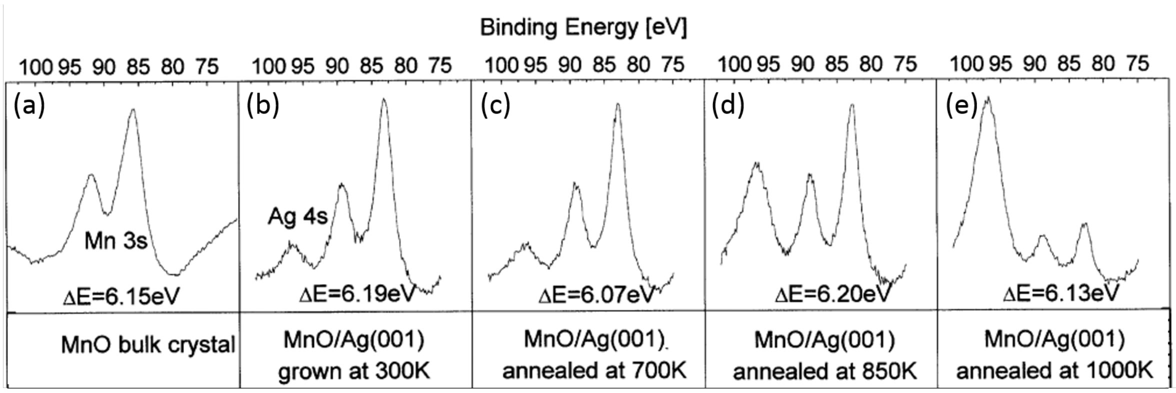

FIGURE 2.3. Mn 3*s* splitting as function of temperature for MnO bulk (a) and MnO thin film grown at 300 K (b), 700 K (c), 850 K (d) and 1000 K (e). Ag 4*s* peak enhances in intensity when temperature increases. Adapted from [20]

temperature (100) becomes (111)".

A general trend observed in all reports in the literature is that at low p(O_2) is possible to growth MnO, but increasing the oxygen pressure (above $5x10^{-7}$ mbar) the formation of Mn_3O_4, a mix of Mn^{2+} and Mn^{3+} is expected. Also, Mn_3O_4 can be formed through the oxidation of MnO at high oxygen pressure [43, 58].

2.3 Mn_3O_4

In recent studies, spinels with mixed valence have drawn attention due to its structural and magnetic properties that are related to physical phenomena such as magneto dielectric, magnetoelastic and quantum phase [59, 60].

The spinels had the formula of AB_2O_4 with (2+) occupying the tetrahedral and (3+) the octahedral sites. The "AB" compound can be a mixture of ternary spinels like $MnAl_2O_4$ or can be the same metal with different valences like Mn_3O_4 [61].

Mn_3O_4 can be considered as an ideal material used in several applications and technology, as reactive catalyst, material sensors, electrochemical energy storage devices [62] and supercapacitors [63].

Hausmannite or Mn_3O_4 in its bulk form has been extensively studied experimentally and theoretically, due to its electronic configuration and distorted structure. Mn_3O_4 (2+, 3+) has cations of Mn^{2+} and Mn^{3+} localized in tetraheddral (MnO_4) and octahedral (MnO_6) sites of its structure, respectively, see Figure 2.1 (left) [59]. Mn^{3+} ion has a d^4 electronic configuration with low spin while Mn^{2+} ion has d^5 with high spin [64]. Mn_3O_4 presents a distorted tetragonal spinel structure elongated in "c" axis due to Jahn-Teller distortion at Mn^{3+} sites at room temperature

(RT) with a lattice constant of $a = b = 5.76$ Å and $c = 9.47$ Å [15].

Relatively fewer studies about the growth of Mn_3O_4 films as compared to MnO are found in the literature. Despite recent reports from Gillmeister *et al* [33], Kundu *et al* [4] and Ren *et al* [65, 66], which have deposited Mn_3O_4 films on Ag(001) and $MgAl_2O_4$, respectively, by e-beam evaporation (EBE).

Gillmeister *et al* focused on the characterization of Mn_3O_4 thin film using NEXAFS, STM and LEED. They studied the surface structure as a function of thickness and temperature. Manganese was deposited at $p(O_2)=5x10^{-7}$ mbar and by varying the tchickness two diferent structures were obtained, $Mn_3O_4(001)$ with p(2x1) and c(2x2) termination as observed by LEED. Their report show results about energies resonance in the NEXAFS spectra at O K-edge located at 539.4, 540.8 and 548 eV that are characteristic for Mn_3O_4 and no other oxide. Another features can be observed at 530.1 eV, 531.2 eV, 533.3 eV and 536.7 eV as you can see in Figure 2.4 but there are not only features of Mn_3O_4.

X-ray absorption spectra of Mn_xO_y with different oxidation states can be found in the following reference [67] or Figure 2.4. In figure 2.4, the L_2 and L_3 edges are related to the transitions from $2p_{1/2}$ and $2p_{3/2}$ to $3d$ unoccupied states, respectively. The L_3 peak has a shift to higher energy when the oxidation state is higher. The peaks are separated by the spin-orbit interaction [68]. For O K-edge, the absorption between 528 and 535 eV is due to charge-transfer transition to Mn $3d$ states. Whereas at higher energies than 535 eV is related to transitions between metal-oxygen sp states [67].

In the reports shown by Kundu *et al*, they decided to focus about the stability of $Mn_3O_4(001)$ film as function of the thickness to observe the evolution of the surface structure. But the growth temperature was not fixed, a parameter that plays an important role in stabilize its polar surface (001) [69] and is critical in its final structure. Several films as function of thickness were prepared and annealed at RT and 473 K to obtained epitaxial thin films. Also Mn_3O_4 was obtained by the oxidation of MnO (111) at 473 K. All the films have different terminations that were observed by LEED: p(1x1), p(2x1), p(2x5) and (2x2) [4].

Mn_3O_4 have two surface terminations: A manganese-oxygen layer (3+) or Mn_2O_4-t and manganese layer (2+) or Mn-t.

The Table 2.2 shows that as a function of temperature substrate, for thin film (3 ML) two structures with different layer terminations were obtained but for thick film (4-10 ML) the same structure was observed. DFT calculations shows that Mn_2O_4-t is the most favourable and Mn-t is energetically unfavorable, this means that p(2x2) termination it is no expected. Gillmeister *et al* [33] observed in STM results that p(2x2) reconstruction is an overlapping between p(2x1) and c(2x2). To verify this assumption, the film was oxidized and a transformation from Mn-t to Mn_2O_4-t was expected. But no changes was notice and this supports the idea of the coexistence of

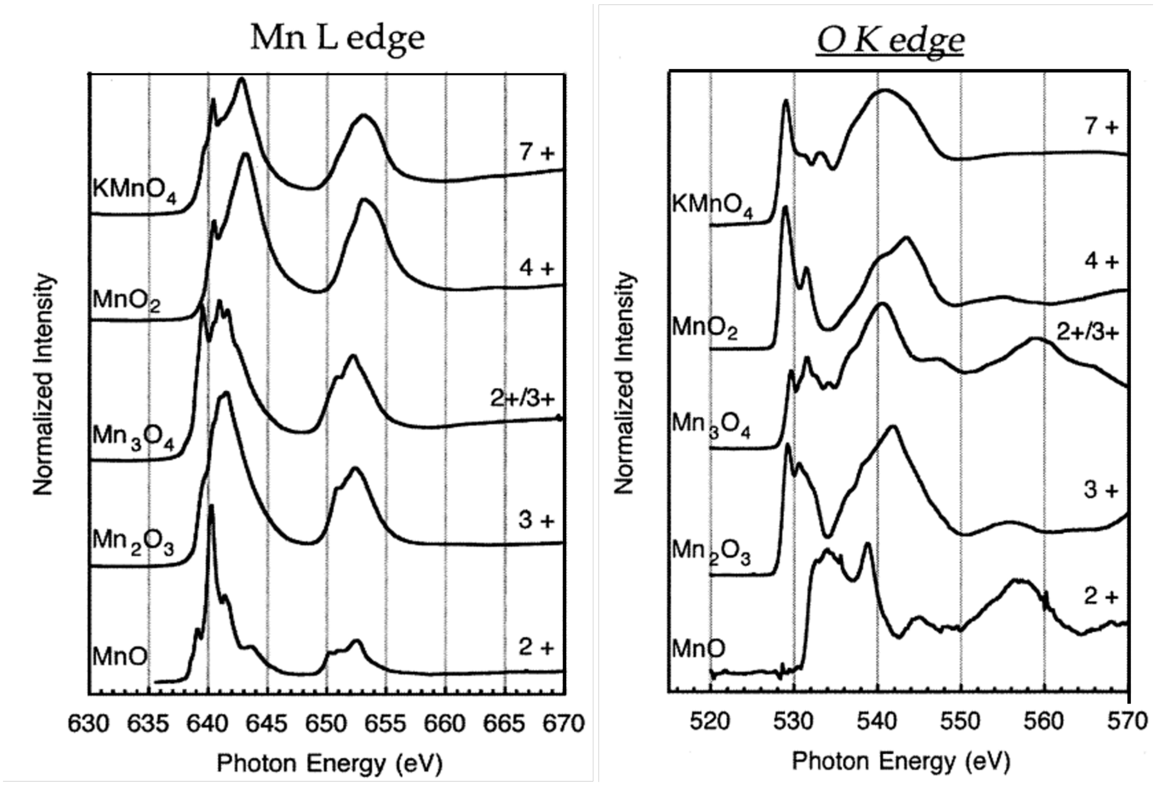

FIGURE 2.4. (Left) Manganese L$_{2\text{-}3}$-edge and (right)oxygen K-edge XAS spectra of different manganese oxide. Mn L$_{2\text{-}3}$-edge is completely dominated by Mn 3*d* states. The numbers indicated at the right side of each spectra correspond to the oxidation state of the Mn cations [67].

Mn3O4	Temperature	
Monolayers ML	RT	473 K
3	p(2x1)*	p(2x2)**
4 - 10	p(2x2)	p(2x2)
*: Mn_2O_4-t **: Mn-t		

Table 2.2: Surface structures of two Mn_3O_4 films with different thickness: 3 and 4-10 ML. "*" and "**" are the layers terminations for each reconstruction [4].

the overlapping.

The instability of the polar surfaces of Mn_3O_4 are the most studied and are characterized by uncompensated electrostatic potential. To avoid this instability, modifications near the surface can be applied like charge distributions, reconstructions and by the interaction with foreign atoms or "doping" [44].

2.4 Doped Mn_xO_y

Several metal oxides and specially mixed metal oxides have been studying due to band gap and its efficency in catalysis [70]. Specially Mn_xO_y, this oxide is a potential catalyst with high activity in low-temperature selective catalytic reduction (SCR) process. Thus, there is a major challengue to improve optical, morphological, thermal and electrical properties of this metal oxide with doping [71].

So, following the approach of this project we have interest in manganese oxide doping with alkaline metal like Ca in $MnCr_2O_4$ [72] or another transitions metal oxides, see Figure 2.5, like Niquel [73], Cadmium [70], Iron, Vanadium, Copper [74], Cobalt [75] and Zinc [76] for example [77]. Noble metals were initially used, but it changes towards earth abundant and low cost transition metals oxide [78]. The doping with low valence cations can modify the electronic structure and creates oxygen vacancies [79].

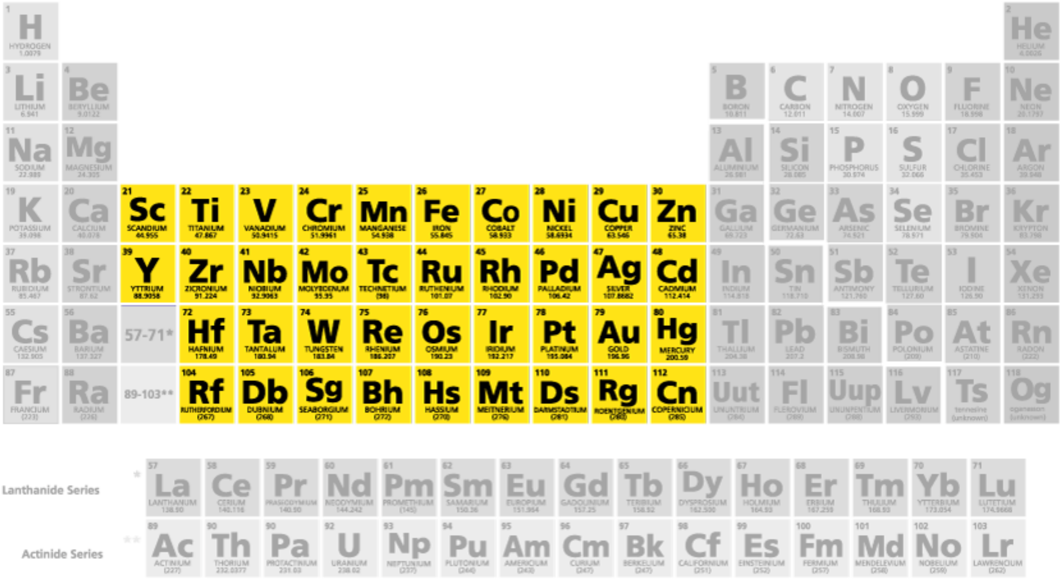

FIGURE 2.5. Positions of transition metal in periodic table [80].

Now we will detail a brief summary of works found in the literature. Our interest is identify the benefit and the influence of a specific transition metal in doped manganese oxides. And take "notes" on what we should expect in future measures.

Zamudio *et al* [72] verified that the addition Ca doping (1 to 5%) favors oxygen mobility[81] and electron donation capacity [82] i.e. an enhancement in catalytic activity. However, Gu *et al* found that a "Ca doping can harm its catalytic performance and properties when the dopant does not entered within the crystal lattices appropriately". As an answer, sol-gel method was used to dispersed Ca in Mn_xO_y/TiO_2. In this case, Ca atoms were better dispersed in manganese oxide. XPS results showed the increase of chemisorbed oxygen content from 8.69 to 11.35% through O 1*s* spectra as a function of % Ca. They use Ca to enhance the NO chemisorption to 90%, two times better that undoped oxide [77]. "First note, the film may not be formed due to the entrance of dopant. And they observe changes in XPS spectra."

Yang [75] deposited Co doped on amorphous Mn_xO_y and crystalline Mn_2O_3 thin films with various percentages (4.9 to 20.7 %) by pulse laser deposition PLD technique. X-ray diffraction (XRD) spectra show that "Co doping up to 20.7% does not change the structure of Mn_2O_3 phase" but it changed its microstructure that improve the capacitance behaviour. Cobalt ions replacing manganese favors its electronic structure and surface state. "Second note, large amounts of the dopant can modify the film structure."

For applications as a supercapacitors, Mn_xO_y has a relatively low specific capacitance compared with other oxides like RuO_2 and poor electronic and ionic conductivity. Doping Mn_xO_y to get mixed oxides has been shown to improve this task. Several works studied how to modify capacitance or electrical conductivity of oxide films by preparing mixed Mn_xO_y with Ir [83], Fe [84], Co [85], Ca [86].

Most of the references mentioned above have worked with different growth methods such as precursors, SILAR method, sol-gel and other, but there is almost no work that refers to thin films. This is one reason why we decided to dope our initial thin film system, Mn_xO_y, with cobalt. We will verify if there is any modification in its electronic and surface structure.

CHAPTER 3

MATERIALS AND METHODS

3.1 Photoemission spectroscopy (PES)

Photoemission spectroscopy is a technique used to characterize the electronic properties of sample surface i.e. gives us information about occupied electronic surface states [87]. Its physical principle is based on the photoelectric effect. This phenomenon takes place when incident light (X-rays, UV or synchrotron radiation) impinges a surface and is absorbed inducing the emission of electrons at specific energy (binding or kinetic) as show in Figure 3.1. In the process the photon transfers part of its energy to the electrons simply called photoelectrons which satisfy the energy conservation law as in 3.1, where hν, E_K, E_B, ϕ are the photon energy, the electron kinetic, the binding energy and equipment work function (analyzer), respectively. At given initial photon energy the electron E_K is characteristic for each element present in the sample [88].

$$E_K = h\nu - E_B - \phi, \tag{3.1}$$

The equation 3.1 is valid in the approximation that only one electron interacting with the incident photon and the excitation does not change any other orbital.

The next Figure (3.1) is described the photoemission process upon photon excitation an electron is ejected from 1s level (arrows). When the electron is emitted from the sample a hole is left behind (1s) and the system is in a metastable state. To bring back the sample to the initial state may occur two processes: Auger electron emission and fluorescence. In the first case upon the formation of hole (ionization), one electron from a higher energy state decay to occupy the vacancy (relaxation), and its energy is transferred to another electron that is ejected from the sample (emission) [89].

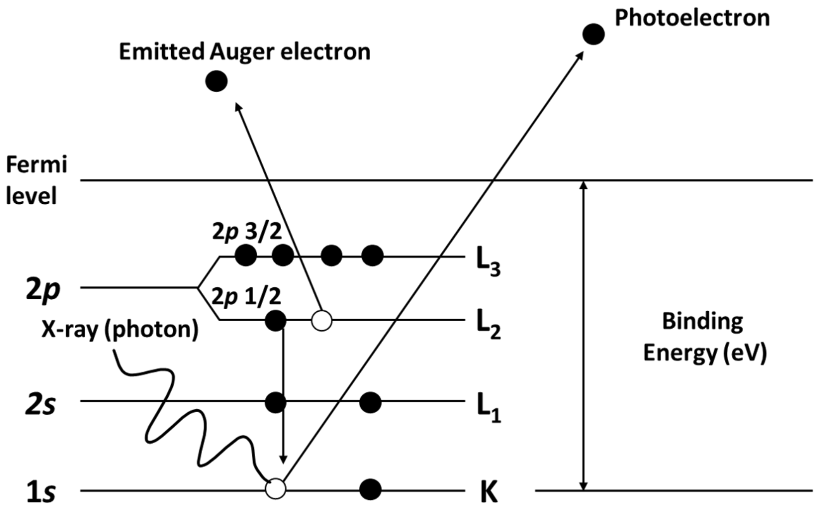

FIGURE 3.1. Schematic energy levels for X-ray (photon) excited photoemission process to eject a photoelectron from 1*s* level. A hole is left behind and another electron decay from 2*p* level (higher level) as Auger emission. Adapted from [90].

The atomic energy diagram scheme with atomic energy levels: 1s, 2s, 2p is show in Figure 3.1. Each electronic level is named as (nl_j), where a principal quantum number *n* indicates its deepness in energy (1, 2, ...), a angular quantum number *l* is related to the typology of orbital (s:l=0, p: l=1; d: l=2; f: l=3), a spin quantum number *s* (s=1/2, m_s=±1/2) is associated to electron spin orientation, a total angular momentum *j*: ($|l$+$s|$,$|l$-$s|$). In the case of *p*, *d* and *f* orbitals a not negligible **spin-orbital** interaction results in energy level split. The orbital occupancy is limited to 2 and 4 electrons (1:2) in the case of $p_{1/2}$ and $p_{3/2}$, whereas 4 and 6 for $d_{3/2}$ and $d_{5/2}$, etc...(Figure 3.2).

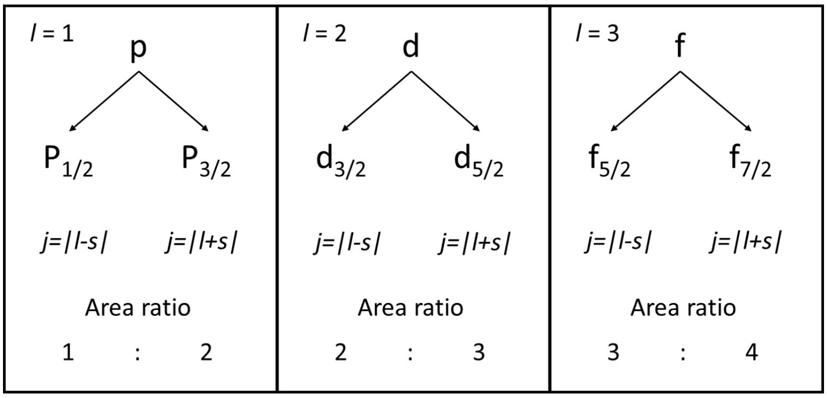

FIGURE 3.2. Scheme show the energy level split due to spin-orbital interaction and the area ratio for p, d and f orbitals. Adapted from [91]

The nl_j energy level is also named using letter K, L, M from the inner to the outer orbital. To the Auger electron is associated a sequence of three letters. The transition depicted in the Figure 3.1 is named: KL_2L_2. V and C are used when a valence electron and core level are involved [89]. The Auger emission named generically XYZ has a kinetic energy given by the difference between the binding energy of levels involved in the process

$$E_K \approx E_X - E_Y - E_Z \tag{3.2}$$

Up to now, we have considered the one-step theoretical approach about the photoemission process, it means the one electron approximation which is removed from an occupied state of a solid. However, in the ionization process, the incident photon interacts with N-electron within the solid and E_B is given as the difference between the N electrons from the initial state and the N-1 electrons from the final state $E_B = E_f^{N-1} - E_i^N$.

Another way to depict the photoemission is its representation as a three-step process which is considered the simplest [88].

1. Absorption of photon by electron - "excitation process of an electron from an initial to a final state within the cristal.";
2. Travel of through the material until reach its surface;
3. Photoelectron ejection from the material to the vacuum, that is, the electron crosses the surface.

In a simpler way, we can assume that the final state wave function is the contribution of the excited state together with the scattered waves from neighboring atoms [87].

The first step is described by the golden-rule transition probability.

In the second step, several electrons suffer from inelastic scattering which means that they lose part of their energy due to electron-plasmon or electron-phonon scattering. In a photoemission spectrum, these electrons that have lost information about their initial state contribute to the background [87]. There is a probability that an electron does not lose its energy when it reaches the surface and it is due to the mean free path (λ). λ depends on the energy and the wave vector k and its values are usually between 5 and 20 A. This second step defines photoemission as a surface-sensitive technique.

In third step, the emitted electron (outside the material) can be considered as a Bloch electron wave with only the parallel component of the translational symmetry [87].

In this approximation it is possible to explain electron kinetic energy loss with respect to the electron transition within one electron picture. The contribution from the initial state is due to effects of the screening of nucleus by the valence electrons on the core states (atom) and the surface acting as dipole when we have adsorbate-substrate system. For the final state, the two contributions are: the system response to the hole produced by ionization and the photoelectron travelling through the solid (interacting with other electrons) [88, 92].

Once the relaxation effect are accounted for, the energy conservation (3.1) modifies into:

$$E_K = h\nu - E_B - \phi - \Delta E_{relax}, \tag{3.3}$$

During the relaxation process, phonons and plasmons also undergo a collective excitation. Because of this, the photoemitted electron receives only part of the relaxation energy since the rest has been used to excite a plasmon or phonon. This photoelectron is detected as a satellite peak structure.

Photoemission (PE) cross-section is the probability of an electron being emitted of its electronic state and depends on the photon energy. The inner electrons are ionized easier than outermost at fixed incident energy [93, 94].

In a photoemission experiment the ejected electrons are discriminated in terms of their kinetic energy and represented as the number of electrons versus their E_k (or E_B using eq. 3.1). A relative maximum intensity is recorder in correspondence to electron ejection from a specific atomic energy level or Auger electron emission.

Electron in core and outer energy level requires photon energy to be excited that may vary of order of magnitude. It is common to use UV or X-ray source to probe electron in valence and core levels, respectively. So, depending on the photon source such as X-ray or ultraviolet source, the photoemission spectroscopy may be referred to as XPS or UPS.

If an ultraviolet power source (UPS) (He I_α: 21.2 eV) is used, the final states have a structured density of states that generates strong changes in the photoemission current. On the other hand, with an x-ray source (XPS) (AlK_α (1486.6 eV) and MgK_α (1253.6 eV)) the final states have an almost continuous distribution due to the quite high energies of the photons, which means that the photoemission current does not suffer alterations.

The most used experimental methods or techniques to study the growth of films in situ are auger spectroscopy (AES) and x-ray photoemission spectroscopy (XPS). The characteristics core-level emission lines of substrate and adsorbate are measured as a function of coverage. It is known that photons must penetrate a certain amount of material before leaving the sample surface. Therefore, independent of the excitation mode, the intensity of the signal depends on the mean free path of the electrons and the amount of matter penetrated. Due to the "strong" interaction in matter (excitation of plasmons) the mean free path of electrons is of the order of few angstroms, thus electrons from higher atomic layers contribute to the detected XPS signal.

When an electron of an atom or molecule adsorbed on a solid surface is excited by photoemission, a valence or core hole is created that is different from that of the original free atom or molecule. Therefore, photoemission is an important experimental technique to study the band structure of occupied electronic states of the surface.

3.2 Low energy electron diffraction (LEED)

LEED is used as a technique to check the crystallographic quality of a surface, either clean or with an adsorbate. The long range order of crystal surface is determined by diffraction of low energy electrons. Due to their dual nature electrons behave as wave and particles. As a wave they can be reflected constructively by a periodic array whose size is comparable to its wave length, as it is for the atomic distances in the crystal surface net for low electron energies. When a beam of electrons with initial energy between 50-300 eV strikes the surface of a sample, the elastically backscattered electrons generate diffraction or Bragg spots that are reflected on a phosphor screen [87].

The diffracted electrons are collected on a two dimensional screen and the geometrical distribution of the spots (diffraction pattern) represent the surface 2-D reciprocal lattice (qualitative LEED acquisition mode). Alternatively, the intensity of diffracted beams is registered as a function of the energy of the incident electrons in quantitative mode, i.e. I-V curves (quantitative LEED acquisition mode) [95].

The theoretical approach is based on the kinematic theory where each Bragg spot is originated when a 2-D vector of the surface reciprocal lattice is equal to the parallel component of the scattering vector. According to the experimental geometry, the wave vector k of the main beam has the central position at (0.0). A sphere around this central point is constructed and is called Ewald sphere [87], Figure 3.3.

First, let us take into account the dispersion of the innermost and outermost lattice planes. The "thicker" regions of the lines (black line) come from Laue's third condition. So when the Ewald sphere fits one of the "thicker" lines, the bragg spot is more intense (strong reflex) while the regions where it does not match originate weaker spots (weaker reflex) as marked in the figure. If the incident energy of the electrons that depends on k is changed, the radius of the Ewald sphere also changes. Therefore the sphere moves as a function of energy and passes between the strongest and weakest thicker lines so the diffraction spots appear and disappear on the screen. That means that the intensity of a bragg spot varies periodically as the energy varies.

A LEED pattern represents various scattering processes within the uppermost atomic layers of a sample. This pattern can help identify some possible problems such as: (1) substrate contamination if the spots are not sharp with high contrast and low background intensity. (2) Defects or imperfections show up as blemishes and they will increase the intensity of the background. A simple and clean sample must show a LEED pattern (1x1). When the surface of a sample undergoes a reconstruction, the LEED patterns becomes more complex. In some cases, the LEED results can provide information on surface crystallographic defects.

The mean free path is the average distance of how far an electron travels through a solid and is limited to a few atomic layers because low enegy electrons can not penetrate much without losing energy [96].

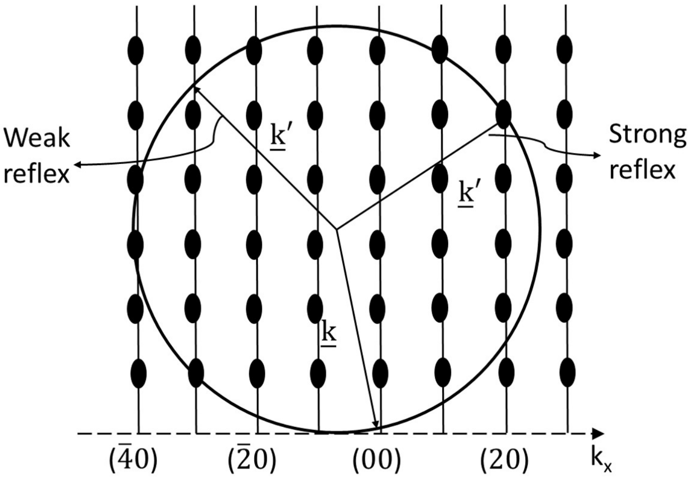

FIGURE 3.3. Scheme of Ewald construction for elastic scattering for 2-D surface lattice. Adapted from [87]

.

The diffraction pattern at well defined positions are studied through the relation between real and reciprocal space by fourier transform. In Figure 3.4, we observed two lattices with a periodicity of defined points whose vectors can define a unit cell.

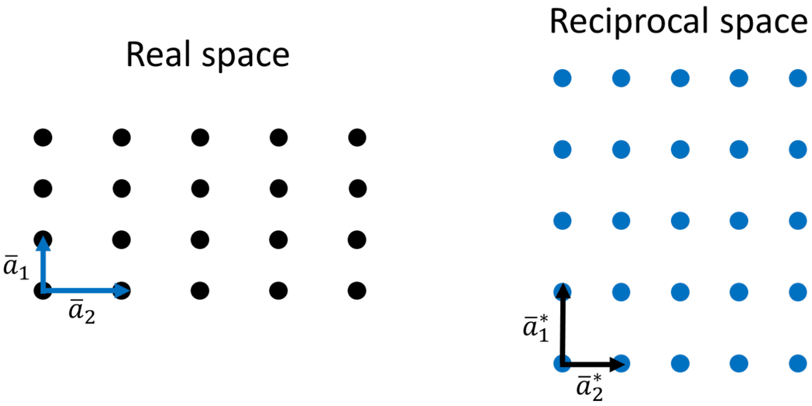

FIGURE 3.4. Real and reciprocal space for a lattice with its respectives vectors. Adapted from [97].

These vectors are "$\vec{a}_1$", "$\vec{a}_2$" and "$\vec{a}_1^*$", "$\vec{a}_2^*$" for real and reciprocal space, respectively [95] and are related as follows,

$$\vec{a}_1^* = 2\pi/\vec{a}_1$$
$$\vec{a}_2^* = 2\pi/\vec{a}_2$$

3.3 X-ray absorption spectroscopy (XAS)

XAS is a technique used to study the structure and unoccupied electronic states of a material. When a X-ray impinges an atom, a core electron is excited and taken to unoccupied level or into an unbound state, called continuum [98]. In both processes, a core hole is left behind. When the electron is ejected from the material, this process is considered the photoelectric effect seen in section 3.1. This technique measures the absorption of X-rays as a function of the incident energy (E_{hv}). The most important in an absorption XAS spectrum is the transition energy levels involved and their intensity.

To measure a XAS spectrum, a variable source such as synchrotron radiation is needed. So if the incident energy increases, the excitation process will involve higher levels of the valence band and an absorption edge is seen on the spectra. Furthermore, the XAS spectrum is defined by the structure of the outermost unoccupied levels.

1. For $E_0 = E_B$, the absorption increases dramatically, and there is a jump in the spectrum called the absorption edge.
2. For $E_0 > E_B$, a transition occur to the continuous state and the excess energy is carried by the photoelectron in the form of kinetic energy (E_K).

X-ray absorption depends on the electron binding energy, so the spectrum XAS will be characteristic of each chemical element. [98, 99].

Soft x-rays have a penetration depth between 500-1000 Å, it is a superficial level. The escape depth of the electrons is small due to the elastic dispersion they undergo before escaping from the sample. Although the electrons that manage to escape generate secondary electrons, these electrons manage to escape if they have enough kinetic energy to overcome the work function of the material [100].

If all emitted electrons are measured, it is known as total electron yield (TEY), while if only emitted photons are measured, it is known as total fluorescence yield (TFY). In the TEY mode, the electron current is measured directly with a channeltron or by measuring the total current with a pico-ammeter. The measurements are easier to carry out, although they may have some problems such as: samples may present charging effects if the conductivity of the material is low or saturation effects may occur in the measurements.

For example, the electron excited from the $1s$ level (deepest level) is called K-edge (highest-energy absorption edge), from the $2p$ level L-edge and so on. The table 3.1 show the relation between edges and core levels for all orbitals,

A typical absorption spectrum can be divided into two regions [101]:

Edge	M_V	M_{IV}	M_{III}	M_{II}	M_I	L_{III}	L_{II}	L_I	K
Core level	3d5/2	3d3/2	3p3/2	3p1/2	3s	2p3/2	2p1/2	2s	1s

Table 3.1: Designation of XAS transitions according to their core levels. K transitions for $1s$ level, L transitions for $2p$, etc.

1. **X-ray absorption near edge structure (XANES):** in this region, the energy of the edge provides information about the average oxidation state of the species in the sample.
2. **Extended X-ray Absorption Fine Structure (EXAFS):** This region provides information about the number, distances, and types of atoms surrounding the sample.

As we already mentioned, it is necessary a tunable X-ray source like a synchrotron radiations which provides a full range of X-ray wavelengths. A monochromator is used to select a defined energy (applying Bragg's law). In this project, XAS was used to verify the oxidation state and the contribution of an specific element.

The XAS peaks have a higher intensity than the resonance spectra peaks, that means that the transition levels that contribute to the XAS signal are higher than resonance. Both techniques in combination complement each other to identify the orbitals involved in the valence band.

3.4 Resonant photoemission spectroscopy (ResPES)

Resonance photoemission is a phenomenon that occurs in the vicinity of a x-ray absorption threshold (XAS). This technique is based on an interference between direct photoemission (DPE) process and the recombination of an excited state.

In **direct photoemission**, a photon is absorbed by an electron that is excited and then ejected from a material with kinetic energy E_k, as seen in Figure 3.5a. In **Auger decay or auto-ionization**, the photon energy excites an electron to the intermediate state leaving a core-hole, the same electron decays via Coulomb interaction filling the vacancy, and then another electron is ejected, Figure 3.5b [102, 103]. In both processes, the final state is the same. This means that the kinetic energy of the emitted electron is the same:

$$2p^6 3d^n \rightarrow 2p^6 3d^{(n-1)} + e \qquad (direct\ PE) \tag{3.4}$$

$$2p^6 3d^n \rightarrow 2p^5 3d^{(n+1)} \rightarrow 2p^6 3d^{(n-1)} + e \qquad (Auger\ decay) \tag{3.5}$$

This causes an increase in intensity of the visible states in the resonance spectrum.

The Figure 3.6 shows different cases (a) when the excited electron is localized in the atom (participator and spectator) and (b) when it is transferred out of the atom during the core-hole

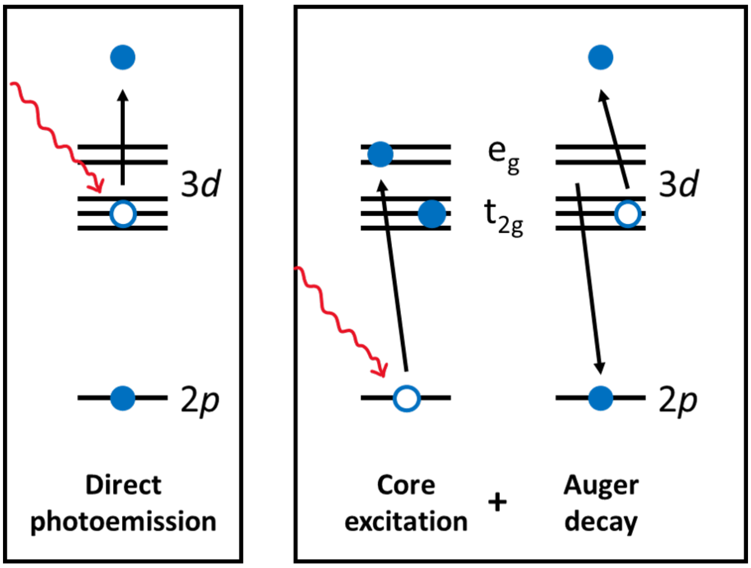

FIGURE 3.5. Scheme of both processes, the direct photoemission (left) and core excitation + auger decay (right). Adapted from [104].

lifetime (charge transfer). The core hole has a particular lifetime (τ) which is dependent on how quickly the hole is filled by an electron from another shell (of the order of 10^{-15} fs). A lifetime decreases the deeper the core hole, because core holes are filled by higher lying electrons. This is considered as atomic property, because the core-hole lifetime depends on the number of electrons that can lower their energy [102, 103].

By varying the energy of the incident photon along the absorption edge (Mn $2p$ for our case) of the element to be studied, the electronic contribution (density of states) of a specific element in the valence band region can be determined.

For example, the transitions from the Mn $2p$ to the Mn $3d$ state will be possible if the energy of the incident photon matches or is close to the Mn $2p \rightarrow$ Mn $3d$ transition and if the partially filled orbitals follow the selection rules. It is necessary that the $3d$ state was partially filled otherwise the resonance does not occur. This means that there will be an increase at the intensity (resonant behavior) within the valence band that belongs to the $3d$ state due to resonance [106].

In the case of MnO, each Mn^{2+} ion is surrounded by six O2− forming an octahedral crystal field that separates the $3d$ state into two orbitales: e_g (dx2y2, dz2) and t_{2g} (dxy, dyz, dxz). Both orbitals can show resonance although the binding energy and the photon energy for the transition from $2p$ to e_g state is slightly different towards t_{2g} state.

In the present study the Resonant photoemission spectroscopy was mainly used to study the contributions of different species in a material in the valence band (VB) region. A resonance spectrum is proportional to an element's density of states rather than a total density of states.

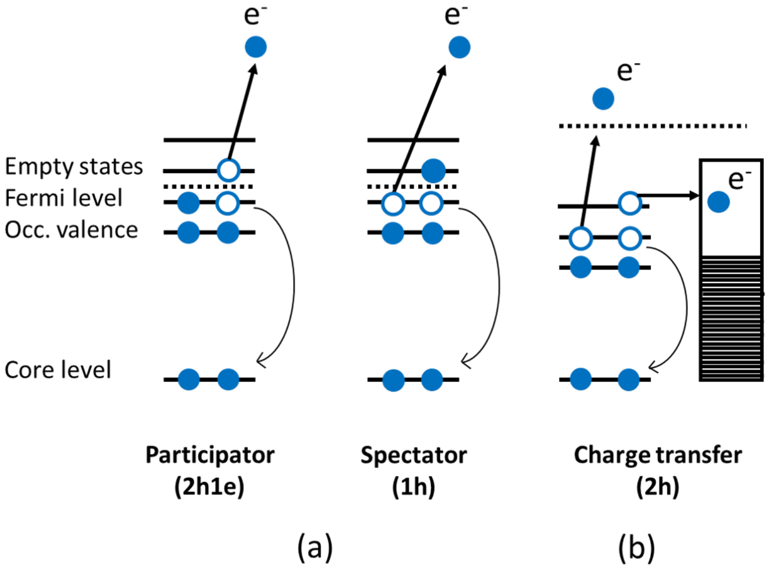

FIGURE 3.6. Schematic illustration of electron excitation and subsequent core-hole decay processes for participator and spectator (a), and change transfer (b). Adapted from [105].

This characteristic of resonance photoemission is used to "decompose" the valence band spectrum of a compound into elemental contributions.

3.5 Experimental details

The laboratory in CBPF is furnished with three experimental chambers: load lock, preparation and analysis. Each of them has specific goal. The first one (A - purple line) is devoted to the introduction of the sample from the air to the vacuum environment. The second (B - yellow line) to the cleaning (substrate), thin film growth and structural characterization of the surface. The preparation chamber (B) is equipped with LEED, sputter gun, heating stage and metal evaporator and leak valves for the dosage of gases. The analysis chamber includes a Phoibos 150 electron analyzer, He UV and X-ray source (with and without monochromator) among others interesting tools. The latter (C - blue line) is used for chemical characterization as X-ray and UV photoemission techniques, as you see the dashed lines in Figure 3.7.

A metallic single crystal (Cu or Au) terminated with the plane (111) was cleaned by a combinations of several cycles of ion sputtering and annealing. The ion sputtering was performed at Ar partial pressure of 5×10^{-6} mbar and with ion beam at 30º from the surface normal. The used ion energy ranges from 2 KeV to 800 eV depending on the previous condition of the surface (presence of thin/thick film, exposure to air, etc). The annealing was performed up to $T = 590$ K in UHV for 20-30 min. This temperature is measured at the site of sample holder and is expected to

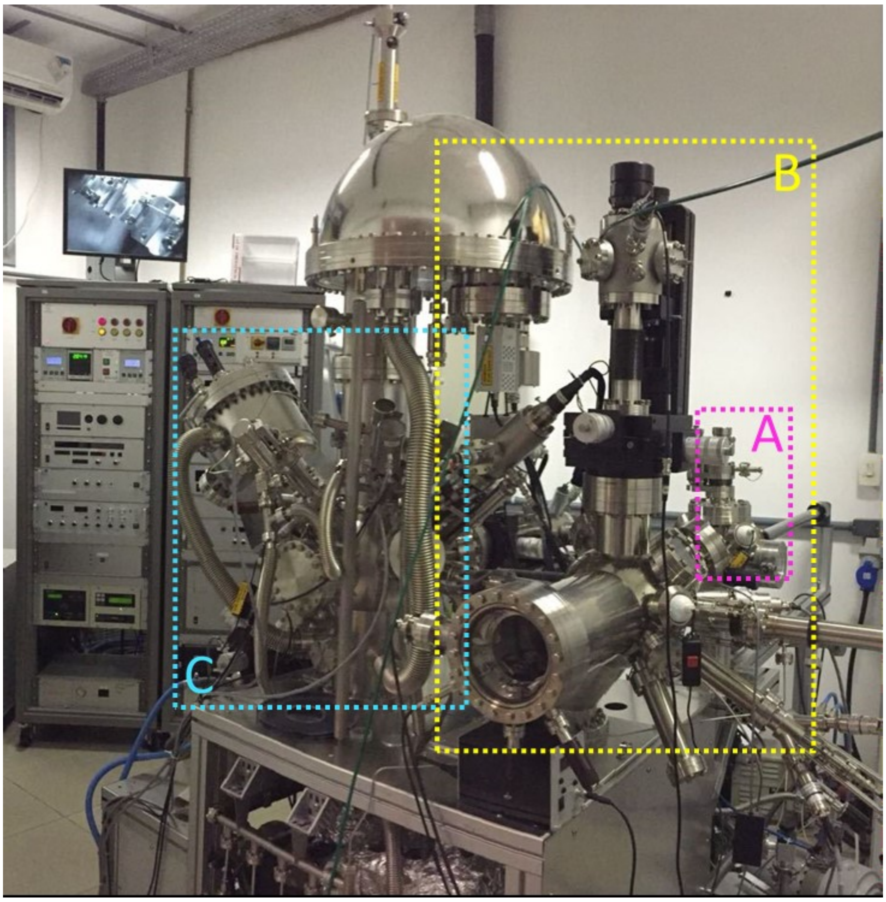

FIGURE 3.7. Photo of XPS equipment in Surface Nanostructures Laboratory. The three chambers are marked with dasehd lines: (A) Load lock, (B) Preparation and (C) Analysis.

have a temperature difference in the rate of 100 K. All the temperatures described in this proyect are refered to the measure temperature at the sample holder as mentioned before is expected to be different to the actual temperature. The cleaning procedure was carried out until no residual contamination was detected by XPS and LEED, see Figure 3.8 and Figure 3.9.

As we mentioned before in this work, our study was focus on the preparation of Mn_xO_y films on metallic substrates like Cu and Au (for doping). But it is well know by literature [107] that Cu is easily oxidized when it comes in contact with oxygen. Considering this issue that is still under investigation whether the film forms on Cu or oxidized Cu surface. We oxidized Cu (111) in one partial oxygen pressure and obtained one of the many reconstruction as already known in literature. In this chapter, the oxidized surface is used as example to explain the LEED pattern and XPS results in the following chapters. The oxidized Cu surface was obtained by heating at 550 K the clean Cu (111) at $p(O_2)=5\times10^{-7}$ mbar for 20 min.

XPS spectra of films deposited on Cu (111) will be measured with a non-monochromatic Mg Kα (1253.6 eV). We use a non-monochromatic source to avoid the overlapping between Cu 2*p* and O KLL auger. For that reason, substrate data measured with XPS were acquired with the same source, see Figure 3.8.

(a) The purple survey spectrum shows the presence of the characteristic peaks (labeled in figure) for clean copper without any contaminants like carbon (284.8 eV) and oxygen (530 eV). The blue survey spectrum is relative to oxidized Cu surface. The presence of oxygen is testified by the appearance of O 1*s* core level at 530 eV (zoomed view in the inset of Figure 3.8a), O *KLL* Auger at ~750 eV and carbon at 284.8 eV. No normalization or prior treatment was used in XPS survey.

(b) Cu 2p XPS spectra for clean and oxygen exposed surface are very similar, despite this there is a slight difference in their intensity, most visible in 2p 3/2 peak. This reduction can be associated with the oxygen layer deposited on the copper surface. For this result we can assume that the oxide is Cu$_2$O and not CuO, due to the ausence of strong sattelites approximately at 943 and 962 eV seen in literature [107].

(c) In the valence band (VB) spectra, measured with UPS, we can identify the features of clean Cu at 2.3, 2.7, 3.2 and 3.8 eV. It is possible to differentiate the contributions between Oxygen at 5, 7 eV (see inset in panel c) and substrate. Another point is the intensity drop between two peaks (3) and (4).

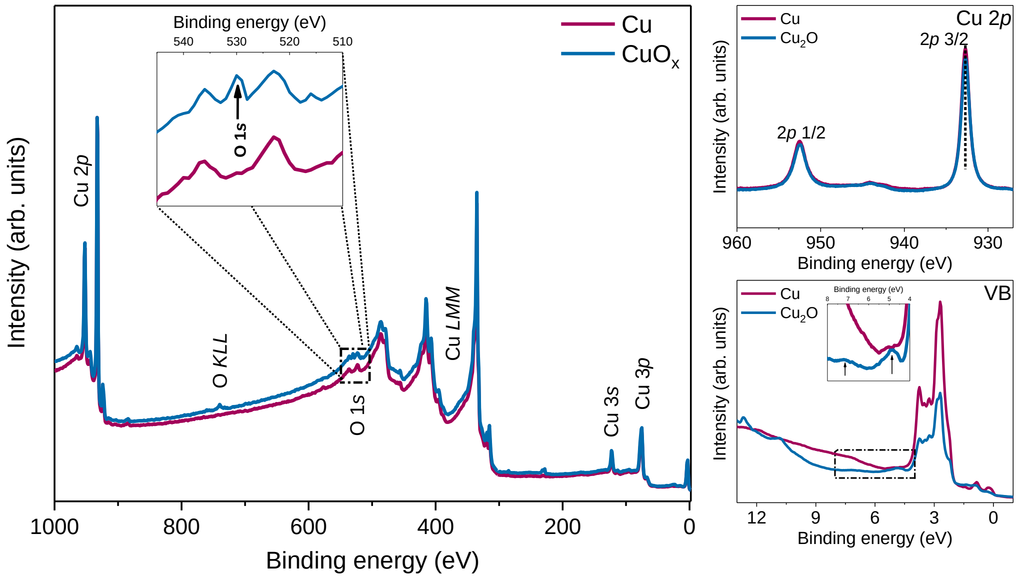

FIGURE 3.8. XPS survey (a) and high resolution (b and c) spectra of Cu(111) and oxidized Cu. (a) Characteristic peaks for Cu and O (O 1*s* core level highlighted in the inset). (b) Cu 2p XPS spectra does not show visible differences in both sample. (c) UPS spectra shows the contributions of Cu and O.

The Figure 3.9 shows the LEED pattern at energies of 45 (d), 65 (a) and 80 (b,e) eV obtained from a clean Cu (111) (upper panel) and the oxygen reconstruction on Cu (111) (bottom panel). In the case of Cu (a and b), the hexagonal pattern relative to a direct lattice parameter of 2.56 Å is observed. Well defined diffraction spots (sharp) is an indication that surface is clean, ordered and homogeneous. We use the LEEDpat program [108] to reproduce the surface structure by using its lattice parameter, as shown in panel (c) the simulation is equal to panel (a and b).

In the oxidized Cu surface (d and e) the diffraction pattern consist of the underlying Cu spots and additional spots in one direction along both in plane (111). The lattice parameters of CuO_x were estimated as a_1= 9.2 Å and a_2= 17.9 Å, by using the LEED spots distance as reference. In panel (d) there is no spot of substrate because in our system it appears only above 65 eV (a). Its respective simulation is show in panel (f). Based on both LEED and XPS results we can assume the formation of Cu_2O [109].

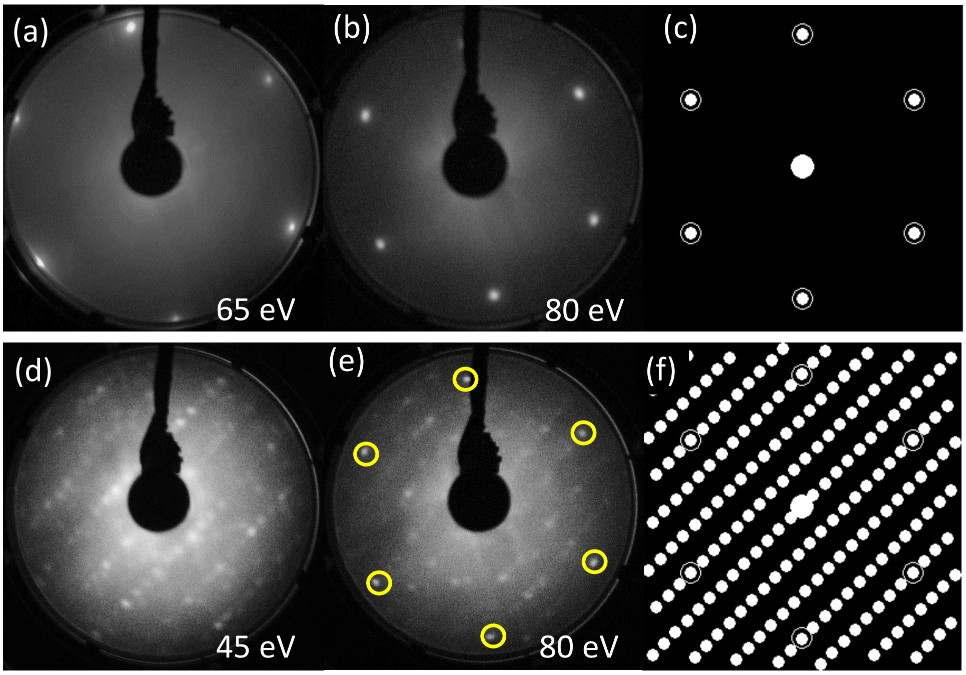

FIGURE 3.9. LEED patterns of substrate (cleaned and oxidized)at 45 (d), 65 (a) and 80 eV (b,d). (c,f) The figures represent the simulation for Cu and oxidized Cu with lattice parameter of 2.56 Åand a_1 = 9.2 Å, a_2 = 17.9 Å, respectively.

After the substrate cleaning process, our next step is the deposition of Mn pellets on clean substrate held at room temperature and by varying two different parameters in the setup of the experiment, such as oxygen pressure $p(O_2)$ and film thickness. The evaporation was followed by a post-annealing up to 550 K and cooling down to RT at same partial oxygen pressure used in deposition. The annealing was performed at low temperatures to avoid the creation of islands [20, 34]. The films preparation were performed in ultrahigh vacuum (UHV) chamber (B in Figure

3.7) with a base pressure of $7x10^{-9}$ mbar, while the pressure during the analysis was $3x10^{-10}$ mbar.

As a function of p(O_2) of either 5×10^{-8} or 5×10^{-7} mbar, we obtained two types of manganese oxides (MnO and Mn_3O_4) and as a function of the thickness we compare thin and thick films of the same oxide, as you will see in next chapters. Mn_3O_4 and MnO films were prepared by electron beam evaporation "EBE" with an evaporation rate of 1.4 Å/min. This estimation is made-up by measuring step height (~ 5 nm), as you see in (b), of manganese oxide film (30 minutes) deposited on half silicon substrate measured with AFM in tapping mode as seen in Figure 3.10(a). The selection of the silicon surface is made by opportune mask.

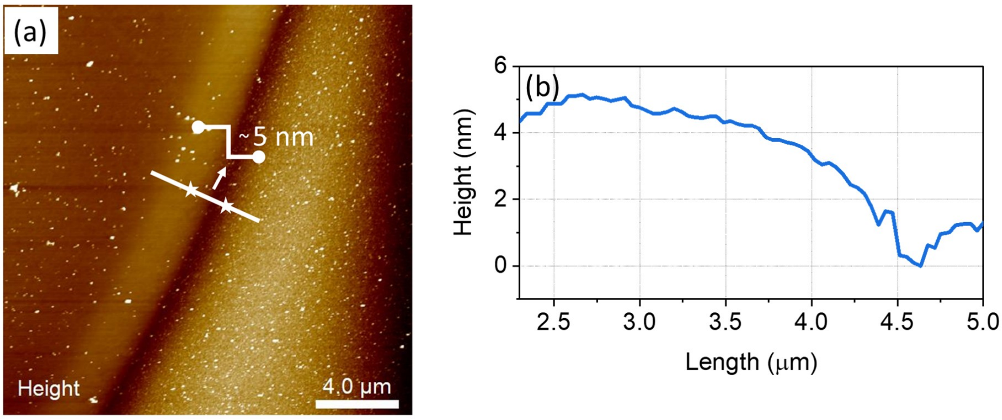

FIGURE 3.10. (a) Topographic image (AFM) of manganese oxide deposited on Si mask measured at tapping mode (4x4 um). Profile (white line) shows the step (~ 5 nm) in surface after 30 minutes of deposition. (b) Step height (~ 5 nm) measurement from manganese oxide on silicon surface.

XAS and ResPES experiments were carried at LNLS in PGM beamline at room temperature, see the figure 3.11 and the following reference for more details [110]. This Beamline is equipment with a tunnel to transfer samples among the different chambers, see the inset figure "E" three experimental chambers: (D) analysis, (E) load lock and (F) preparation. The base pressure for analysis chamber was 10^{-10} mbar, for other chambers the pressure was close to 10^{-9} mbar. The preparation chamber have the same facilities that CBPF. XPS, UPS and LEED measurements were performed in the analysis and preparation chambers, respectively to verify the correct formation of the thin films. After verification, all sources were turned off before irradiating the sample with synchrotron radiation for absorption and resonance measurements.

The deposition rate was obtained by using a quartz microbalance, whose result was not so different from the value obtained from the mask measured by AFM. We try to maintain the same growth conditions as the deposition time and oxygen pressure in order to reproduce the films made in CBPF. In order to improve the quality of films, a second or third post-annealing can be carried out, and we will see this improvement through the LEED patterns.

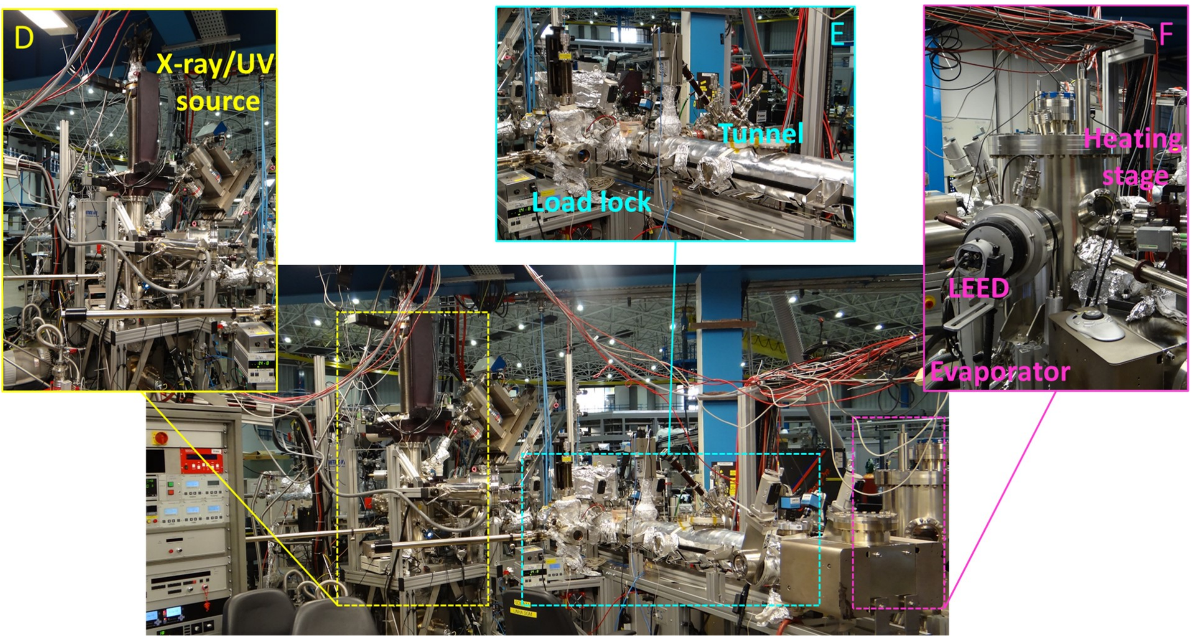

FIGURE 3.11. Photo of the PGM beamline at LNLS. The beamline is equipped with three chambers and a tunel marked in figure. (D) Analysis chamber, (E) load lock and tunel and (F) preparation chamber.

A change of substrate from Cu (111) to Au (111) was implemented for doped manganese oxide films, the principal reason was the overlapping between core levels such as Co $2p$, this feature will be important to identify the oxidation state of the dopant.

CHAPTER 4

GROWTH OF MNO ON CU (111)

It is known that MnO bulk has an insulating nature and cubic rock-salt structure. So, to avoid its insulating nature we grew films of few layers from 0.5 to 2 nm meanwhile a film of 4 nm was used as a bulk reference like cited by [37]. These films are thick enough to represent a semi-infinite crystal and avoid charging effects [20]. We determinate the oxidation state of the films by measuring the fingerprints cited in Chapter 2 through high-resolution XPS spectra of Mn $2p$ and Mn $3s$ core levels with a non-monochromatic source - Mg $K\alpha$ (1253.6 eV) as seen in Figure 4.1.

Through Mn $2p$ core level (a), the fingerprints of the MnO film formation can be identify by relating to the binding energy distance. The spin-orbit splitting located at $2p_{3/2}$ (641 eV) and $2p_{1/2}$ (652.9 eV) peak is near to 11.9 eV (indicated by the black dotted lines in figure). These values are in accordance with the literature and Table 2.1. One may also observe the characteristic satellite structure, which is less intense, localized at ~ 5.4 eV (657 eV) higher to the binding energy from the main core-level $2p_{3/2}$ peak. This is an evidence of MnO formation. We observe that the size of the satellite depends also on the film thickness of the sample [111]. An Auger broad peak “Mn LMM” is also identified at 669 eV and related to the excitation of manganese $2p$ levels [112]. The background was removed for all Mn $2p$ spectra with CasaXPS program [113], but a normalization analysis was not applied to avoid modifications in the intensity of the peaks. As expected, the relative intensity increases as a function of the film thickness from 0.5 to 4 nm. Nevertheless, we observed the peak envelope has an asymmetric shape in $2p_{3/2}$ region, more noticeable when the film is thicker. But more importantly, for all thicknesses, the asymmetric shape of the two peaks kept constant.

Further analysis of the Mn $3s$ core-level region is displayed in panel (b). This feature is most conveniently used to identify the oxide phase. The Mn $3s$ peak region presents two multiplets splitting peaks separated to 6.0 eV (ΔE). This separation is due to exchange interaction between 3*s* and 3*d* electrons [24] and its magnetic moments involved. So, when the quantity of manganese deposited is low, Mn 3*s* is difficult to be detected [24], and of course making it difficult to analyze the separation between peaks. Mn 3*s* features of thin films (from 0.5 to 2 nm) are significantly affected by the appearance of Cu 3*p* peak (79 eV). In literature the intensity ratio between M 3*s* peaks is nearly 1.4 [20] but experimentally we found that I_R for our films is in the range of 1.4 to 1.8. In all the spectra, we remove the background and the contribution of Cu 3*p*, leaving only Mn 3*s*. A shift is observed by increasing the film thickness but the Δ is kept constant, we relate this phenomenon to the strong interaction between film-substrate for thinner sample.

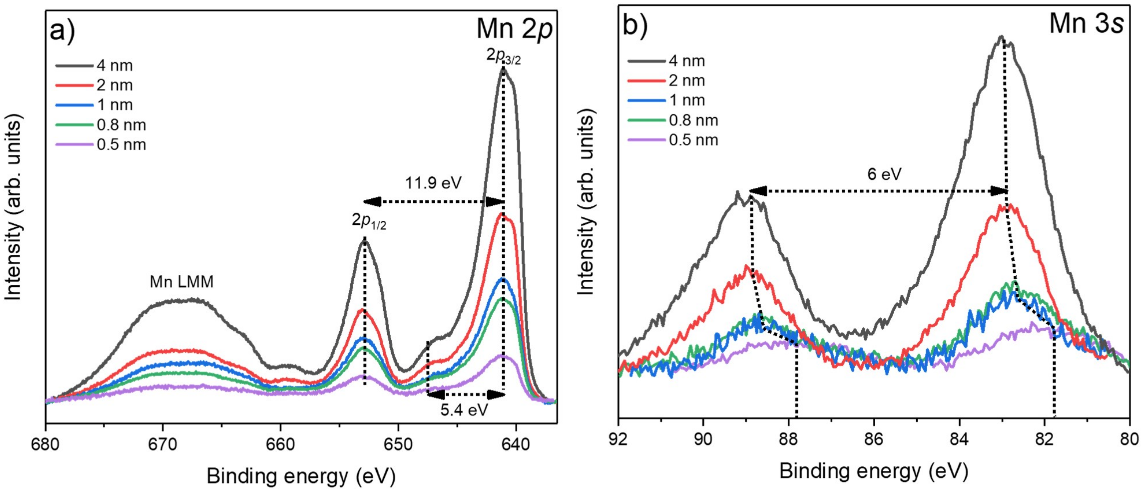

FIGURE 4.1. HR XPS spectra of several MnO films deposited: (a) Mn 2*p* and (b) Mn 3*s*.

Further, we have measured the LEED patterns of all the MnO films. And interestingly two different patterns were found among the five films. In films the Cu(111) spots are still visible. In patterns, the Cu (111) spots as well as those related to the MnO film are highlighted as follow: yellow circles for the Cu substrate and green, red and blue for MnO films. Since the substrate spots are yet identified, we have considered the Cu surface lattice parameter (a=2.56 Å) as a reference to estimate the lattice constant of MnO films. LEED pattern at 25 (e), 30 (a), 50 (b and f), 65 (c) and 75 (g) eV were measured for all films but only two of them were shown in Figure 4.2. For thin films as 0.5 and 0.8 nm (top panel), we estimated the lattice parameters as $a_1 = a_2 =$ 6.32 Å with angle of 90º between lattice vectors.

These results were used by LEEDpat software [108] to obtain the simulation showed in Figure 2d and 2h and with that information the phase was catalogued as MnO (111) with a reconstruction of c(2x2). On the contrary for thick films from 1 to 4 nm, the surface lattice vector is given by a_1=4.5 Å and a_2=6.32 Å with angle of 54°. In simulation figure, the white spots of Cu (111) are forming a hexagonal pattern as expected, while green spots belong to the six domains of MnO with a separation angle between them of 15. This results match to the marked spots in diffraction patterns. For these films, the phase was catalogued as MnO (100) with a reconstruction of (1x2) due to the rearrangement of the atoms. This phase is well ordered and stable at low temperature (≤ 350 C) and low p(O_2). However, an increase in temperature in UHV or p(O_2) transforms the phase (100) into (111), although it depends a lot on the thickness of the film [43]. Our general findings suggest that oxide thin films display predominantly the (111) plane and thick ones exhibit mostly the (001) plane.

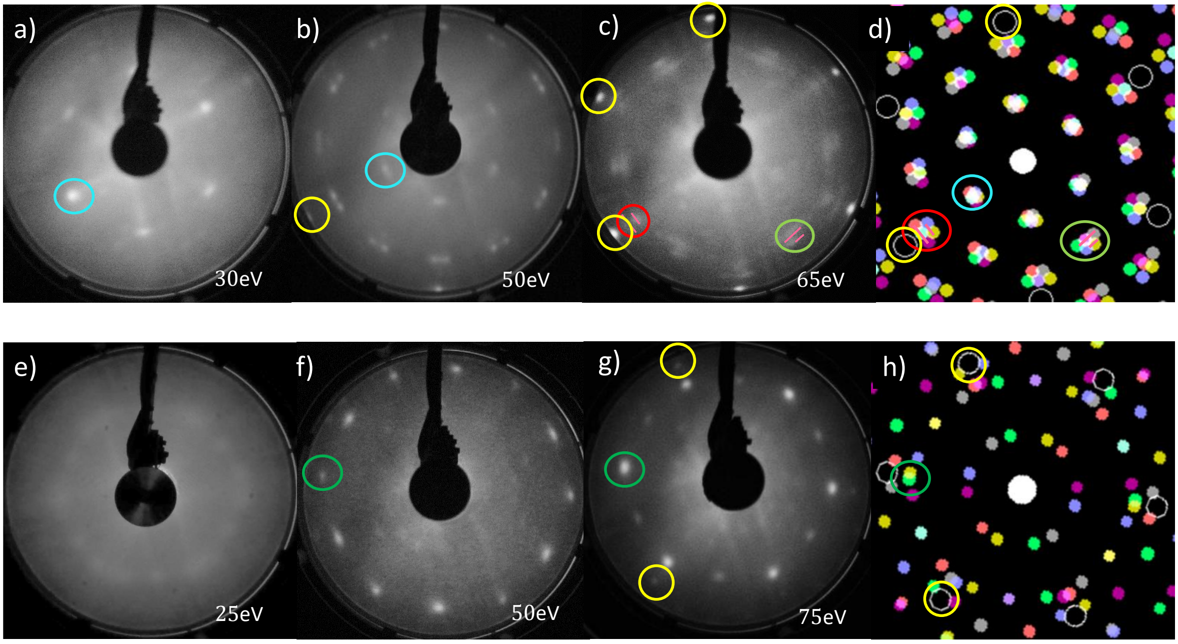

FIGURE 4.2. LEED patterns of two MnO films at energies of 50 (a,e), 65 (f) and 75 eV (b). The panels represent the simulation for MnO film (c,g) and their respective real space (d,h).

The valence band (VB) spectra of Cu (111) surface and MnO films were measured by UPS (He Iα) and with synchrotron radiation as showed in Figure 4.3 (a) and (b), respectively. According to the literature, all manganese oxides have 3 features: a narrow peak O 2*s* at ~ 23 eV, a O 2*p* at ~ 7 eV and an intense feature Mn 3*d* at ~ 4 eV, the latter two in a hybridized state (overlapping each other) between ~ 4 - 10 eV [48, 114]. The VB for a thin (0.5 nm) and thick (4 nm) film, additionally the clean copper (pink) are plotted in panel (a). For Cu (111) is possible to recognize its features at: 2.2, 2.7, 3.2 and 3.7 eV. We can observe the modifications of valence between MnO films: for 0.5 nm (purple) a clearly enhancement is observed at 3.5 eV and a shoulder appears discreetly at 2.1 eV. The continuous enhancement of this features increases as the thickness increases to 4 nm (black). For 4 nm film, a bigger shoulder is formed at 2.1 eV, including peaks at

3.1 and 3.5 eV. For this film, the substrate is no longer visible, only film features are visible as manganese “3d” states. The influence of oxygen vacancies on the VB structure (presence of O) and the hybridization state between O 2*p* and Mn 3*s* [111]. The characteristic satellite of MnO (crystal) seen in the Mn 2*p* core level should be seen in the Valence Band at the same distance 6 eV but that does not happen in our case. We use the Al source of XPS. So, by using a variable source like synchrotron we can observe the characteristic satellite.

Resonant photoemission measured with synchrotron radiation at LNLS was employed as a new tool to understand with more details what happens in the valence band of films. All the spectra were normalized to 1 for convenience. Initially, we select two energies: 851.4 eV, energy related to Mn 2*p* and 100 eV, lower measurement resolution. Even with low resolution compared to UPS measurements, we observe the increase of intensity near at 3.5 eV (MnO film contribution) specially for thick film and with low-energy (100 eV). For 851 eV the σMn/σO is 4.9 and for 100 eV is 2.1. By increasing the thickness from 1 to 4 nm, the hybridized state O 2*p* - Mn 3*d* are more visible at both energies (blue and green) and for thin film it is more difficult to distinguish between the contributions of the film and the substrate. The peak at 22 eV were assigned to O 2*s* and the shoulders at 11.2 and 14.6 eV to copper satellites. But unexpectedly we cannot identify the satellite at 6 eV, this could mean that the satellite is not related to bulk but to the surface of MnO. Therefore it appears only in Mn 2p and not in VB. We already mentioned earlier that the intensity of the satellite depends on the sample, and this is because it depends on the Q parameter ("core-hole"-"d" electron Coulomb attraction). Thus, the satellite increases with increasing Q. And Q is higher for Mn 2*p* than other features like Mn 3*s* or VB. Using variable energy such as the Mn 2*p* threshold, the satellite and other features can resonate and be more visible. This resonance comes from a direct emission of the 3d state [111].

Another technique used to identify the oxidation state of the film was XAS. These measurements were performed at PGM beamline in the National Laboratory of Synchrotron Radiation (LNLS), in Campinas, Brazil. Initially, XAS spectra was measured in UHV environment for copper (orange) and copper oxide (blue). We use the oxidized substrate as reference to identify the oxide contribution and compared to film results. The Figure 4.4 shows the Cu $L_{2,3}$ (a) and O K-edge (b). The background was removed for all spectra, but no normalization was performed for this case to avoid changes in the intensity.

In panel (a), we have not observed significant differences on the peaks energy positions, except fot the intensity, between both spectra. The Cu spectrum has three strong peaks between 930 and 950 eV, this is in good agreement with the literature, but this is not the case for copper oxide. The CuO_x spectrum have only one strong peak at 934 eV at the same region of Cu as indicated by the literature [109, 112]. We know that only the surface was oxidized, so if we consider that

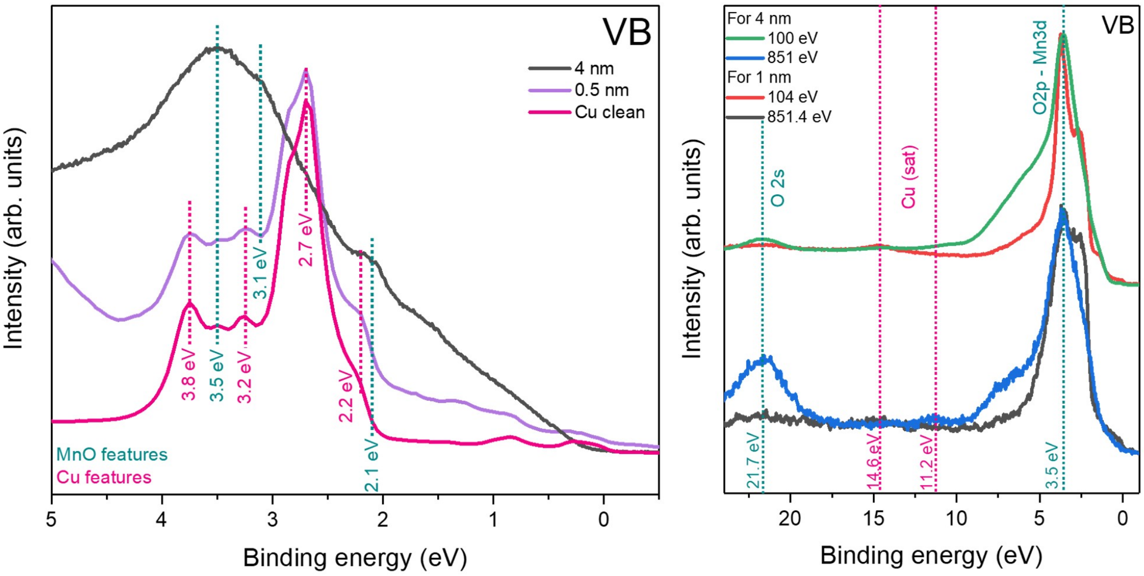

FIGURE 4.3. Valence band spectra measured at He Iα energy as a function of thickness for different $\mathrm{Mn_xO_y}$ thin films.

assumption this layer oxide can be so thin that is not possible to be recognize with XAS. By the way, we will focus on O XAS to find the stoichiometry of the oxidized surface.

In panel (b), great differences are observed in both oxygen spectra, as the strong peak at 530 and 532.5 eV for copper oxide as shown by the difference between CuO$_x$ - Cu clean. The peak at 530 eV is attributed to hybridization of O $2p$ with Cu $3d$ electrons, according to other reports this is characteristic of CuO. And the peak at 532.5 eV is characteristic for CuO$_2$. The results can indicate a mixture of this two oxides at the surface. At higher energies (above 535 eV), the features are related to hybridized O $2p$ orbitals with Cu $4sp$ band. For copper clean, initially no oxygen sinal was expected but it was note a little contribution (orange spectrum) near of 530 eV but with less intensity compared to copper oxide. This is probably due to contamination (low quantity of oxygen) when transporting the sample from the preparation to the analysis chamber.

XAS measurements of MnO films are shown in Figure 4.5. The (top) manganese $L_{2,3}$-edge and (bottom) oxygen K-edge XAS spectra are shown for two samples (1 and 4 nm) with the same phase - (100) (1x2), with transitions as Mn $2p \rightarrow 3d$ and O $1s \rightarrow 2p$ for Mn and O, respectively. The background was removed and a normalization in a "single point - 645 eV and 547 eV for Mn and O edge respectively" was applied for all spectra. The data were acquired with two angles as function of the experimental geometry between beam and sample: Normal incidence - 0° (almost perpendicular to the substrate surface) and Grazing incidence - 54°. So, we expect that measurements with grazing angle can provide results of film surface and possible film termination. On

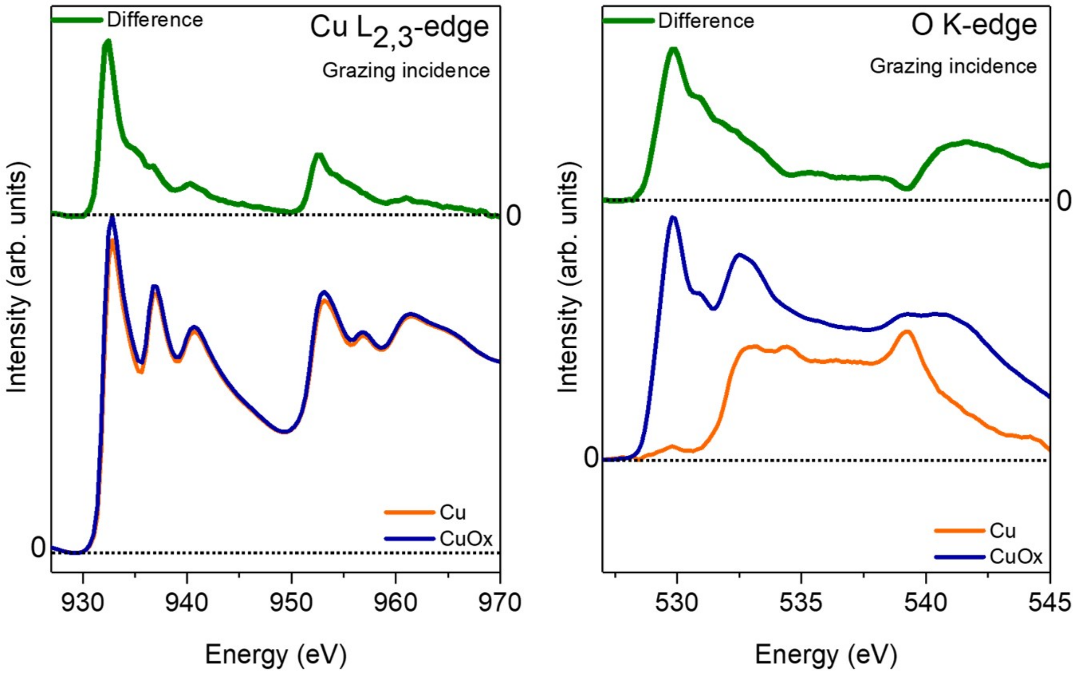

FIGURE 4.4. XAS spectra for Cu (orange) and CuO_x (blue) measured at grazing incidence for Cu $L_{2,3}$ and O K-edge, respectively. The green spectra is the difference between CuO_x and Cu.

the other hand, perpendicular measurements provide us bulk results.

In the figure 4.4 top panel, the $L_{2,3}$ edge correspond to the transitions from $2p_{3/2}$ and $2p_{1/2}$ states to $3d$ unoccupied states localized on manganese ions. MnO XAS spectra, with Mn^{2+} high-spin, are characterized by having two line regions: L_3 from 636 to 646 eV and L_2 from 646 to 656 eV, its separation is due to the spin-orbit interaction and is independent of the oxidation state [68]. L_2 region does not show big changes, that is why we will focus in L_3 edge. Through these spectra, we confirm again the oxidation state of MnO, as seen in Figure 2.4 [68, 111]. For L_3 region i.e. the t_{2g} state with d_{xy}, d_{xz} and d_{yz} have the highest level at 639.8 eV for d_{xy} [111]. At first glance in both top panels are slight differences marked but arrows, with the aid of subtracted spectra (0° and 54). We notice specially two differences at 638.6 and 639.8 eV, regardless of the thickness of the film. But actually the intensity of the spectra was normalize, so differences about the intensity are not completely valid for our results. So, for ResPES measurements we will just consider the two peaks of Mn edge (black and blue): 638.6 and 639.8 eV.

In the figure 4.4 bottom panel, the transitions for O K-edge are from O $1s$ to $2p$ state hybridized with Mn $3d$ (529-533 eV) and multiple absorption peaks (533 - 546 eV). We notice that the peak increases near at 530 eV only for thick film. According to literature [67], this peak

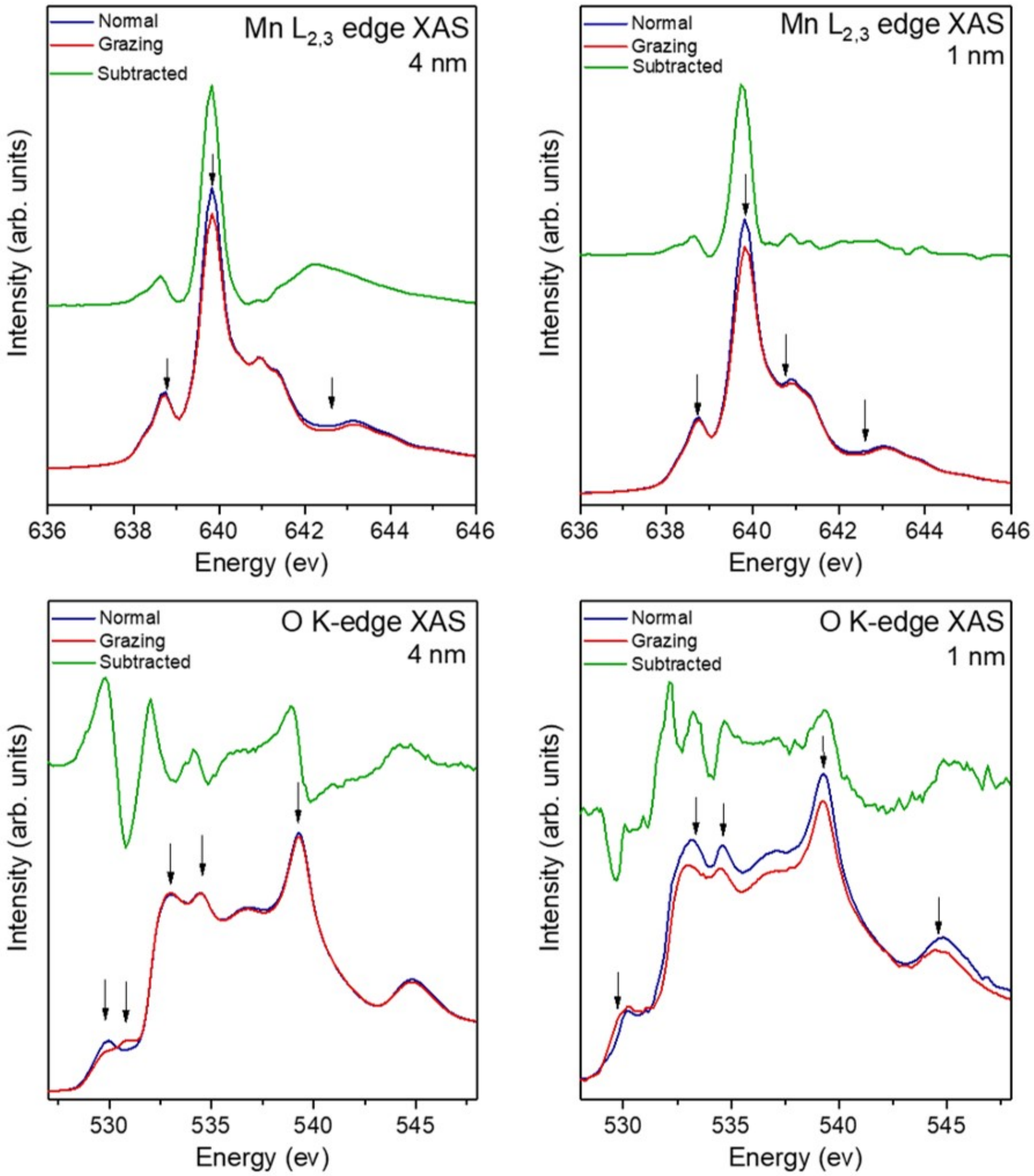

FIGURE 4.5. Manganese $L_{2,3}$-edge (a) and O K-edge (b) XAS spectra of two MnO films of 1 (right) and 4 nm (left).

represents the oxygen at surface, higher exposure of oxygen and longer time of post-annealing at same oxygen pressure. So, it is accurate to assume that this contribution is related to surface contribution than bulk, and it is expected for a grazing measurement. But this change is not seen on thin film probably due to little amount of oxygen caused by deposition and the contribution of copper oxide. Forward, we labeled the peaks as literature: (1) near to 530eV is related to the oxygen at surface. (2) The region from 533 to 535 eV is assigned to transitions between O 1*s* to Mn 2*p*-3*d*. (3) From 535 to 545 eV, we found the unoccupied O 2*p* mixed with 4 *sp* state. (4) Above 550 eV, there is the influence of the multiple scattering [67].

Previously, we made a comparison as a function of angle for the same film (thickness and phase). We discovered some differences like the little enhancement of intensity for O edge for example. Now, we are interested in a surface comparison as a function of thickness measured at the same angle i.e. 0° or grazing. Figure 4.6 shows this comparison, for Mn edge (left) we notice only in the subtracted spectra (green) differences about intensity again (639.4, 639.8 eV and 638.6 eV). On the other hand, a shift is clearly visible for O K edge at 530 eV and between 533-535 eV. Obviously we assume the shift is a consequence of the thickness, the measure of thin film is influenced by the oxidized substrate (peak at 530.2 eV) and thick film is consider as bulk.

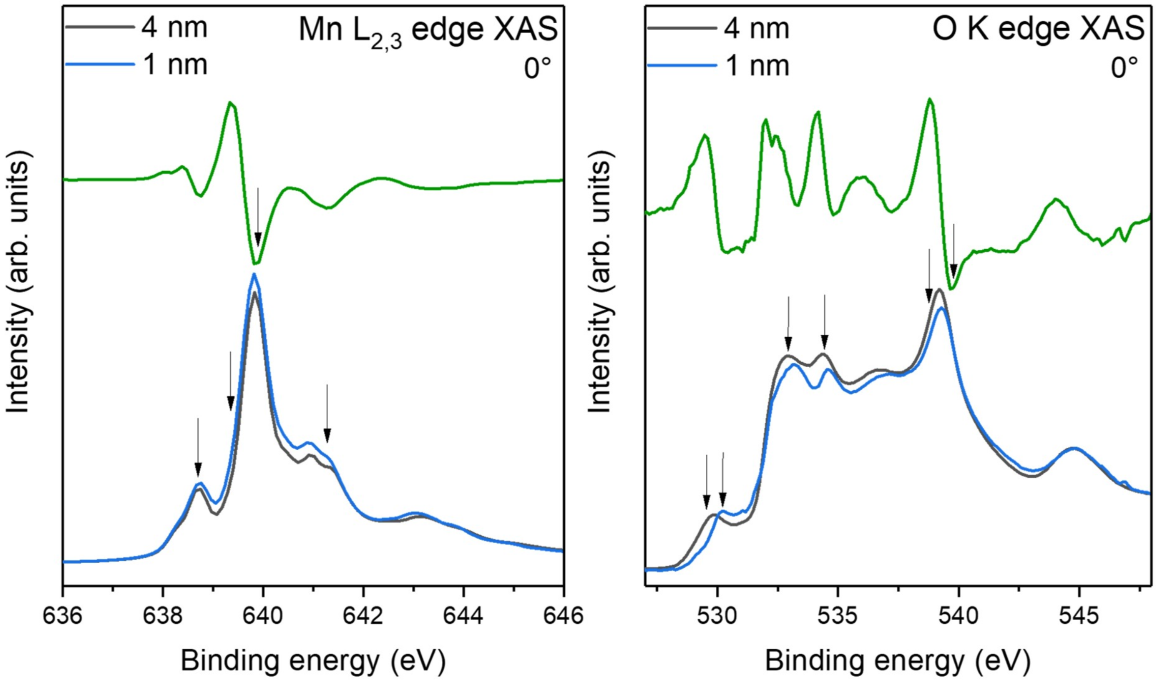

FIGURE 4.6. Manganese $L_{2,3}$-edge (a) and O K-edge (b) XAS spectra of two MnO.

In addition to measurements of XPS and UPS, a more detailed study of valence band "VB" structure with resonance photoemission "ResPES" in TMs has been a matter of interest in recent years [111]. ResPES experiments were measured at different incident energies, these energies were selected from Mn L_2-edge and O K-edge recorded at 2*p*-3*d* absorption threshold.

The Figure 4.7 shows the ResPES results for Cu and CuO_x measured at different incident energies come from Mn $L_{2,3}$ edge. In panels, we observe the valence band (VB) between the region from 8 to -1 eV. No normalization was performed in all spectra and the fermi level E_F (0 eV) was used to calibrate the spectra. In XAS spectrum, the following energies: 620, 630 and 670 eV are located in flat regions, so no enhancement should be seen in valenve band, we refer these energies as "off-resonance". Other selected energies that show an enhancement are considered as "on-resonance".

For the Cu substrate (a), we mainly notice the features peaks at 2.3 and 3.5 eV (black dotted lines), both peaks are sharp with a deep "valley" between them. For CuO_x (b), these features are observed at same positions, but instead of being sharp peak at 3.5 eV, it is thicker now, and the region of "valley" is less deep. These changes may be due to a new contribution close to region ~ 3.1 (red dotted line) related to the oxygen at the crystal surface.

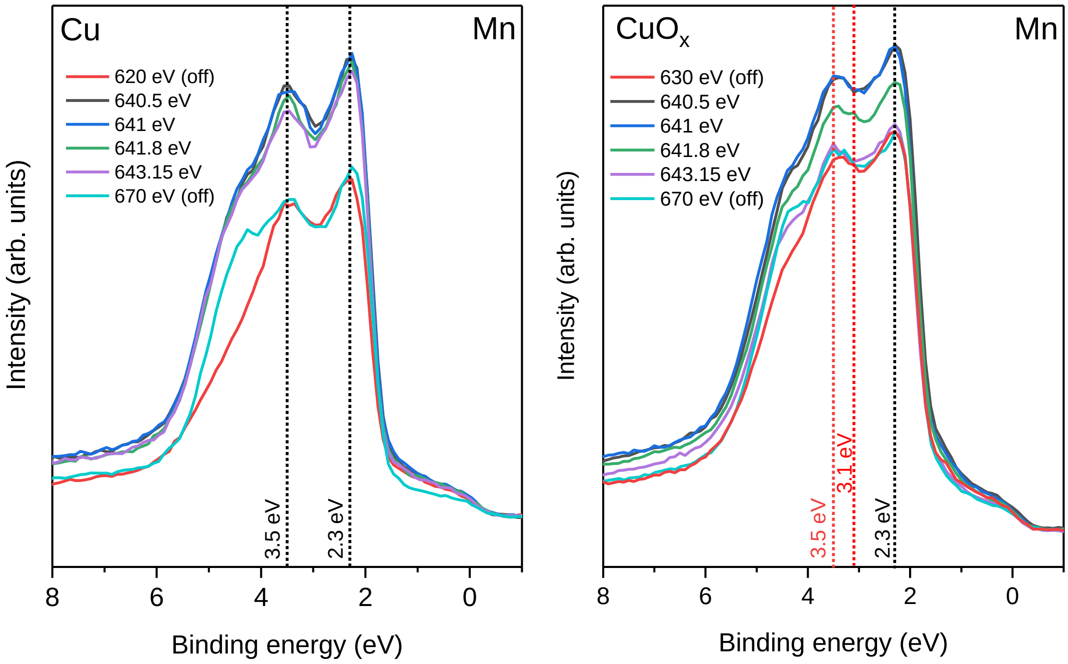

FIGURE 4.7. ResPES spectra of Cu (left) and CuO_x (right) measured at selected energies of Mn $L_{2,3}$ edge. The features for copper and copper oxide are marked by black and red dotted lines, respectively.

If we assume that these small changes in valenve band (VB) is caused by the presence of oxygen at the surface, we expect to detect this phenomenon in the next results measured by using energies of O K-edge.

ResPES spectra measured with energies of O K-edge are show in Figure 4.8. As the same for

Mn, energy at 590 eV is "off-resonance" according to O XAS and show no enhancement as you see in the figure (brown spectra). The valence band is displayed at the same region (8 to -1) that Figure 4.7. For clean Cu (a) and CuO$_x$ (b), we figure out that VB shape has changed to previous results. "On-resonance" energies an enhancement at 2.7 and 3.5 eV (red dotted lines) are more visible unlike panel (b) in Figure 4.7, where the peak was only thicker. The black dotted line corresponding to substrate at 2.3 eV is no more visible.

The fact that we observed an enhancement for "clean" copper, indicate us that substrate is not completely clean, as we already saw with the XAS spectrum. For CuO$_x$, the enhancement and the FWHM (black horizontal line in both spectra) show an increase probably to a higher quantity of O.

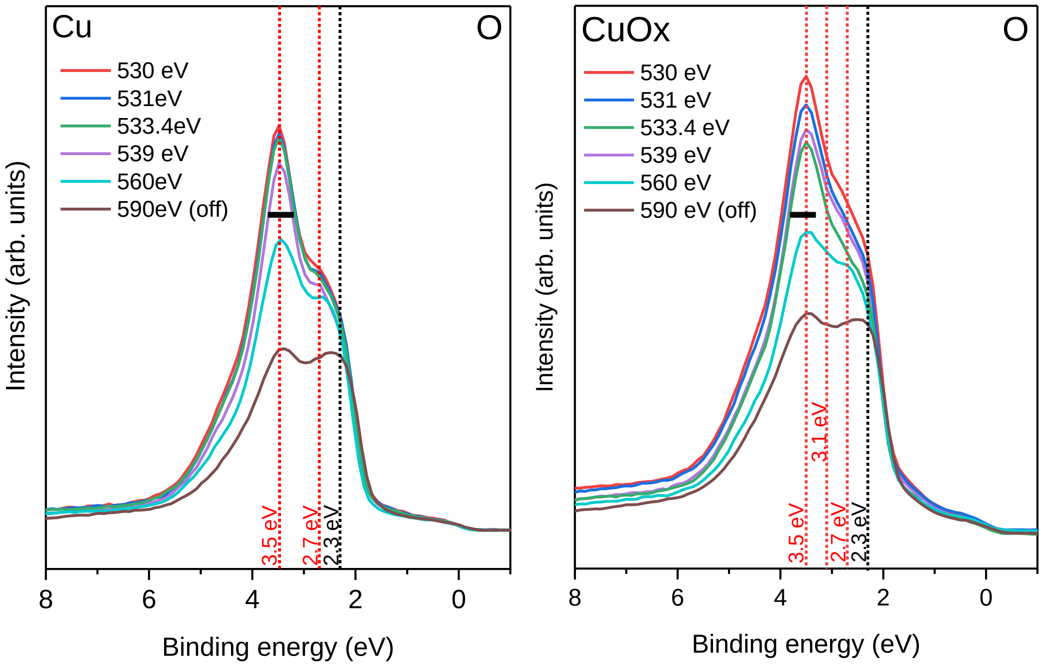

FIGURE 4.8. ResPES spectra of Cu (left) and CuO$_x$ (right) measured at selected energies of O K-edge. The features for copper and copper oxide are marked by black and red dotted lines, respectively.

For the case of MnO, in the Figure 4.9, we observed the ResPE spectra for energies from 630 eV to 643.1 eV normalized to maximum intensity for low region - 3.5 eV. With this normalization, we lose information about intensity but on the contrary we notice another features like augers and satellites marked as pink and blue dashed lines in graphic for substrate and thin film, respectively. All the spectra were calibrated by using the XAS spectra and the position of core leve peaks as Mn 3p (BE = 47.8 eV) and Cu 3p (BE = 75 eV). We divided the figure in two regions, the first from -2 to 18 eV and the second from 18 to -85 eV. In first region we notice an enhancement at 3.5 eV, same position as we saw in valence band measured by UPS/XPS. If we compare these results with the ResPES for Cu clean, it is clear that this enhancemente is from Mn 3d states. An hibridized state is marked between 4-7 eV. At ~ 10 eV we see the appearance of a new feature, we rule out that it is an auger because it does not seem to shift as a function of energy and it does not belong to the substrate either. Which leads us to believe that it is the satellite of MnO, and apparently has a resonance behavious. The spectra is displayed in second region in such a way that the auger $MnL_3M_{23}V$ (with KE= 582.4 eV) shift is better observed.

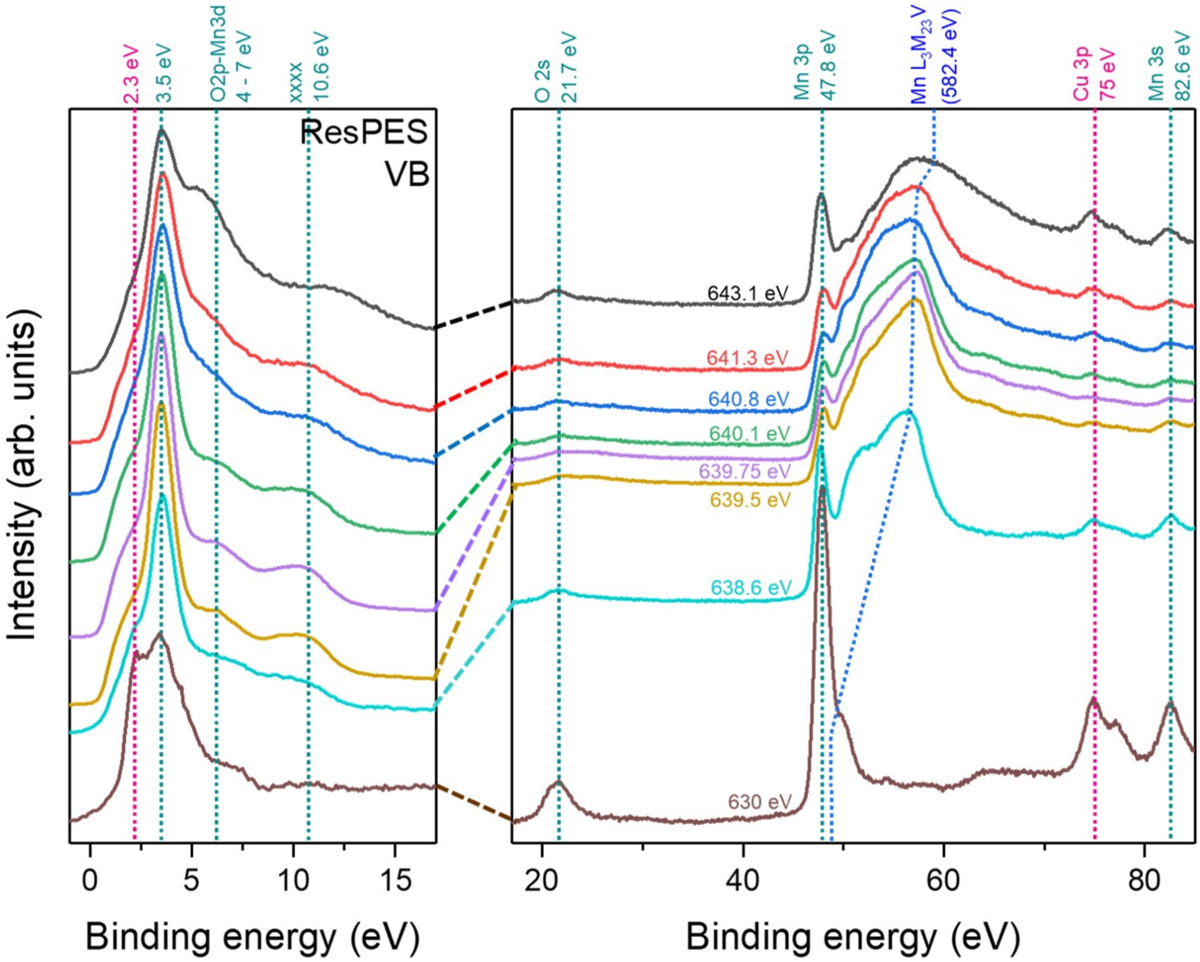

FIGURE 4.9. ResPE spectra normalized and calibrated for MnO films at selected energies (different colors) using the Mn L_2-edge threshold. The spectra were separated in two regions.

The next Figure 4.10 shows the valence band for the first region for several MnO films . The background was removed for all spectra and calibrated by using Cu 3p peak. A great enhancement at 3.5 eV region from 638.6 to 643.1 eV is notorius, with a maximum intensity especially at 640 eV, we called this spectrum as “on-resonance”. The 630 eV and other energies not recorded here do not show great or any changes in intensity, we refer these to "off-resonance" spectra. The peaks at 1.3 (e$_g$), 2.3 (t$_2g$) and 3.5 eV are considered purely substrate contributions and were shown in few papers about resonance photoemission. In the case of MnO, we perceive clear differences such as the appearance of a peak at ~10 eV.

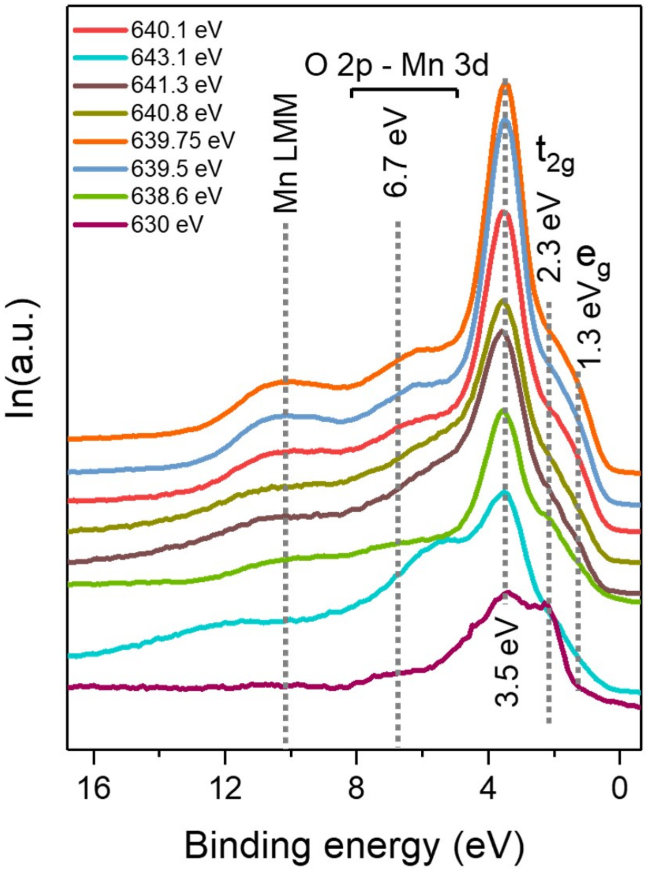

FIGURE 4.10. No-normalized ResPE spectra of MnO films at selected energies for Mn L$_2$-edge threshold. The peaks were labeled to identify the contribution of each element.

The difference between MnO and copper clean measured at 640 eV (on-resonance) are displayed in the next Figure 4.11, 4 nm (left) and 1 nm (right). For clean Cu (black line), we notice no major differences in both panels but this is expected as there is no contribution from any adsorbate in the surface. But for the MnO (red spectra), we see big differences that are more noticeable in the difference (blue dotted line) between film and substrate. For example in the $3d$ feature the states t$_{2g}$ and e$_g$ overlap the unhybridized contribution of O $2p$, showing only two peaks at 3.5 (is the maximum intensity) and 1.7 eV, respectively. From the states hybridized with O $2p$, we see that there is also a resonance marked at 6.4 eV, the feature at 10 eV that has undergone an enhancement can only be the characteristic satellite of MnO. Finally, it is more difficult to distinguish contributions for thin films due to low intensity.

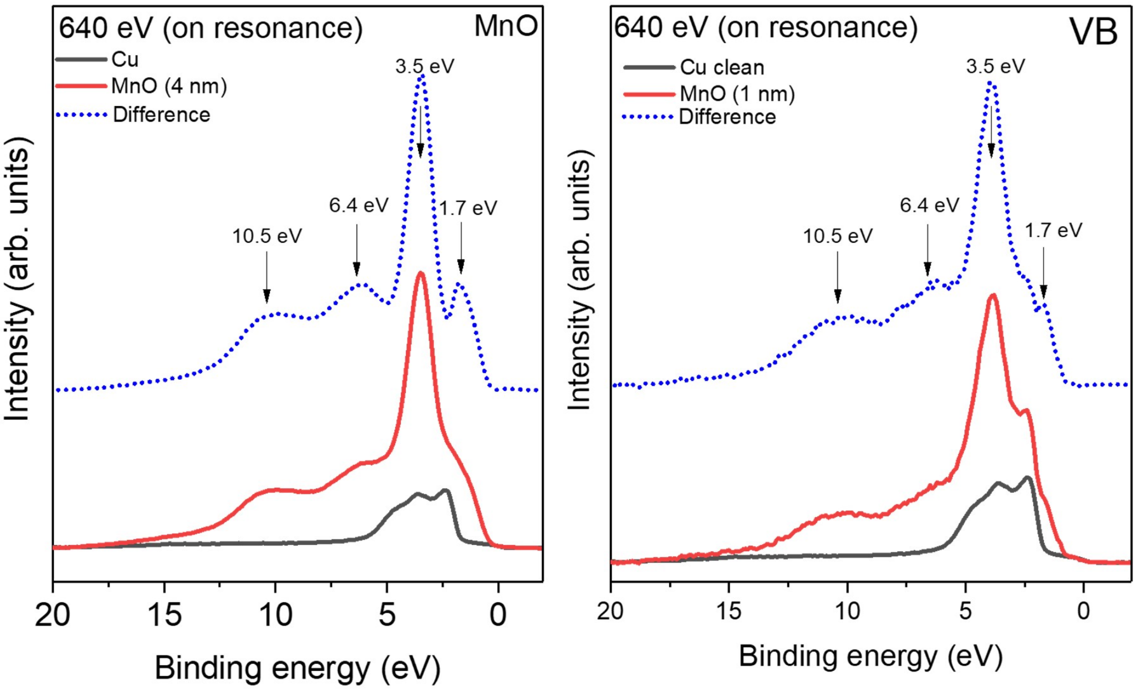

FIGURE 4.11. ResPE spectra normalized and calibrated of MnO and Cu at one selected energie 640 eV (on resonance). The dotted spectra is the difference between film and substrate.

Like Mn region, with O energies (figure 4.12), we divide the spectrum into two regions. The first from -2 to 12 eV and the second from 12 to 85 eV with the same calibration treatment and removal of the background. The shoulder at 2.3 eV and the Cu $3p$ core level are substrate features used for calibration. On the contrary that Mn, in the first region it was not necessary to use a normalization since there is no enhancement in the spectra at 3.5 eV. So, we confirmed that the increasement is related to Mn states. This absence of resonance can also be noted by the low intensity of the hybridized state at 7 eV, showing that in this state the predominant state is the Mn $3d$. Therefore it is normal for the "$3d$" to have a resonant behavior with Mn energies. Also, it is not possible to recognize the state O $2p$ - Mn $3d$ in figure due to the prominent auger contribution, labeled as O KVV (KE = 512.3 eV). The peak below the Fermi level (red spectrum) is due to the behavior of the energy harmonic of the selected photon, in this case 530 eV. The beam is initially diffracted to select a specific energy (530 eV) and the harmonic (1060 eV) is also transmitted but with less intensity. So the peak at -1 eV is the same Auger peak of oxygen but with incident energy of 1060 eV. In the second region, we show the augers scattered throughout the region as function of energy, each one was named based on the NIST database: O KL_1L_1 with KE = 477 eV and O KL_1L_{23} with KE = 492 eV (KE: Kinetic energy) [112].

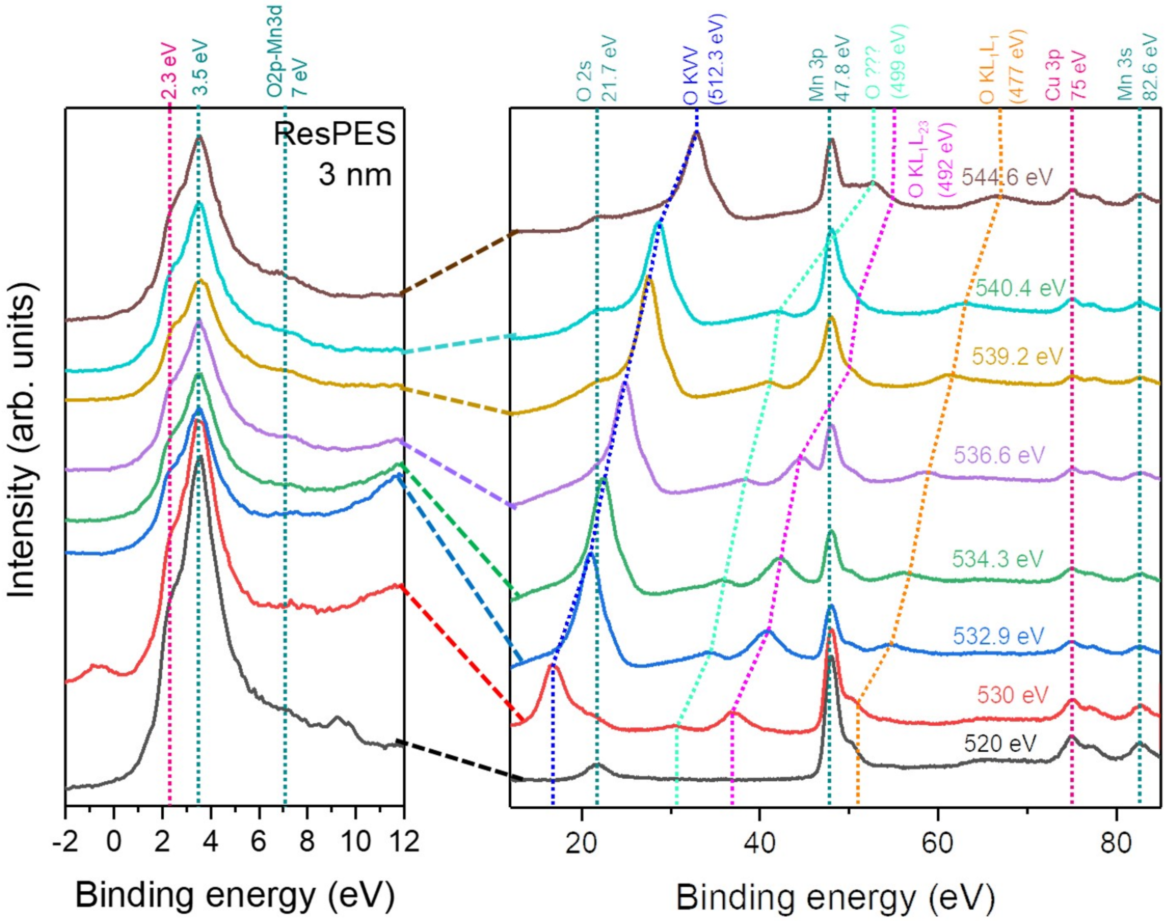

FIGURE 4.12. ResPE spectra normalized and calibrated for MnO films at selected energies (different colors) using the O K-edge threshold. The spectra were separated in two regions.

Partial conclusions

We conclude that the sample preparation at low oxygen pressures (5 x 10^{-8} mbar) we obtained MnO according to the XPS results. The Mn 2*p* core level showed the presence of a satellite at 5.4 eV. Also the separation between the Mn 3*s* peaks gave a value of 6 eV. Both results are characteristic of MnO. Through LEED patterns, we saw that for thin films we obtained the phase (111) and for thick films it was the phase (100).

The contribution of each element was seen by XPS/UPS measurements in the valence band region. The features for Cu (111) were recognized: 2.2, 2.7, 3.2 and 3.7 eV. An enhancement at 3.5 eV is seen with both techniques. By increasing the thickness from 1 to 4 nm, the hybridized state O 2p - Mn 3d and the enhancement are more visible.

Through Cu XAS spectra, we consider the mixture of two oxides at the surface: CuO (peak at 530 eV) and CuO_2 (peak at 532.5 eV). We confirm again the oxidation state of MnO through the XAS spectra. As a function of thickness, we found a shift for O K edge at 530 eV and between 533-535 eV. This result is due to the influence of the oxidized substrate on the film.

ResPES measurements for clean Cu and oxidized Cu by using O energies indicate that the substrate is not completely clean. For (4 nm) MnO resonance spectra, we labeled the augers and film contributions (both Mn and O energies). In the difference spectra between film and substrate, we observe the enhancement at 3.5 eV and 1.7 eV, are related to the T_{2g} and eg state.

CHAPTER

5

GROWTH OF MN_3O_4 ON CU (111)

In the previous chapter we talked about the growth of MnO at a certain $p(O_2)= 5x10^{-8}$ mbar, since now our objective is the formation of an oxide with a higher oxidation state. We explored to increase $p(O_2)$ to $5x10^{-7}$ mbar but keeping the other parameters the same. We already saw in Chapter 2 several references using this strategy. The films were taken to the vacuum chamber at the CBPF to begin their analysis. From the beginning we found differences with the results of the previous chapter, which led us to believe in the formation of another manganese oxide.

The high resolution XPS spectra for core levels as function of their thickness is depicted in Figure 5.1. In Mn 2*p* core level (a), we observe that there is no satellite at 6 eV above 2p3/2, thereby discarding the existence of MnO but no the existence of another manganese oxide like Mn_2O_3 or Mn_3O_4. We note that the intensity of the spectra and the line shape varies as function of thickness, i.e. this variation is compatible with the amount of material deposited on the substrate. Another characteristic that eliminates the formation of MnO is the distance between the 2*p* peaks, which has been reduced from 11.9 eV (MnO) to 11.7 eV (Mn_xO_x). Also, we observe that the line shape changes from flattened (0.7 - 1.4 nm) to sharp (3 - 7 nm), this modification is attributed to the effective interaction of thin film with the substrate, the copper or copper oxide. Just like MnO, we identify the oxidation state by measuring a second core level, cited in chapter 2, like the Mn 3*s* (b). A shift of 0.2 eV is observed between thin (0.7 - 1.4 nm) and thick (3 - 7 nm) samples, this effect is also attributed to the film-substrate strong interaction for thin films. For thick films this effect is despised. But the Mn 3*s* exchange energy split separation is 5.6 eV for all cases and remains constant. Based on literaure and the table 2.1 this value is more compatible with Mn_3O_4 than Mn_2O_3 or other manganese oxide.

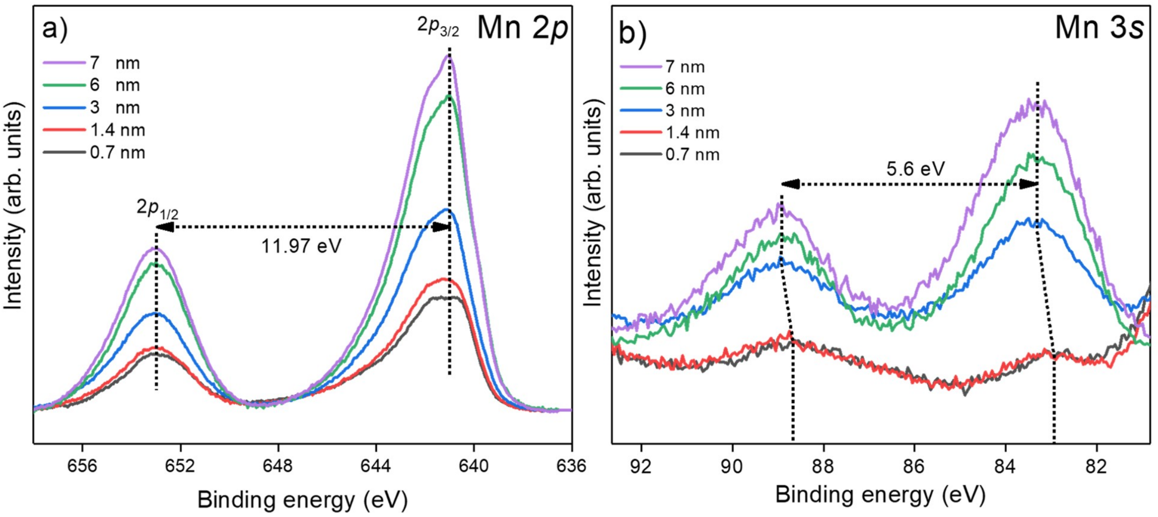

Figure 5.1: HR XPS spectra of several Mn$_3$O$_4$ films deposited and annealed at 5×10^{-7} mbar. (a) Mn 2p and (b) Mn 3s.

Once the formation of Mn$_3$O$_4$ has been confirmed, we must remember that we are facing an oxide with two oxidation states "2+" (tetra) and "3+" (octa). The ion "2+" has a final d^5 electronic state with a high spin state while the ion "3+" has a final state of d^4 with a low state spin [115]. We carry out a more detailed study of the Mn 3s of almost all the samples as shown in the following Figure 5.2. All the spectra were fitted with a lineshape of GL(30) and FWHM of 2.2 except for the satellite that appears in the thickest films, the other parameters were left free.

For 0.7 nm, we have two peaks with ion 2+ separated by 6 eV, this value has already been verified with the results of MnO (2+) from the previous chapter. The ratio between the itensities of the two peaks is 0.43, a fairly low value compared to the 0.75 given by the literature. This difference in intensities can be caused by the thin thickness of the film, which means that the surface of the substrate has not been completely covered. That is, the growth was in the form of islands, and the "x" contribution may be due to the interaction with the crystal. For 3 nm which is already a considerable thickness and not thin, we notice that the contribution "x" has disappeared (not influence of the substrate) and now we see the contribution of the two oxidation states: "2+" and "3+". The difference between the "2+" peaks is still 6 eV while that of the "3+" peaks is 5.8 eV. But even so, the "2+" ion continues to be more predominant. The ratio between peaks (2+) is 0.7, which means that the film has completely covered the substrate, i.e. growth layer by layer. The ratio between the peaks (3+) is 0.47. For 6 nm, in addition to the ion "2+" and "3+" we have another contribution located approximately at 94 eV, and this satellite is due to the charge transfer between film-substrate. The ratio of (2+) compared to the previous film has fallen to 0.6 eV, probably due to the thickness of the film. Several post-annealings were necessary to improve the LEED patterns, which must have caused patches like a layer + islands growth. The ratio between "3+" is 0.51, while the ratio of 3+ keeps constant. For this film we see that the (3+) ion is more dominant. For the thickest film - 7 nm, the intensity of the (3+) ion is higher than the (2+). The ratio between peaks (2+) has decreased more to 0.53, we consider that the same factor (post-annealings) has influenced this result.

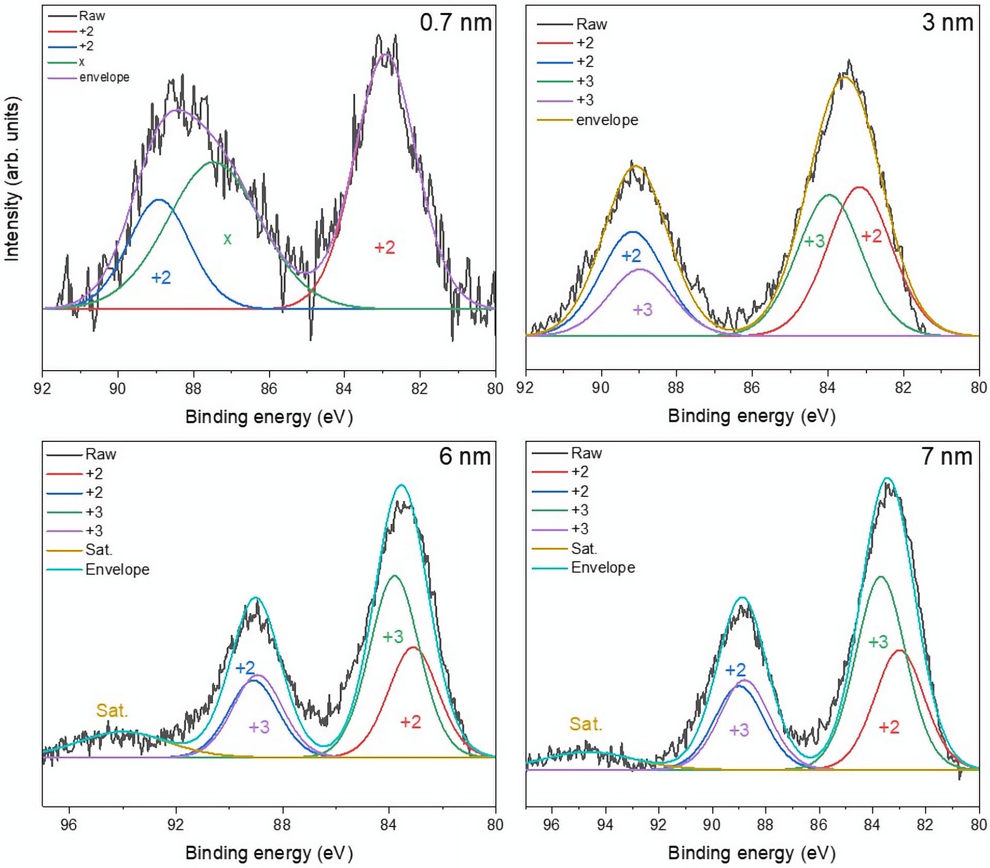

Figure 5.2: HR XPS spectra of several Mn$_3$O$_4$ films deposited and annealed at 5×10^{-7} mbar. (a) Mn $2p$ and (b) Mn $3s$.

Among all films and their thickness, different structures were observed by LEED patterns, see Figure 5.3. The quality of the patterns, i.e. the definition of the spots, were improved by performing several post-annealing at the same oxygen pressure, 5×10−7 mbar. But in all cases we avoid raising the temperature too much to avoid the complete desorption of the film. With LEED results, we verify if for all the films we have the same surface structure or if there is more than one phase.

The top panel of Figure 5.3 displays LEED pattern are shown at 50 eV (a) and 80 eV (b) for Mn$_3$O$_4$ thin film (1.4 nm), the same structure was found for 0.7 nm film. In the first inner circle, we observe 6 strong spots, the second inner has 12 line spots and the outer circle has 6 line spots (several and elongated spots together that looks like only one). The lattice parameter of this Mn_3O_4 film was estimated in a_1= 2.8 Å and a_2= 6.5 Å with angle of 64° between lattice vectors, once again confirming the formation of Mn_3O_4. These values are very close to the ones for Mn_3O_4 (110) plane (theory): a_1=3.14 Å and a_2=6.28 Å. Comparing experimental and bibliographic values, we see that there is a 10% variation, there is a distortion of Mn_3O_4 structure. Panel (c) shows the reciprocal lattice space with the six domains (color spot) simulated by the LEEDpat program [108] with our lattice parameters. Since the sample is thin we can still see the characteristic spots of Cu at 85 eV. The yellow circles represent the hexagonal pattern for the copper substrate, not copper oxide as we see the LEED pattern in chapter 3. Red, green and blue circles represent the 3 spots circles. As a result we obtain a distorted Mn_3O_4 (110).

The bottom panel of Figure 5.3 shows the measurements for Mn_3O_4 thick film (7 nm). The LEED pattern at 20 eV (d) and 75 eV (e) show a different structure than thin film, we also see that the quality of the patterns is not good. Although it took six post-annealing to be able to observe the spots marked (red and blue) in the figure. Cu spots are not more visible due to the large thickness of the film, but we marked the substrate spots as reference. At 20 eV (d), the figure show two inner hexagon patterns and one outer hexagon are notice at 75 eV (e) (red circle). The lattice parameter obtained from the LEED pattern were: a_1= 5.3 Å and a_2= 11.0 Å with angle of 72° between lattice vectors and with 6 domains. The simulation was represented in panel (f) and confirms the the growth of a distorted superstructure (2x2), almost twice the value we found for the previous film - Mn_3O_4 (110). Besides the number of annealing used for thick samples, the other parameters were not modified, which leads us to believe that the phase change is due to the influence of the substrate.

In thick films, the Jahn-Teller distortion favors the "3+" state which causes an octahedral distortion which generates a decrease in the oxidation state, hence the mixed valence of Mn_3O_4 [48]. There are several theoretical works trying to explain the distortion in other oxides with mixed valence such as [116, 117]. We have already seen in the Mn3s analysis that the 3+ ion predominates. The valence band is composed mostly of O 2p and Mn 3d, especially of the octahedral sites. We assume that the transfer of electrons occurs between the O $2p$ state and $3d^4$.

The Figure 5.4 shows the valence band spectra of clean Cu(111) surface and Mn_3O_4 for two films with different thickness, 0.7 and 7 nm. The measurement were performed using He I_α lamp and at room temperature. The clean Cu(111) (green) has the following features at 2.3, 2.9 and 3.5 (black dotted line) eV characteristics of the copper valence band spectra. It is possible to differentiate the contributions for Cu, Mn and O by comparing all the spectra. The thinner film of Mn_3O_4 have a larger contribution from copper VB yet visible. But even so it is possible to see a

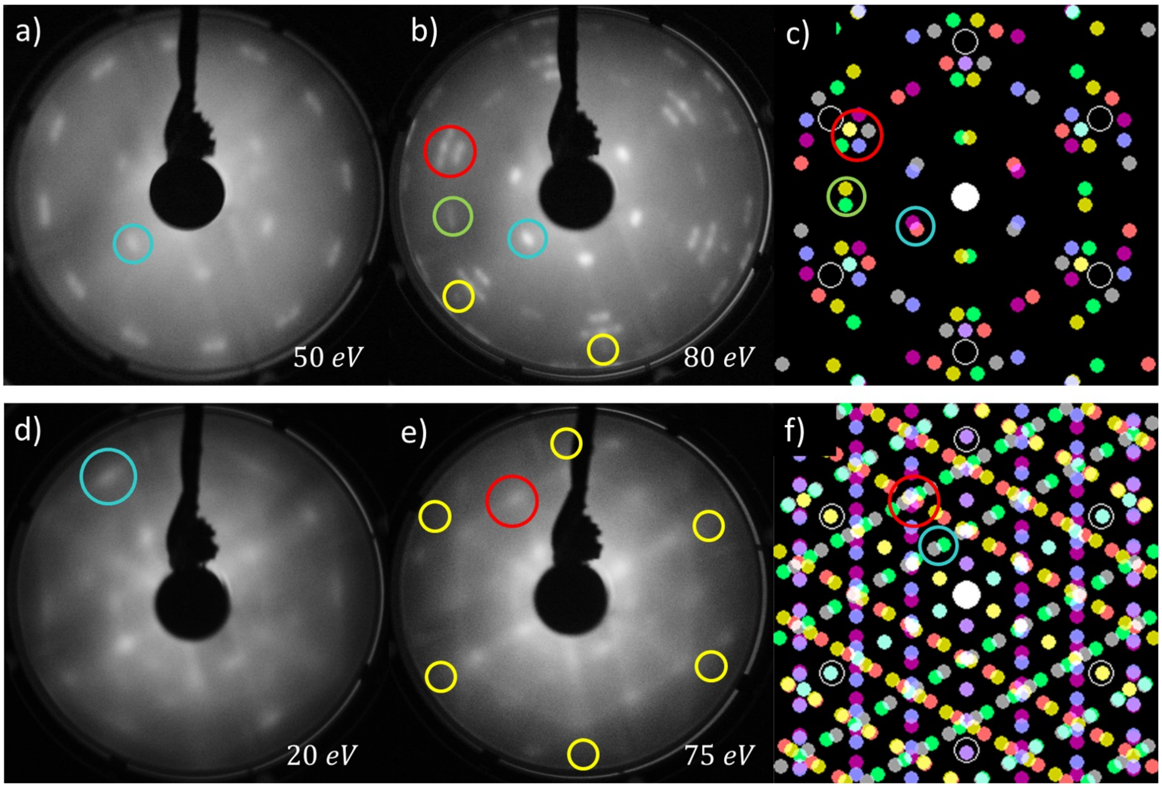

FIGURE 5.3. LEED patterns of two Mn_3O_4 thin films at energies of 20 (e), 50 (a), 75 (f) and 80 eV (b). (c,g) The figures represent the simulation for Mn_3O_4 for thin (top) and thick (bottom) film, respectively. The last panels (d,h) show the lattice plane visualized in real space.

shoulder at 1.8 eV that does not belong to the substrate but to the Mn 3d state of the film.

Despite not being so noticeable, we see an enhancement at 3.5 eV as well as the appearance of a shoulder at 5.4 eV (5 to 7 eV), which is associated with O 2*p* states seen in the thicker film too. The increase to 3.5 eV indicates the dominance of the Mn 3d states over O 2*p*. For the thickest film (7 nm), the contribution of substrate is not more relevant for this film, due to its thickness. We see that there is a shift of 0.3 eV to higher binding energy (BE), according to Kundu [4] this is due to the annealing at high temperatures that the sample suffers. This increase in temperature generates defects or oxygen vacancies which is reflected in the shift that is also seen in the O 1*s* spectra.

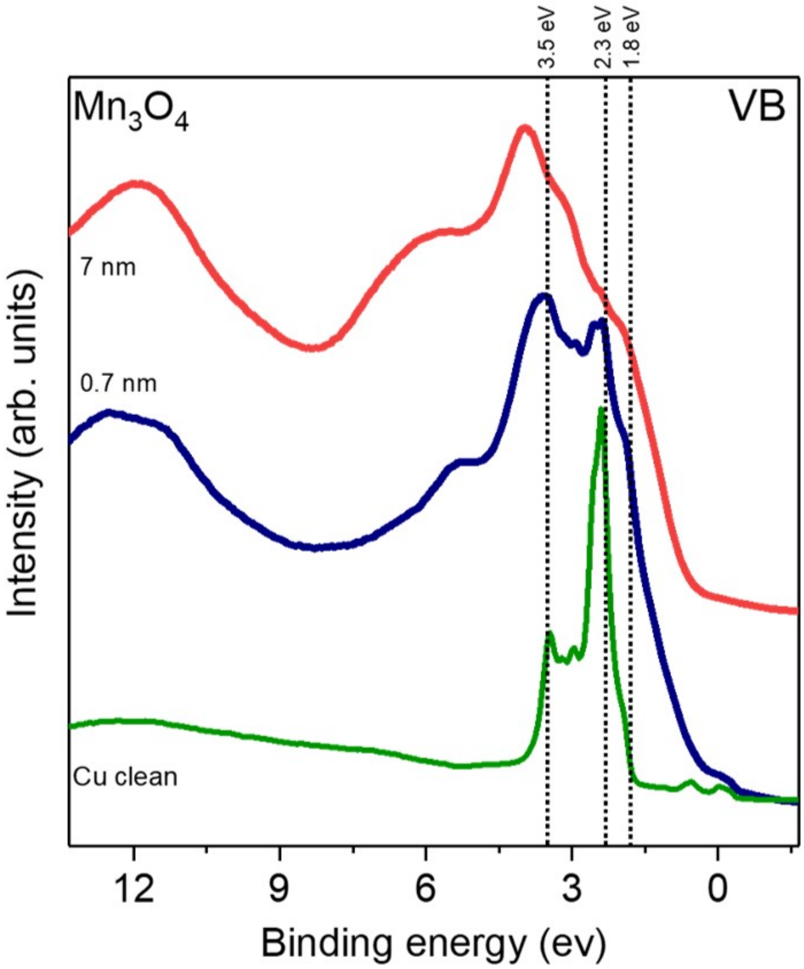

FIGURE 5.4. UPS spectra for Cu clean and two Mn_3O_4 thin films: 0.7 and 7 nm.

Partial conclusions

By increasing the oxygen pressure to $5x10^{-7}$ mbar we obtained a different manganese oxide: Mn_3O_4. We confirm the oxidation state with Mn 2*p* and Mn 3*s* core levels. The distance between Mn 2*p* is 11.7 eV and the absence of the satellite at 6 eV, indicate the discarding of MnO. Also, the line shape changes from flattened (0.7 - 1.4 nm) to sharp (3 - 7 nm). This modification is attributed to the effective interaction of thin film with the substrate (Cu or CuOx). The Mn 3*s* exchange energy split separation is 5.6 eV. This result is compatible with Mn_3O_4 than other manganese oxide. From 0.7 to 7 nm, the contribution of the 3+ state increases over the 2+ state.

Through LEED patterns, we saw that for thin films we obtained the phase (110) with lattice parameters: a1= 2.8 Å and a2= 6.5 Å. For thick films, we obtained a (2x2) reconstruction of the phase (110) with a1= 5.3 Å and a2= 11.0 Å.

In VB is possible to see a shoulder at 1.8 eV that does not belong to the substrate but to the Mn 3*d* state of the film. A menor enhancement is observed at 3.5 eV as well as the appearance of a shoulder at 5.4 eV (5 to 7 eV), which is associated with O 2*p* states seen in the thicker film too. The increase to 3.5 eV indicates the dominance of the Mn 3d states over O 2*p*.

CHAPTER 6

VALENCE BAND STUDY OF MN_3O_4 BY RESONANCE PHOTOEMISSION (RESPES)

Two Mn_3O_4 films were deposited on Cu(111) at PGM beamline in LNLS synchrotron in Campinas, Brazil. We try to maintain the same growing conditions as in the CBPF. At LNLS, we use the beamline as a variable energy source to the range from 100 to 1500 eV as described in the reference [110]. So, to confirm the formation of Mn_3O_4 films see the Figure 6.1. Here, we measure the Mn 2*p* core level with a different energy from previous chapters where we use an Al source. For this case, the energy used was 851.4 eV and the biggest change is the absence of the Mn LMM auger at 660 eV. Due to this change, it is now easy to observe the satellite located at 10.5 eV so characteristic of Mn_3O_4 and not Mn_2O_3 or MnO (remenber too the absence of satellite next to main peak - $2p_{3/2}$). So, both films, 1 and 3 nm, are confirmed as Mn_3O_4.

The surface structure of both films was found with LEED measurements. Initially, it was expected to find the same growth plane (110) as seen in chapter 6, since we tried to reproduce the same recipe with the same parameters or close values. The 1 nm film measured at 35 and 80 eV (top left panel), in Figure 6.2, has the expected structure of 110 (one inner circle with 6 spots and two outer circles with line spots). As we have already seen and analyzed the diffraction patterns in detail in the chapter "Growth of Mn_3O_4 on Cu (111) films". On the contrary, the 3 nm film presents a different structure not seen in previous results. For this new structure measured at 25 and 35 eV, we observe two circles (dashed red lines) with twelve spots each one, twice than 110 plane.

In the right panel we observe the structure of Mn_3O_4 for 1 and 3 nm films, both of them have almost the same distorted unit cell as indicated in Figure (top right panel) with turquoise lines.

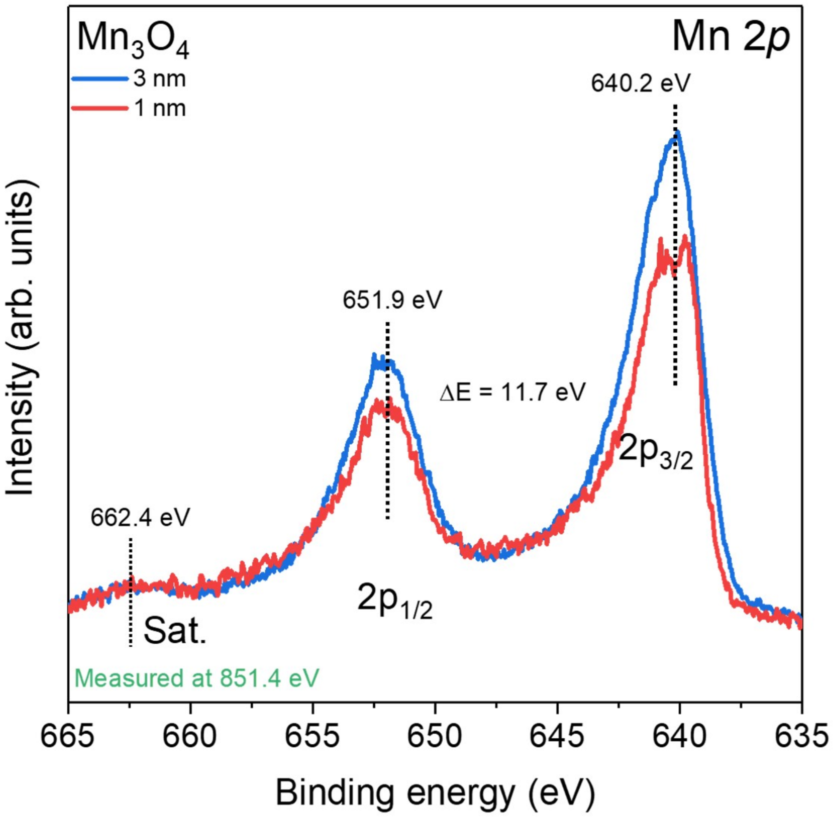

FIGURE 6.1. Mn 2*p* core level HR spectra for two Mn_3O_4 films: 1 and 3 nm.

The lattice parameters for 1 nm is the same for other Mn_3O_4 films found in previous chapters: a_1 = 2.8 Å and a_2 = 6.5 Å, with an angle of 64 between vectors. For 3 nm, we obtained the following lattice parameters a_1 = 3.2 Å and a_2 = 6.4 Å with an angle of 60 between the lattice vectors. Interestingly, the lattice parameters of both films seem to be similar, so we decided to verify the angle between the film + substrate for both cases. Unexpectedly we found that between both films there is a difference of 15° (α(3 nm) = α(1 nm) + 15°). In other words, the difference is due to the arrangement of the Mn_3O_4 atoms on copper substrate.

As we already mentioned, we tried to reproduce the same previous conditions, but then we noticed a slight difference in the amount of material deposited, which was higher than expected. And as we have seen before, in thick films the diffraction patterns have less definition. Therefore, initially no pattern could be observed, to improve the resolution we decided to increase not only the number of post-annealings (evaporate material) but also the maximum temperature used. We know from past experiences that increasing the number of post-annealings (all with the same parameters) does not generate changes in the structure, which leads us to believe that the change is mainly due to the increase in temperature.

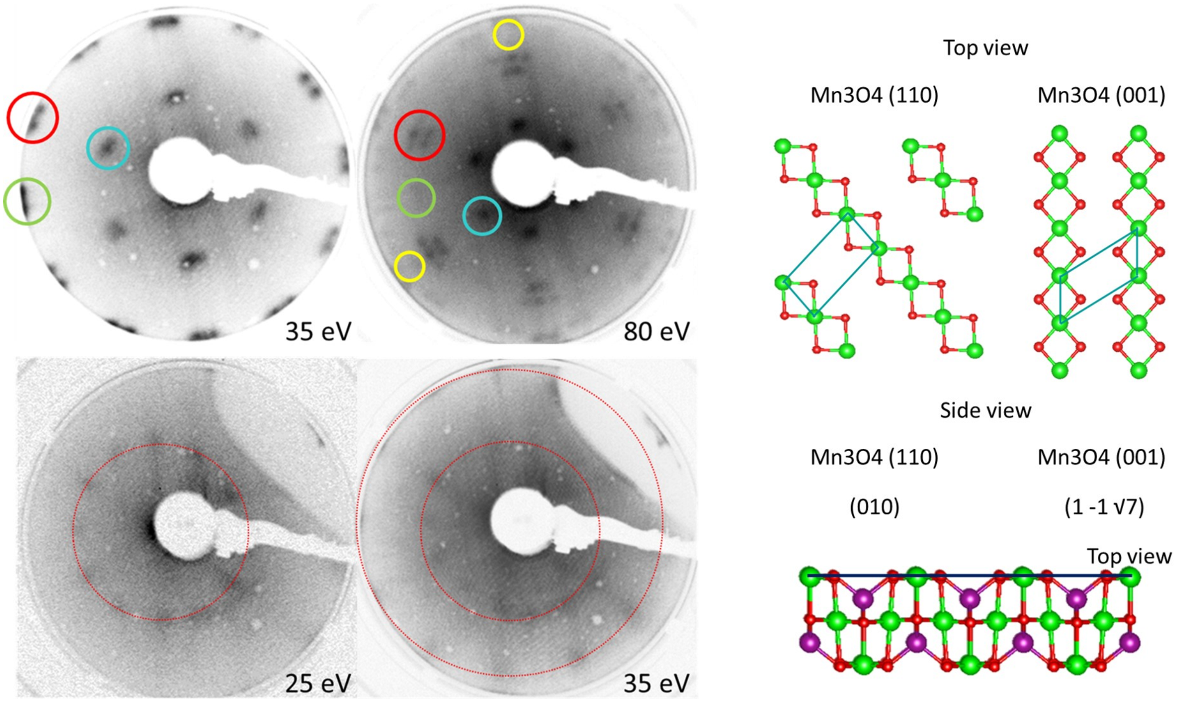

FIGURE 6.2. (Right) LEED patterns of Mn$_3$O$_4$ films measured at 25, 35 and 80 eV. (Top) 1 nm and (Bottom) 3 nm. (Left) Lattice structure for both films with distorted unit cell (turquoise line).

Before entering about the VB study. We first perform a quick measurement of this region for 1 and 3 nm using the same energy used for the Mn 2p core level (851.4 eV) and the minimum energy measured by the beamline (100 eV). In the figure we will show only the 3 nm film because the low thickness and the background do not allow us to see the film in detail, since the substrate predominates. We observed that in the thicker film, the contribution of the hybridized O 2*p*-Mn 3*d* state is more notorious (purple and blue spectra). Comparing both energies, we see that at 100 eV the film contribution is more intense than the substrate (see how the O 2*s* peak at 22 eV decreases by increasing the intensity at 3.5-3.6 eV region). So at the end, the peak (3,5 eV) is related to the film and not Cu. Compared to other measurements made with stable sources such as Al and Mn, we see that we have a better resolution using variable energy as the source. Therefore we set up the ResPES experiment with variable excitation energies coming from the threshold of Mn and O. These energies were obtained from the XAS spectrum.

XAS results for 1 and 3 nm films measured at normal incidence "NI" or "grazing" to the sample were performed at room temperature. The comparison between the XAS spectra with different thicknesses can be seen in the previous chapter 4. Since we already mentioned that in the thinnest film it is not so easy to observe due to the influence of the substrate, we chose to

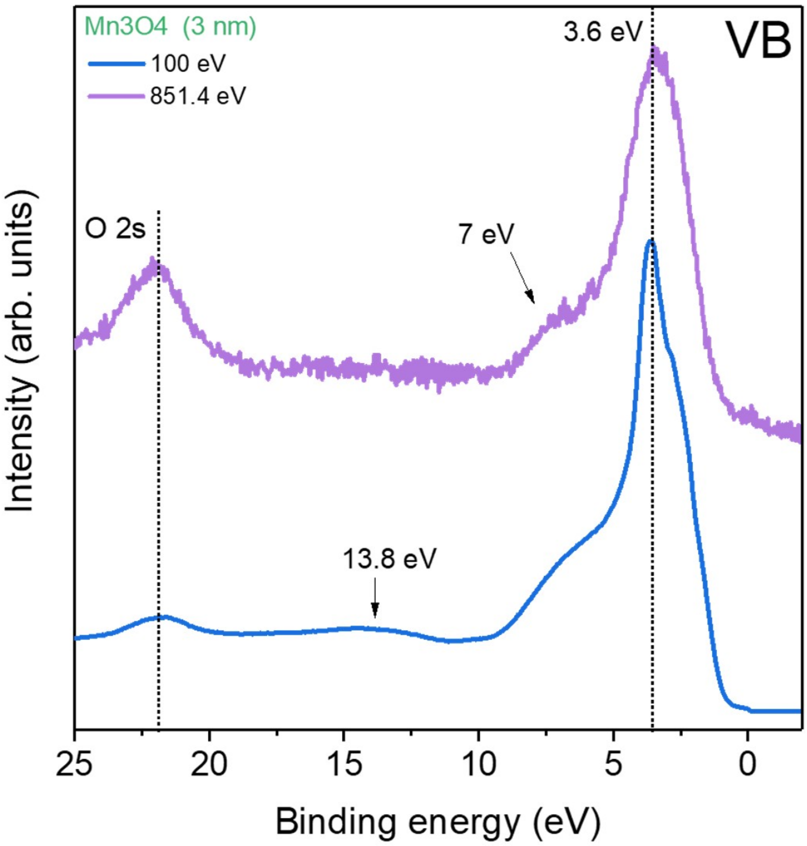

FIGURE 6.3. Valence band for the thick film (3 nm) measured at two different energies 100 and 851.4 eV at LNLS.

show the XAS results for Mn and O for the thickest film. The left panel shows the Mn L_3 edge of Mn_3O_4 films for transitions between Mn $2p$ and Mn $3d$. Each absorption peak represents a characteristic energy that is marked with dotted lines: 639.7, 640.5 641 and 641.8 eV, the peak of 641 eV with the maximum intensity. The first peak (639.7 eV) is attributed to the oxidation state "2+", while the other peaks correspond to the superposition between the "2+" and "3+" states. The right panel shows the O K-edge with transitions between O $1s$ and $2p$. Like the previous panel, we mark energies with dotted lines as 530, 531, 533.1 and 540.5 eV. The pre-edge feature is related to oxygens outside and inside the plane and which are linked with the hybridized state. We noticed the difference of the intensities between the peak at 530 (e_g) and 531 eV (t_{2g}), the latter with higher intensity, almost absorbing the peak at 530 eV. The peak at 540.5 eV has a short shift due to the unoccupied states of the O $2p$ linked to the 4 sp band). The background was removed for all spectra.

We observed the resonance enhancement of Mn3d states for absorption energies: between (Figure 6.4) 629-663 eV for Mn 2p and (Figure 6.5) 520-568.3 eV for O 1s.The ResPES experiment was carried out after the XAS results, since we took as reference the energies that correspond

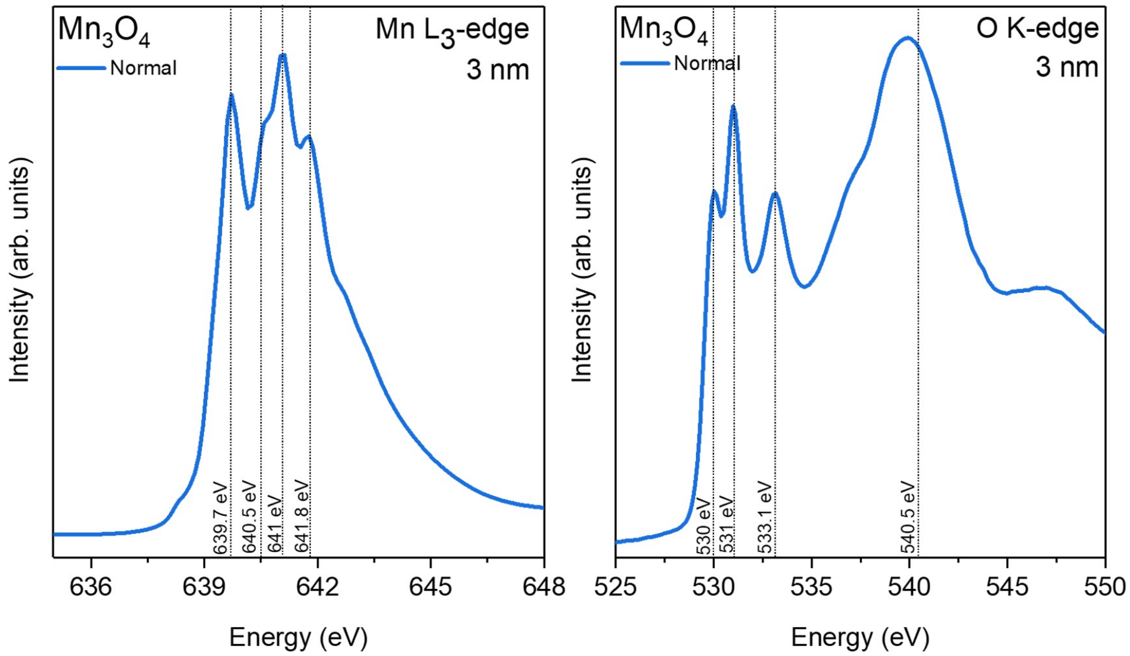

FIGURE 6.4. XAS spectra of Mn$_3$O$_4$ mesured at (Left) Mn L2-edge and (Right) O K-edge for thick film: 3 nm

to the position of absorption peaks across the XAS threshold. The maximum intensity peak as 641.8 eV (dotted lines in Figure 6.4), as well as energies with the minimum intensity as 630 eV. Our objective is to understand the increase in intensity as a function of the energy used. The ResPE spectra is displayed in Figure 6.5 and were measured in an energy range from 630 to 670 eV. All the spectra were calibrated using Cu 3p (fix position at 75 eV) peak and the background was removed using a linear fitting. The spectra were divided in two regions: the first one from -1 to 28 eV, a normalization to the maximum point in this region has helped to better distinguish the contributions located at 7.5 (actually is displayed from 5 to 8 eV) and 22 eV. Later labeled as pure film contribuions as O 2p-Mn 3d and O 2s, respectively. The maximum intensity used for normalization was 3.5 eV (although the enhancement is not seen because of the normalization). This value in conjunction with the shoulder at 1.8 eV is already known from our previous works, where we saw that these contributions belongs only to the t$_{2g}$ and e$_g$ states of Mn. The auger labeled as Mn L$_3$VV (blue dotted line) is seen across the entire region (dispersed) as a function of binding energy. The second region from 28 to 85 eV, no normalization has been applied for this case. Another auger is found and labeled as Mn L$_3$M$_{23}$V [112]. And followed by film contributions, Mn 3p and Mn 3s. Even knowing that film is thick, we can see that features of the substrate are still present, its contribution in valence band at 2.3 eV as well as the presence of the Cu 3p core level at 75 eV.

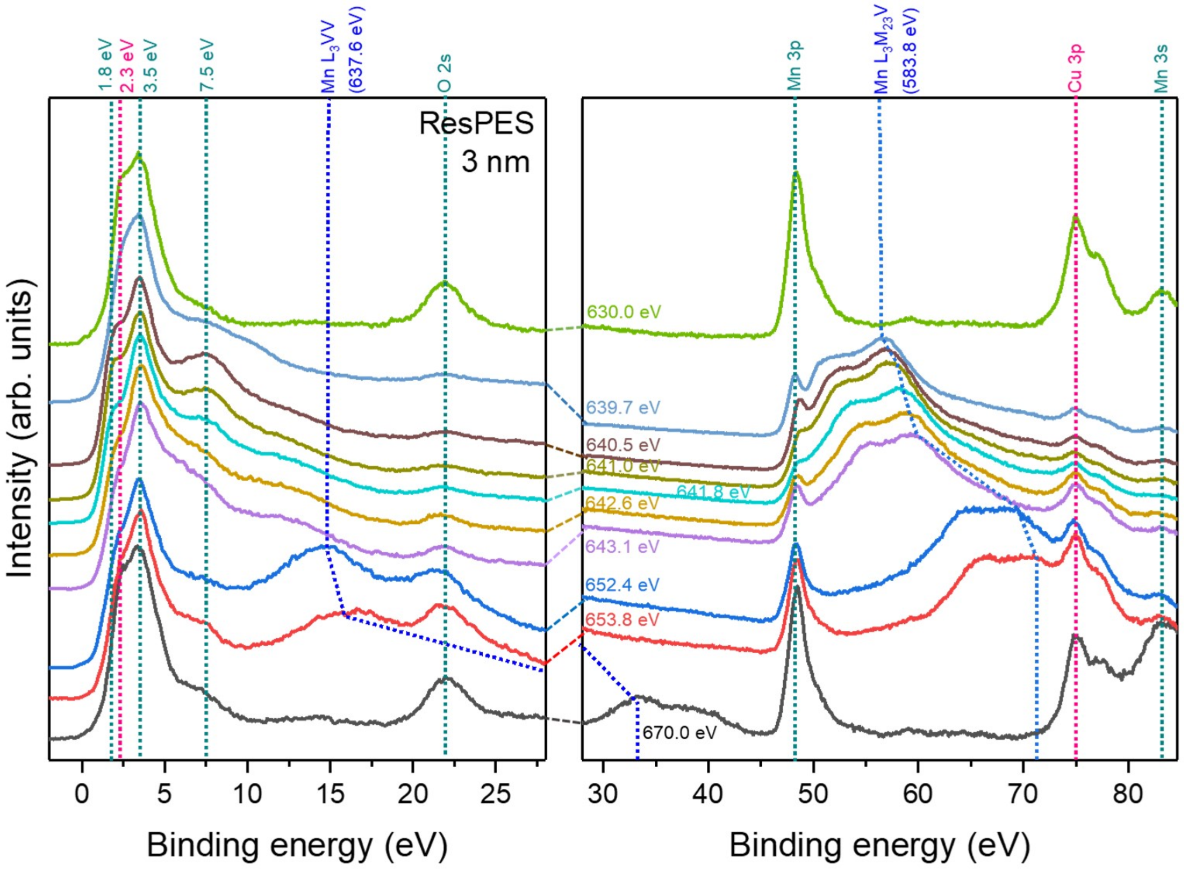

FIGURE 6.5. ResPE spectra normalized and calibrated for Mn_3O_4 films at selected energies (different colors) using the Mn L2-edge threshold. The spectra were separated in two regions.

The results of the resonance photoemission measured with the energies of the threshold of O are elaborated in the following figure. The same analysis of dividing into two regions has been applied. But this time, in the first region from -1 to 9 eV no normalization at 3.5 eV has been carried out since only the contribution of hybridized states (close to 7.2 eV) is hardly visible. Another reason why the spectra were not normalized at 3.5 eV is because of their intensity. Unlike Mn, for oxygen spectra the intensity enhancement between 520.0 to 554.3 eV is not large. Eventually we see that there is a small enhancement at 3.5 eV, although it is difficult to recognize the hybridized state O $2p$ - Mn $3d$ in figure due to the prominent Augers contributions, but with 554.3 and 547.6 eV spectra we could distinguish that is located at 7.2 eV. We observe a shoulder at 2.3 eV, but apparently there is no change as a function of energy, which leads us to think that this shoulder is related to the substrate and not the film.

In second region, we applied a normalization at 85 eV to keep all the spectra with the same background. Unlike Mn, in this region we see more auger contributions, and we labeled as follows: O KVV (KE = 512.3 eV), O KL$_1$L$_{23}$ (KE = 492 eV) and O KL$_1$L$_1$ (KE = 477 eV), where KE is Kinetic energy. [112]. Substrate features are less visible, such as Mn 3p and O 2s. Almost Cu 3p were used to calibrate the spectra.

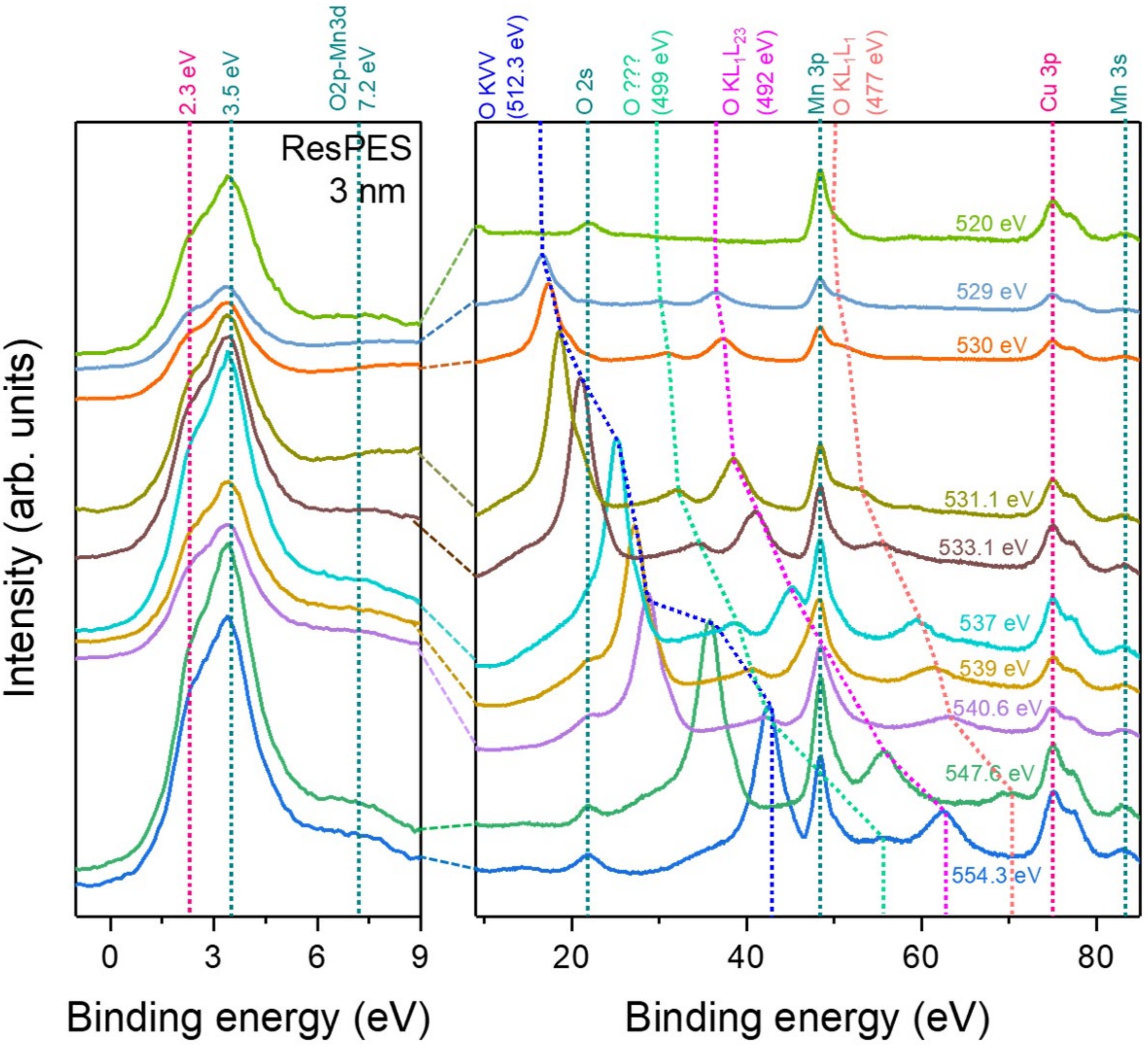

FIGURE 6.6. ResPE spectra normalized and calibrated for Mn$_3$O$_4$ film at selected energies (different colors) using the O K-edge threshold. The spectra were separated in two regions.

We already know that the selected energy (see energies associated to different colors) correspond to the position of absorption peaks across the XAS threshold. We already saw in the resonance measurements (of Mn) of Mn$_3$O$_4$ that due to normalization we could not observe the difference in intensity between spectra. Therefore, in the following figure 6.7, we show the same region but without normalization. Now, the enhancement at 3.5 eV is noticeable from 639.7 to

643.1 eV ("on-resonance” spectra), with two energies with higher intensity: 639.7 and 641 eV. Precisely, these two energies belong to the maximum peaks seen in the XAS spectrum, 6.4. Other energies like 630 eV or 652.45 to 670 eV not show large or any changes in intensity, we refer these to “off-resonance” spectra. Then, contrary to manganese region, with O 1s energies we not observe an enhancement at 3.5 eV. So, we confirmed that the increasement is related to Mn states.

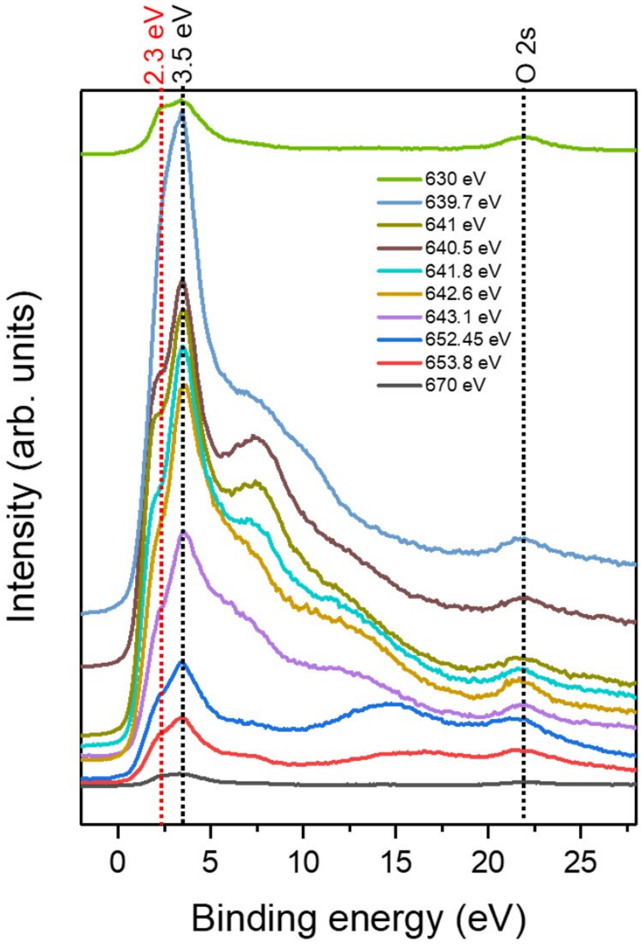

FIGURE 6.7. No-normalized ResPE spectra of Mn$_3$O$_4$ film. The O 2*s* peak was used as calibration peak. The contribution at 3.5 eV is more intense at 639.7 eV (on-resonance).

So, we select three “on-resonance” spectra to study the contributions of the film as seen in panel a, b and c. First, we already measure the resonance of the Cu (111) substrate by using the same Mn (Figure 4.7) and O (4.8) energies. Since the enhancement is related to the Mn states, this analysis will be done only for the Mn threshold and not for oxygen. We select energies where the resonance was higher like 641.8 (a), 641 (b) and 640.5 (c) eV. For these spectra, we remember that we also see contribution from the substrate and not only the film. So, in panels we obtain the difference between the film (indeed is "Mn$_3$O$_4$+ Cu" - red spectrum) and substrate ("Cu" - blue spectrum), obtaining only the pure contribution of the film. Before subtraction, all spectra were calibrated and the background was removed. Thus, the green spectra represent the only pure film contribution i.e. the difference. As for MnO, we the existence of two Mn states at 1.8 and 3.5 eV which were labeled to e_g and t_{2g} orbitals of Mn, respectively. From 4.5 to 9 eV, we observed the O 2p - Mn 3d states.

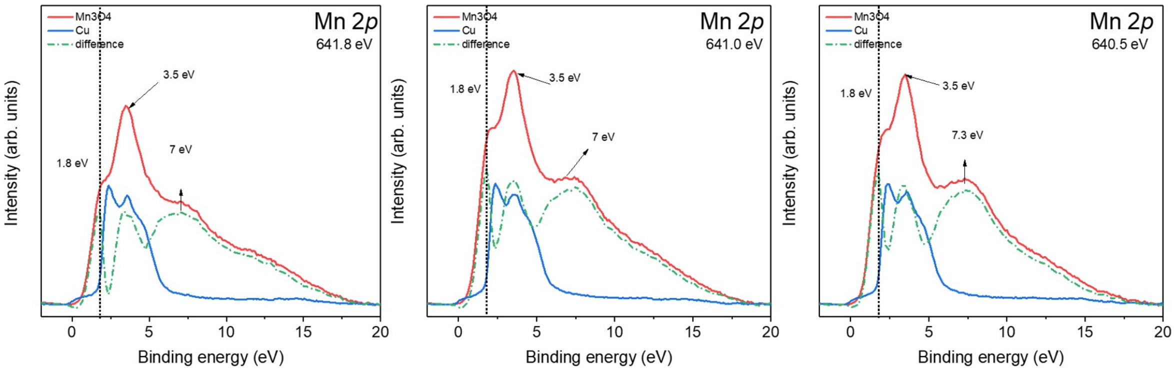

FIGURE 6.8. (ResPE spectra normalized and calibrated of Mn$_3$O$_4$ and Cu at three selected energies (all on-resonance): (left) 641.8 eV, (center) 641.0 eV and (right) 640.5 eV. The dotted spectra is the difference between film and substrate.

Partial conclusions

We obtained two Mn$_3$O$_4$ films (confirmed by XPS) with thicknesses of 1 and 3 nm. The LEED results showed the formation of two distinct phases: (110) for 1nm and (001) for 3nm. Both films have a distorted unit cell due to the Jahn-Teller effect. Their lattice parameters are: a_1 = 2.8 Å and a_2 = 6.5 Å for thin film. For thick film, we obtained the following lattice parameters a_1 = 3.2 Å and a_2 = 6.4 Å. The phase change of the film is probably due to the increase in temperature of the post-annealing.

Due to the interference of the background and the small amount of material from the 1nm film, a study of the VB and XAS could not be carried out. Only for the thickest film. XAS for 3 nm film, we see that at the Mn L3 edge: the first peak at 639.7 eV is associated with the 2+ state and the following peaks with the superposition of 2+ and 3+. For O K-edge: The pre-edge function is related to the in-plane and out-of-plane oxygens associated with the hybridized state.

ResPEs spectra shows the auger and film+substrate contributions for several energies (Mn threshold). We found a shoulder at 7.5 eV labeled to O2p-Mn3d and peaks at 3.5 and 1.8 eV, not labeled yet. This is only visible in Mn and not for O resonance. A difference between the film and the substrate indicated the existence of 3 features: 2 peaks and 1 shoulder. Already seen in previous results. The two peaks at 3.5 and 1.8 eV represent the t2g and eg state. The shoulder at 7 eV is labeled as a hybridized state.

CHAPTER 7

STUDY OF THE ELECTRONIC PROPERTIES OF Mn_3O_4 DOPED WITH COBALT

We have already seen that Mn_xO_y is a widely used material in different applications. For example, in the battery industry it is used to improve storage capacity. We know that manganese oxide is a highly promising catalysts and it is one of the most used due to its durability and low cost [118]. But one way to improve the properties of a material is to be doped with another material. For example, using a metal (M) as a dopant in Mn_xO_y we can improve the chemical stability due to strong chemical bonds between the substituted cations (M replaces Mn) and oxygen.

It is also important to emphasize how the dopant fits within the crystal lattice. In the case that the dopant fails to enter in the lattice correctly, it is likely that a mixed oxide will be obtained instead of a doping. This happens when there is no control of the am ount of dopant inserted. So, to avoid the strong modification of the structural and the formation of mixed phases, a small amount of Co was added in Mn_3O_4 thin films. The reason for using cobalt is because it has the same oxidation state and because their chemical properties are similar.

Our first attempt was to obtain a doped film on the same substrate (Cu) that we have been working on previously. Although we have found some difficulties that we will detail later, the following table 7.1 summarizes the attempted deposition of the films:

So we deposited Mn_3O_4 at 5×10^{-7} mbar with different configurations and then a post-annealing was performed at the same oxygen pressure for 20 min for all samples.

For sample "1", we choose a reasonable deposition time like 20 min to avoid a thick or thin film. The initial deposition rate for cobalt was 60 times lower that manganese. The deposition was performed layer by layer to avoid material desorption. We started with Mn for 5 min, then

Sample	R(Mn)/R(Co)	Deposition time (min)	Comments
1	60	20	Mn: 18 min Mn+Co: 2 min
2	60	5	At the same time
3	20	5	At the same time
4	20	10	At the same time
5	10	5	At the same time

Table 7.1: Information about all the samples (film+dopant) deposited on Cu substrate.

Mn+Co for 0.5 min, again Mn for 5 min until complete 20 minutes. No LEED result was seen after second post-annealing. XPS results were not promising as shown in figure 7.1 because no trace of cobalt was found in the spectrum (black line).

We thought that the problem could be the amount of manganese deposited compared to cobalt. For sample "2", we kept the same rate and reduce the deposition by 4 times (5 minutes). Both materials were deposited at the same time. XPS spectrum (not shown here) not show the existence of cobalt.

For sample "3", the initial rate (60) was reduced by 3 times (20) and the deposition time was the same (5 minutes) that sample "2". No XPS and No LEED was obtained.

Since the problem was the absence of cobalt in the spectrum. For sample "4", we deposited at the same time Co and Mn$_3$O$_4$ for 10 minutes. We know that if the amount of the dopant is high, there is a probability that a mixed oxide will be formed. But our goal is to obtain a defined Co 2*p* spectrum. Two small peaks can be seen in green spectrum, see figure 7.1.

With this promising result we reduce the last rate and deposition time used by half for sample "5", see table 7.1. The HR spectrum clearly shows the two cobalt peaks separated by a distance of 15.4 eV as well as two prominent satellites. The quality of the spectrum is not the best but it is still a satisfactory result. The "strong" presence of these satellites at ~ 6 eV could indicate the formation of CoO (2+).

We discovered with the presence of Co 2*p* some problems to identify the formation of the Mn$_3$O$_4$ film. Throughout this work we have always used the Mg source to avoid the overlapping that occurs between Mn 2*p* and the Cu LMM auger by using Al source. For this system (film+dopant) using the Mg source, we observe an overlap between Co LMM auger with Mn 2*p*. It is impossible to verify the formation or oxidation state of Mn$_3$O$_4$ with this overlapping. So, using the Al source is not a solution.

To avoid these problems, we changed from Cu (111) to Au (111) substrate.

The last sample on Cu was successful in showing the presence of cobalt but no LEED was found. For sample "6", the first in Au substrate, we use layer by layer deposition and we mantain the same rate. The layers were distributed as follows: Mn$_3$O$_4$ for 10 minutes - Co for 5 minutes - Mn for 1 minutes - Mn$_3$O$_4$ for 10 minutes, with 26 minutes of total deposition. Followed by an

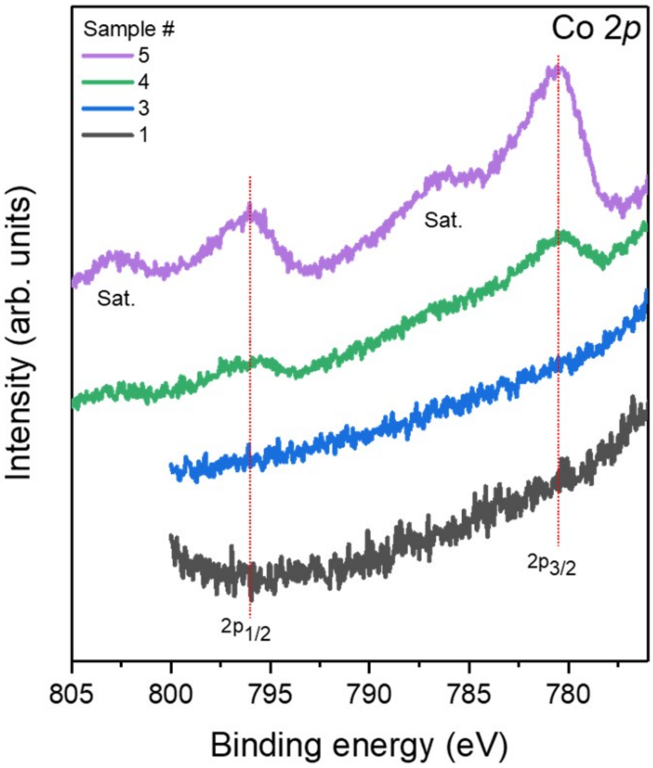

FIGURE 7.1. HR-XPS spectra of Co 2p for several films. Our main goal was to demonstrate the presence of cobalt in the manganese oxide lattice.

annealing of 20 minutes.

The XPS spectrum was measured before and after annealing and we found that the intensity of the Co 2p peaks had decreased quite a bit. This indicated to us that cobalt was being desorbed from the film. Despite this, the spectral line can still be observed defined, as seen in figure 7.2 and it becomes evident that we are still facing the formation of cobalt oxide. After several attempts we were finally able to observe a diffraction pattern although it is a bit diffuse. At an energy of 125 eV, the two rings with 12 spots each can be seen. This LEED pattern has been previously seen in another work of our group dedicated to the growth of Mn_3O_4 on Au. More annealings were performed to improve the quality of the patterns but it had no effect, on the contrary with each annealing we lost more cobalt.

To tackle some of the difficult on the doping strategies explored above, we have employed a new approach, encapsulating the cobalt species between MnOx layers. In its metallic form (cobalt) it is more difficult to be removed with increasing temperature. The final recipe consists of a total 15 minute deposition, Mn_3O_4 (5×10^{-7} mbar) for 5 min + Mn without oxygen for 1 min + Co for 2.5 min + Mn for 1.5 min + Mn_3O_4 for another 5 min, see figure 7.3.

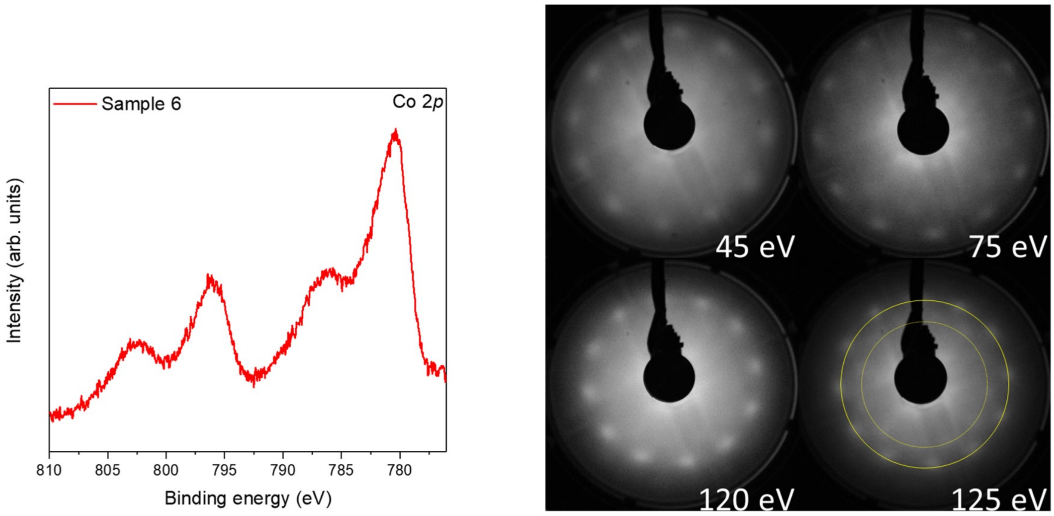

FIGURE 7.2. HR-XPS of Co 2*p* for sample "6", the core-level remains defined and shows the formation of CoO. LEED patterns of Mn$_3$O$_4$ "doped" with cobalt measured at energies of 45, 75, 120 and 125 eV

A subsequent post-annealing at the same p(O2) was used to create an ordered film. The recipe for sample "7" appears to be appropriate as cobalt desorption has decreased. Just as we see an incredible improvement in LEED measures. For this sample the rate set at 5 but considering that the difference between the deposition time of Mn with Co is 5 times lower. We can say that Co deposition rate was 25 times lower than the one for Mn.

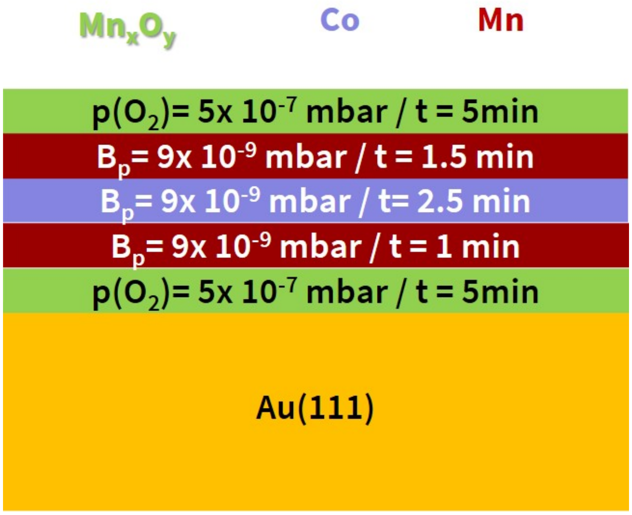

FIGURE 7.3. Scheme of layered deposition of cobalt-doped Mn3O4 to prevent cobalt desorption.

We remember that films with a thickness of 1 nm (about 10 minutes) were difficult to analyze with the XAS and ResPES techniques due to their low thickness. Therefore, a film thicker than 3 nm (30 minutes) was prepared with the previous recipe for XAS and ResPES measurements in LNLS. The core-level Mn 2*p* XPS spectra are showed in Figure 7.4 (left) for four films: two undoped (1.5 and 3 nm) and two doped (1.5 and 3 nm) films. Mn 2*p* binding energy position and the shape of the peak does not seem to vary depending on the doping. (Right) At first glance the line shape of the spectrum looks like CoO (2+) for the satellites but when the peak deconvolution is applied we notice that there are two contributions with 2-2.5 of FWHM. Although it seems that the contribution of the 3+ state is more intense, in fact the 2+ contribution has a larger area and therefore is more predominant. Since there are two oxidation states, it means that cobalt has grown in the form of Co_3O_4.

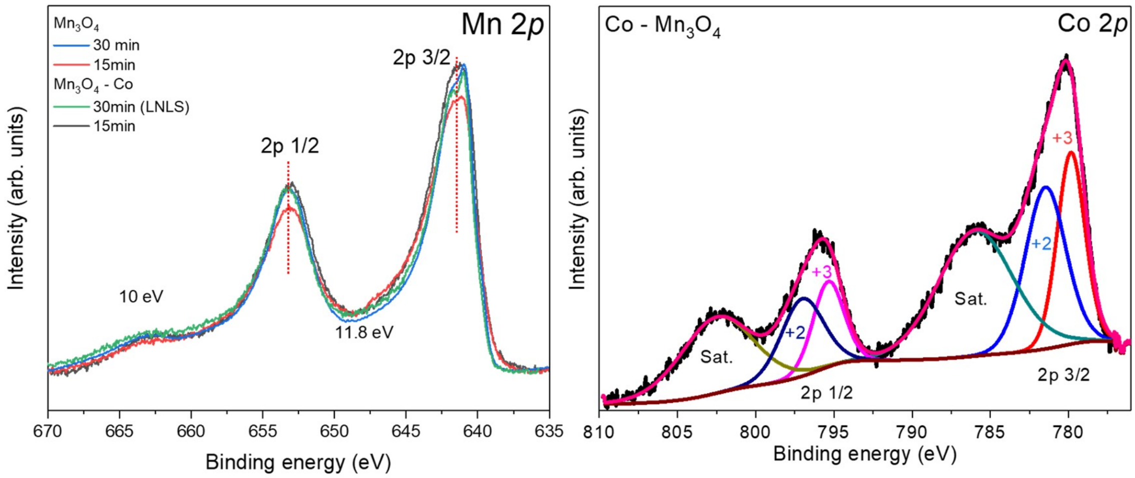

FIGURE 7.4. Survey XPS spectra of Au and Co-Mn_3O_4 measured at 1486.6 ev (a). High resolution of Co 2*p* (b) and Mn 2*p* (c) core level spectra.

LEED pattern at 45 eV for undoped (left) and doped (right) Co-Mn_3O_4 deposited on Au are seen in Figure 7.5. For the same energy, similar structural features are found, the two perfect rings (yellow dotted circles) with 12 spots each one are marked in both panels. This result indicates that the doped film is well organized on the surface as well as the undoped film. On the contrary, if the film had not been formed, no LEED sign would be seen. If the dopant had not entered well in the crystal lattice, we would have a polycrystal material with perfect rings (LEED). With the lattice parameters, the preferential growth plane was determined as Mn_3O_4 (001).

Doping can modify the lattice constants because it depends on the size of doping element (Co) and the material (Mn_3O_4). If the lattice parameter has decreased, it means that the ionic radius of cobalt is less than that of manganese oxide. According to the XPS results cobalt is in the Co_3O_4 state with the 2+ state with high spin and the 3+ state with high spin. So when entering the manganese oxide lattice Co(2+) should enter the position of Mn(2+) and Co(3+) in the position of Mn(3+).

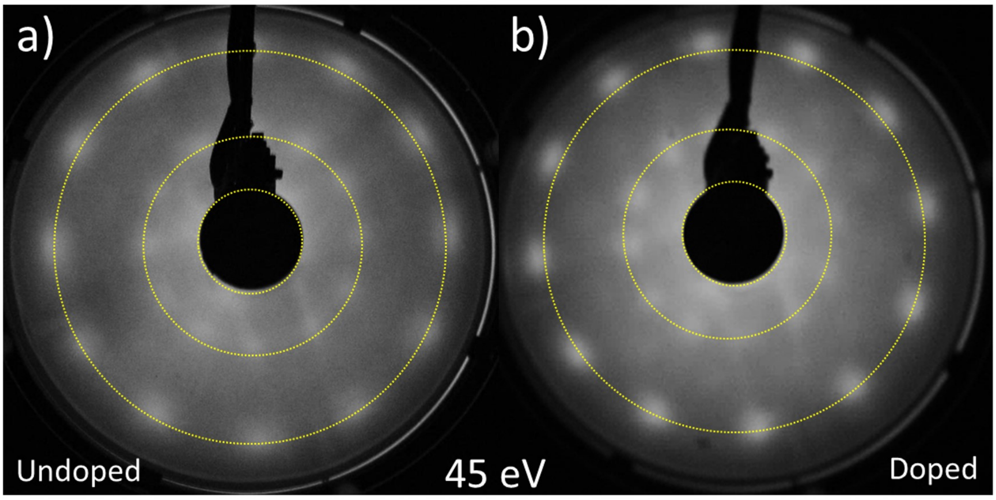

FIGURE 7.5. LEED patterns of Mn_3O_4 at energies of 45 eV for undoped [46] (a) and doped (b).

According to the following reference, the ionic radius for cobalt oxide and manganese oxide are the following [119]:

- Co (2+) with tetrahedral position and high spin is 0.720 A.
- Co (3+) with octahedral position and high spin is 0.750 A
- Mn (2+) with tetrahedral position and high spin is 0.800 A.
- Mn (3+) with octahedral position and high spin is 0.785 A.

An analysis of the XPS spectrum of oxygen shows that in addition to the peak related to the oxide there is another less intense peak. This peak represents the oxygen vacancies in the material lattice. We see that for an undoped 1nm film (15min) the number of vacancies is approximately 5.6%. In the case of a 1 and 3 nm doped film, the number of vacancies doubles to 10%. Noticeable differences are seen in the valence band, especially near the Fermi level. According to the results of Mn_3O_4 on Cu, we know that the start of the BV is about 1 eV because of the "t2g" state of the film. Now we see that below 1 eV, the 3d state of cobalt and Au are noticeable. So resonance measurements should help to get into details about the enhancement in that region. Both spectra have been normalized, so it seems that the spectrum of the undoped film has greater intensity, especially in the O 2p region (22 eV).

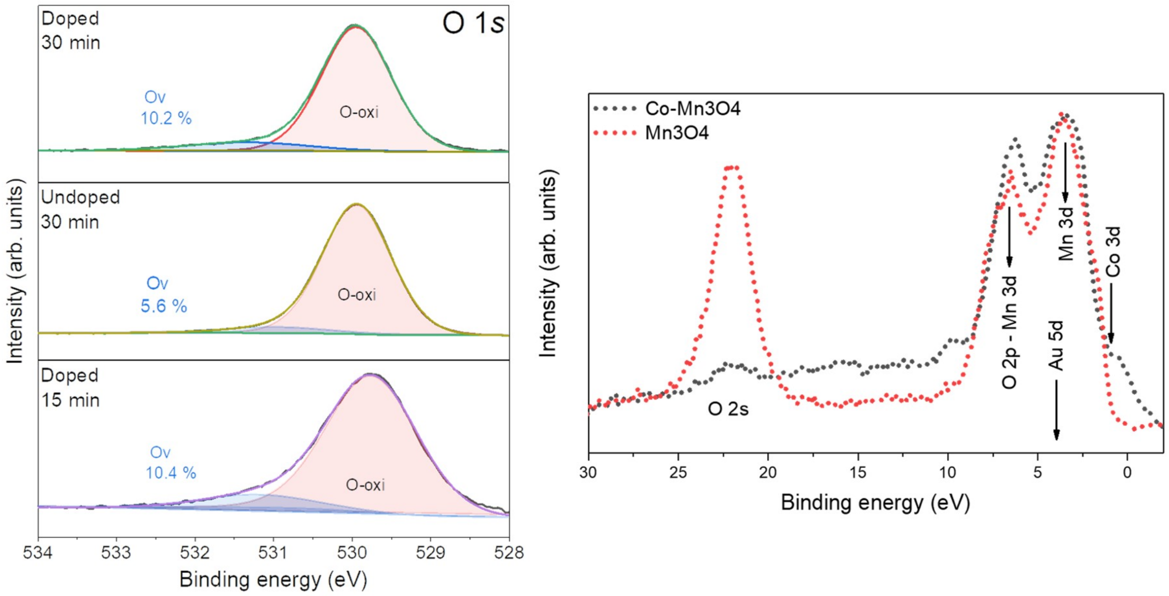

FIGURE 7.6. (Left) O 1s spectra for doped and undoped Mn$_3$O$_4$. The first peak is the bond between M and O. In a doped film the percentage of oxygen vacancies (second peak) increases almost double. (Right) Valence band region measured with Al source for both films.

The XAS and ResPE results shown below are from the 3nm thickest sample and and were measured on the PGM beamline. The left panel of Figure 7.7 shows the XAS spectrum for the Co 2p threshold. A comparison with the literature shows that the line shape of our XAS spectrum is more similar to CoO than to other oxides or even its metal form. As in the XPS spectrum it seems that the dominant state is the 2+ ion. The following reference [120] shows a comparative figure between different XAS spectra of Co. Even so, there are some differences such as the absence of the peak at 776 eV characteristic of CoO.

Wi et. al. [120] measured the XAS spectrum of Co for a cobalt-doped ZnO sample. It is known that the shape and position of the XAS spectrum depend on the electronic structure (crystal field) of the studied material. ZnO has a tetrahedral crystal field for that reason cobalt assumes the 2+ state but in tetrahedral sites when it enters as a dopant.

Since the line shape of the spectrum is the same as our result. We can assume that cobalt within manganese oxide is also located in the tetrahedral sites. We know that the 2+ ion is located in the octahedral site for CoO. While for Co$_3$O$_4$ the 2+ ion is in tetrahedral sites. This result corroborates what was stated previously, which is the formation of Co$_3$O$_4$.

For O K-edge XAS spectra we notice two differences. The first is the increase in the peak at 530 eV that almost absorbs the second peak located at 531 eV. The second difference is the shift towards higher energies for the doped film. This shift is related to the increase in vacancies (almost 10%) that we had already seen in the spectrum of O 1*s*.

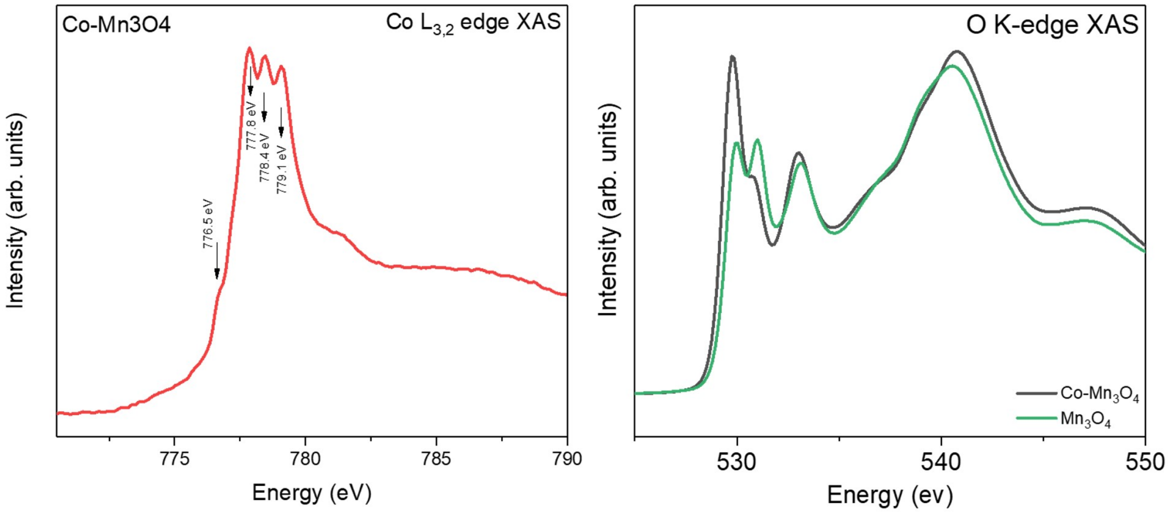

FIGURE 7.7. XAS spectra for doped and undoped Mn_3O_4 film. (a) Co L2,3 edge. (b) O K-edge.

As in previous samples, a resonance analysis on the doped film was performed. This time the Co 2*p* threshold energies seen in the XAS spectrum were used. All spectra were calibrated using Au 4*f* (84 eV) as reference and the background was removed using a linear fitting. Mn 3p and O 2*p* are identified at 48.1 and 21.8 eV, respectively. As expected, the intensity increase occurs at the 3.5 eV point and in the hybridized state, 7 eV.

Taking into account the small amount of cobalt in the film, it is not possible to identify large differences in the photoemission spectra. We chose for a comparison between spectra in the valence band region measured with the most resonant threshold energy of Co (777.7 eV) and Mn (640.5 eV). We expect the resonance process to occur at different points according to the orbitals of each element as seen in figure 7.9 (left panel). Since the beginning of the valence band of Au begins approximately from 2 eV, the contribution located at 2.1 eV must belong purely to the film, specifically at the 3*d* level of Mn (t_{2g}) or Co. Since the contribution of the Co (3+) should be located close to 2 eV. The Mn 3*d* (e_g state) is sighted at 3.5 eV.

We note that the black spectrum measured with Co 2p energy is thicker compared to the green spectrum measured with Mn 2*p*, as well as the shoulder near 6 eV. If it is a new contribution (marked at 4.7 eV with a red dotted line) that appears only with Co 2*p*, this means that it is a resonant state of cobalt. And according to this reference [121] the Co (2+) state should be located

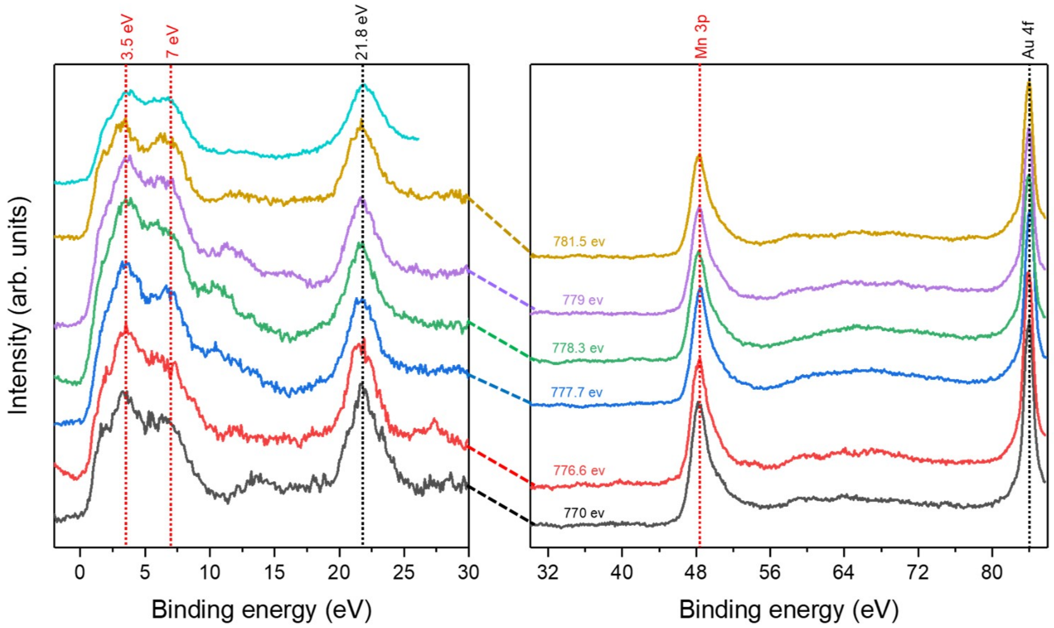

FIGURE 7.8. ResPE spectra normalized of doped Mn_3O_4 film measured at several energies. The spectra is separated in two regions.

near 4.5 eV.

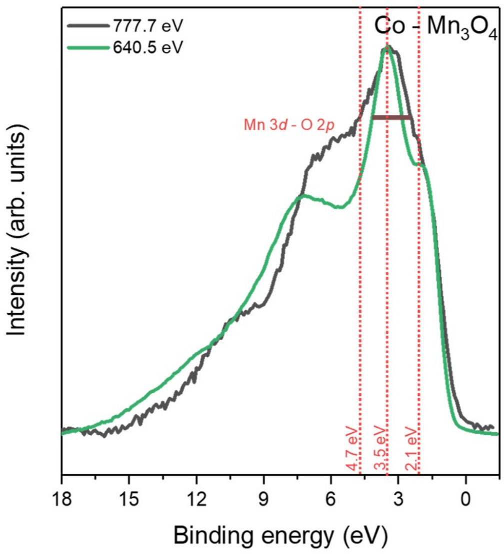

FIGURE 7.9. Resonance spectra of Co doping Mn_3O_4 measured with different energies.

Partial conclusions

Our first four samples (doped film preparation) were not effective due to cobalt desorption. In our fifth sample we managed to measure Co by XPS after one more long deposition without LEED results. We then discovered (XPS) that there is an overlap between Co LMM auger with Mn 2p. To avoid this inconvenience we decided to change the substrate from Cu (111) to Au (111). In sample 6 (with Au substrate) we used the cobalt encapsulation recipe between layers of manganese oxide. The XPS spectrum showed the existence of Co in the form of Co_3O_4 and the LEED results showed no variation with an undoped sample. The phase found is 001.

XPS results showed the formation of Mn3O4. Co 2p HR core level has the contribution of two states 2+ and 3+. With the 2+ state being more dominant because of the appearance of the satellite near 785 eV characteristic of CoO (2+). For LEED, we estimated the lattice parameter of 5.6 Å. This value is less than the 5.8 Å found for a non-doped film. O 1s core level showed an increase in vacancies from 5.6 to 10.4 %.

XAS for Co L-edge show that Co is located in the tetrahedral sites. This corroborates the formation of Co_3O_4. Due to the low amount of cobalt, we cannot see big differences in the resonance photoemission. But in the comparison of spectra between the energies of 777.7 and 640.5 eV (two more resonant energies for each threshold: Co and Mn). We see that the peak is maintained at 3.5 eV, the contribution at 2.1 eV and a shoulder at 4.7 eV that is part of Co 2*p* (resonant state of cobalt).

CHAPTER 8

GENERAL CONCLUSIONS AND FUTURE PROSPECTS

We have successfully fabricated MnO and Mn_3O_4 thin films deposited on Cu (111) surface to explore their electronic properties by electron photoemission spectroscopy.

We deposit MnO at p(O_2): 5×10−8 mbar at room temperature but with different thickness through the EBE technique. The characterization was made by various techniques at the CBPF and LNLS synchrotron laboratories. XPS measurements allowed us to understand that all films have the same oxidation state (2+), while LEED indicated the existence of two phases: (001) and (110). UPS results also show the valence band features for MnO and Cu for thin and thick film. XAS experiment has exposed a partial contamination of the substrate, i.e. we have copper oxide at surface. For film results we saw the differences for XAS results as a function of angle and thickness. The resonance spectra confirms the presence of oxygen in the substrate. We discovered that the peak at 3.5 eV is the T_{2g} state of Mn.

Mn_3O_4 films were deposited at p(O_2): 5×10−7 mbar at RT as a function of thickness. All spectra were confirmed with mixed oxidation state (2+ and 3+) through Mn 3*s* core level. Unlike MnO, we observed only one surface structure (110) but with different reconstruction: for thin films (1x1) and for thick films (2x2).

Another phase was found in LNLS experiments for Mn_3O_4 films. The new phase (001) show a different LEED pattern. We made a comparison between phases and no change was observed through XAS. Due to the film thin thickness with phase (110), not good results were obtained from the resonance experiment. Because that only the phase (001) has been shown.

Samples doped with cobalt were obtained after several failed attempts where the substrate, temperature and thickness of the film were important factors at the time of deposition and formation of film. To prevent cobalt from being evaporated, our strategy was encapsulate a cobalt within Mn_3O_4 layer follow by a post-annealing step. Interestingly our results indicate, according to XPS, that the oxidation state formed seems to be Co_3O_4, and LEED results does not show a change in its structure, eliminating the possibility of a mixed oxide. The lattice parameter has been reduced for the doped film. The number of oxygen vacancies has increased for doped films according to XPS.

As future prospects we hope to complete and go one step further than cobalt doping. By completing we refer to the preparation of some more samples varying the thickness of the film and Co doping. Finding precisely how much Co deposited is considered doping or mixed oxide (by LEED).

We would like to test the high temperature stability properties by Temperature programmed desorption (TPD). Also test how our system reacts to gases such as CO_2 in a high temperature environment, see if there is a reduction of CO_2 in other compounds such as CO or H_2O.

BIBLIOGRAPHY

[1] W. W. Fischer, J. Hemp, and J. E. Johnson., “Manganese and the evolution of photosynthesis,” *Origins of Life and Evolution of Biospheres*, vol. 45, no. 3, pp. 351–357, 2015.

[2] G. W. Brudvig., “Water oxidation chemistry of photosystem ii,” *Philosophical Transactions of the Royal Society B: Biological Sciences*, vol. 363, no. 1494, pp. 1211–1219, 2008.

[3] A. Pirson., “Ernahrungs-und stoffwechselphysiologische untersuchungen an fontinalis und chlorella,” *Z Bot*, vol. 31, pp. 193–267, 1937.

[4] A. K. Kundu, S. Barman, and K. S. Menon., “Stabilization of polar mn3o4 (001) film on ag (001): Interplay between kinetic and structural stability,” *Surface Science*, vol. 664, pp. 207–215, 2017.

[5] N. S. Lewis and D. G. Nocera., “Powering the planet: Chemical challenges in solar energy utilization,” *Proceedings of the National Academy of Sciences*, vol. 103, no. 43, pp. 15729–15735, 2006.

[6] G. W. Huber, S. Iborra, and A. Corma., “Synthesis of transportation fuels from biomass: chemistry, catalysts, and engineering,” *Chemical Reviews*, vol. 106, no. 9, pp. 4044–4098, 2006.

[7] R. Cogdell, T. Brotosudarmo, A. Gardiner, P. Sanchez, and L. Cronin., “Artificial photosynthesis - solar fuels: current status and future prospects,” *Biofuels*, vol. 1, no. 6, pp. 861–876, 2010.

[8] K. N. Ferreira, T. M. Iverson, K. Maghlaoui, J. Barber, and S. Iwata., “Architecture of the photosynthetic oxygen-evolving center,” *Science*, vol. 303, no. 5665, pp. 1831–1838, 2004.

[9] J. Messinger, J. H. Robblee, U. Bergmann, C. Fernandez, P. Glatzel, H. Visser, R. M. Cinco, K. L. McFarlane, *et al.*, “Absence of mn-centered oxidation in the s2 → s3 transition: Implications for the mechanism of photosynthetic water oxidation,” *Journal of the American Chemical Society*, vol. 123, no. 32, pp. 7804–7820, 2001.

[10] C. Ling and R. Zhang, “Manganese dioxide as rechargeable magnesium battery cathode,” *Frontiers in Energy Research*, vol. 5, 2017.

[11] K. Kordesch and W. Taucher-Mautner, “Primary batteries – aqueous systems | leclanché and zinc–carbon,” in *Encyclopedia of Electrochemical Power Sources* (J. Garche, ed.), pp. 43–54, Amsterdam: Elsevier, 2009.

[12] M. Pozin and S. Wicelinski, “Chapter 4 - safety aspects of lithium primary batteries,” in *Electrochemical Power Sources: Fundamentals, Systems, and Applications* (J. Garche and K. Brandt, eds.), pp. 83–111, Elsevier, 2019.

[13] K. Nishio, “Primary batteries – nonaqueous systems | lithium–manganese dioxide,” in *Encyclopedia of Electrochemical Power Sources* (J. Garche, ed.), pp. 83–92, Amsterdam: Elsevier, 2009.

[14] H. Kung, *Transition Metal Oxides: Surface Chemistry and Catalysis*.
Studies in Surface Science and Catalysis, Elsevier Science, 1989.

[15] C. N. R. Rao and G. V. Subba Rao, *Transition Metal Oxides: Crystal Chemistry, Phase Transition, and Related Aspects*.
No. 49 in NSRDS-NBS, Washington, DC : United States Government Printing Office, 1974.

[16] P. Poizot, S. Laruelle, S. Grugeon, L. Dupont, and J. M. Tarascon, “Nano-sized transition-metal oxides as negative-electrode materials for lithium-ion batteries,” vol. 407, pp. 496–499, 2000.

[17] A. Pareek and S. Venkata Mohan, “Chapter 1.4 - graphene and its applications in microbial electrochemical technology,” in *Microbial Electrochemical Technology* (S. V. Mohan, S. Varjani, and A. Pandey, eds.), Biomass, Biofuels and Biochemicals, pp. 75–97, Elsevier, 2019.

[18] H.-Y. Su, Y. Gorlin, I. C. Man, F. Calle-Vallejo, J. K. Nørskov, T. F. Jaramillo, and J. Rossmeisl., “Identifying active surface phases for metal oxide electrocatalysts: a study of manganese oxide bi-functional catalysts for oxygen reduction and water oxidation catalysis,” *Phys. Chem. Chem. Phys.*, vol. 14, pp. 14010–14022, 2012.

[19] T. Ogasawara, A. Débart, M. Holzapfel, P. Novák, and P. G. Bruce., “Rechargeable li2o2 electrode for lithium batteries,” *Journal of the American Chemical Society*, vol. 128, no. 4, pp. 1390–1393, 2006.

[20] F. Müller, R. Masi, D. Reinicke, P. Steiner, S. Hüfner, and K. Stöwe., “Epitaxial growth of mno/ag(001) films,” *Surface Science*, vol. 520, p. 158, 2002.

[21] F. Kapteijn, L. Singoredjo, A. Andreini, and J. Moulijn., “Activity and selectivity of pure manganese oxides in the selective catalytic reduction of nitric oxide with ammonia,” *Applied Catalysis B: Environmental*, vol. 3, no. 2, pp. 173 – 189, 1994.

[22] B. Gillot, M. EL Guendouzi, and M. Laarj., “Particle size effects on the oxidation–reduction behavior of mn3o4 hausmannite,” *Materials Chemistry and Physics*, vol. 70, pp. 54–60, 2001.

[23] Z. Gui, R. Fan, W. Mo, X. Chen, L. Yang, and Y. Hu., “Synthesis and characterization of reduced transition metal oxides and nanophase metals with hydrazine in aqueous solution,” *Materials Research Bulletin*, vol. 38, no. 1, pp. 169 – 176, 2003.

[24] A. K. Kundu and K. S. Menon., “Growth and characterization of ultrathin epitaxial mno film on ag(001),” *Journal of Crystal Growth*, vol. 446, pp. 85 – 91, 2016.

[25] B. Piriou, J. Dexpert-Ghys, and S. Mochizuki., “Time-resolved-photoluminescence spectra of mno and mns,” *Journal of Physics: Condensed Matter*, vol. 6, p. 7317, 1999.

[26] H. Osgood, S. V. Devaguptapu, H. Xu, J. Cho, and G. Wu, “Transition metal (fe, co, ni, and mn) oxides for oxygen reduction and evolution bifunctional catalysts in alkaline media,” *Nano Today*, vol. 11, no. 5, pp. 601–625, 2016.

[27] A. Omidvar, “Catalytic role of transition metals supported on niobium oxide in o2 activation,” *Applied Surface Science*, vol. 434, pp. 1239–1247, 2018.

[28] A. Singh and L. Spiccia, “Water oxidation catalysts based on abundant 1st row transition metals,” *Coordination Chemistry Reviews*, vol. 257, no. 17, pp. 2607–2622, 2013.
40th International Conference on Coordination Chemistry, Valencia, Spain, Sept. 9-13th 2012.

[29] S. Royer and D. Duprez, “Catalytic oxidation of carbon monoxide over transition metal oxides,” *ChemCatChem*, vol. 3, no. 1, pp. 24–65, 2011.

[30] P. Deshlahra, “Chemical functionality of oxide surfaces,” in *Encyclopedia of Interfacial Chemistry* (K. Wandelt, ed.), pp. 553–559, Oxford: Elsevier, 2018.

[31] H.-J. Freund, B. Dillmann, O. Seiferth, G. Klivenyi, M. Bender, D. Ehrlich, I. Hemmerich, and D. Cappus., “Molecules on oxide surfaces,” *Catalysis Today*, vol. 32, no. 1, pp. 1 – 10, 1996.

[32] F. S. Galasso, *Structure and properties of inorganic solids*.
Pergamon Press Oxford, New York, 1st ed., 1970.

[33] K. Gillmeister, M. Huth, R. Shantyr, M. Trautmann, K. Meinel, A. Chasse, K.-M. Schindler, H. Neddermeyer, and W. Widdra., “Mn$_3$o$_4$(001) film growth on ag(001) - a systematic study using nexafs, stm, and leed,” 2015.

[34] E. A. Soares, R. Paniago, V. De Carvalho, E. Lopes, G. Abreu, and H.-D. Pfannes., "Quantitative low-energy electron diffraction analysis of mno (100) films grown on ag (100)," *Physical Review B*, vol. 73, no. 3, p. 035419, 2006.

[35] M. Nagel, I. Biswas, H. Peisert, and T. Chassé., "Interface properties and electronic structure of ultrathin manganese oxide films on ag(001)," *Surface Science*, vol. 601, no. 18, pp. 4484 – 4487, 2007.

[36] A. Chassé, C. Langheinrich, F. Müller, and S. Hüfner., "Growth and structure of thin mno films on ag(001) in dependence on film thickness," *Surface Science*, vol. 602, no. 2, pp. 597 – 606, 2008.

[37] A. Chassé, C. Langheinrich, M. Nagel, and T. Chassé, "Photoelectron diffraction studies of ag(001), mno(001) and epitaxial mno films," *Surface Science*, vol. 605, no. 3, pp. 272–281, 2011.

[38] L. Zhang, Z. Tang, S. Wang, D. Ding, M. Chen, and H. Wan., "A synthetic mn4ca-cluster mimicking the oxygen-evolving center of photosynthesis," *Surface Science*, vol. 606, no. 19, pp. 1507 – 1511, 2012.

[39] H. Nishimura, T. Tashiro, T. Fujitani, and J. Nakamura., "Surface structure of mno/rh(100) studied by scanning tunneling microscopy and low-energy electron diffraction," *Journal of Vacuum Science & Technology A*, vol. 18, no. 4, pp. 1460–1463, 2000.

[40] C. Hagendorf, S. Sachert, B. Bochmann, K. Kostov, and W. Widdra., "Growth, atomic structure, and vibrational properties of mno ultrathin films on pt(111)," *Phys. Rev. B*, vol. 77, p. 075406, 2008.

[41] G. Rizzi, M. Petukhov, M. Sambi, R. Zanoni, L. Perriello, and G. Granozzi., "An x-ray photoelectron diffraction structural characterization of an epitaxial mno ultrathin film on pt(111)," *Surface Science*, vol. 482, pp. 1474–1480, 2001.

[42] F. Li, G. Parteder, F. Allegretti, C. Franchini, R. Podloucky, S. Surnev, and F. Netzer., "Two-dimensional manganese oxide nanolayers on pd(100): The surface phase diagram," *Journal of physics. Condensed matter : an Institute of Physics journal*, vol. 21, p. 134008, 2009.

[43] F. Allegretti, C. Franchini, V. Bayer, M. Leitner, G. Parteder, B. Xu, A. Fleming, M. G. Ramsey, R. Podloucky, S. Surnev, and F. P. Netzer., "Epitaxial stabilization of mno(111) overlayers on a pd(100) surface," *Phys. Rev. B*, vol. 75, p. 224120, 2007.

[44] V. Bayer, R. Podloucky, C. Franchini, F. Allegretti, B. Xu, G. Parteder, M. G. Ramsey, S. Surnev, and F. P. Netzer., "Formation of mn_3o_4(001) on mno(001): Surface and interface structural stability," *Phys. Rev. B*, vol. 76, p. 165428, 2007.

[45] C. Mӧller, J. Barreto, F. Stavale, and N. Niliu.s, “Manganese oxide thin films on au (111): Growth competition between mno and mn3o4,” *The Journal of Physical Chemistry C*, vol. 123, no. 13, pp. 7665–7672, 2018.

[46] J. Barreto, “Estudo do crescimento de filmes finos de mno e mn3o4 sobre substrato de au(111),” Master’s thesis, Centro Brasilero de Pesquisas Físicas, 2018.

[47] E. S. Ilton, J. E. Post, P. J. Heaney, F. T. Ling, and S. N. Kerisit, “Xps determination of mn oxidation states in mn (hydr)oxides,” *Applied Surface Science*, vol. 366, pp. 475–485, 2016.

[48] V. D. Castro and G. Polzonetti., “Xps study of mno oxidation,” *Journal of Electron Spectroscopy and Related Phenomena*, vol. 48, no. 1, pp. 117 – 123, 1989.

[49] J. Van Elp, R. Potze, H. Eskes, R. Berger, and G. Sawatzky., “Electronic structure of mno,” *Physical Review B*, vol. 44, no. 4, p. 1530, 1991.

[50] V. Galakhov, M. Falub, S. Bartkowski, M. Neumann, N. Ovechkina, E. Kurmaev, N. Lobachevskaya, Y. Mukovskii, J. Mitchell, and D. Ederer., “Mn 3s exchange splitting in mixed-valence manganites,” *Physical Review B*, vol. 65, p. 113102, 2002.

[51] P. S. Bagus, R. Broer, and E. S. Ilton, “A new near degeneracy effect for photoemission in transition metals,” *Chemical Physics Letters*, vol. 394, no. 1, pp. 150–154, 2004.

[52] M. C. Biesinger, B. P. Payne, A. P. Grosvenor, L. W. Lau, A. R. Gerson, and R. S. Smart, “Resolving surface chemical states in xps analysis of first row transition metals, oxides and hydroxides: Cr, mn, fe, co and ni,” *Applied Surface Science*, vol. 257, no. 7, pp. 2717–2730, 2011.

[53] K. Momma and F. Izumi., “*VESTA3* for three-dimensional visualization of crystal, volumetric and morphology data,” *Journal of Applied Crystallography*, vol. 44, no. 6, pp. 1272–1276, 2011.

[54] M. Bonfante, B. Hennion, F. Moussa, and G. Pepy., “Spin waves in mno at 4.2°k,” *Solid State Communications*, vol. 10, no. 6, pp. 553 – 556, 1972.

[55] G. Renaud and A. Barbier, “Chapter 6 - atomic structure of oxide surfaces by surface x-ray scattering,” *The Chemical Physics of Solid Surfaces*, vol. 9, pp. 256–300, 2001.

[56] A. K. Kundu and K. S. R. Menon, “Structural and electronic properties of polar mno ultrathin film grown on ag(111),” *AIP Conference Proceedings*, vol. 1731, no. 1, p. 080042, 2016.

[57] C. Franchini, V. Bayer, R. Podloucky, G. Parteder, S. Surnev, and F. P. Netzer, “Density functional study of the polar MnO(111) surface,” *Phys. Rev. B*, vol. 73, p. 155402, Apr 2006.

[58] M. A. Langell, C. W. Hutchings, G. A. Carson, and M. H. Nassir, “High resolution electron energy loss spectroscopy of mno(100) and oxidized mno(100),” *Journal of Vacuum Science & Technology A*, vol. 14, no. 3, pp. 1656–1661, 1996.

[59] T. Suzuki and T. Katsufuji, “Magnetodielectric properties of spin-orbital coupled system mn$_3$o$_4$,” *Phys. Rev. B*, vol. 77, p. 220402, Jun 2008.

[60] M. Kim, X. M. Chen, Y. I. Joe, E. Fradkin, P. Abbamonte, and S. L. Cooper, “Mapping the magnetostructural quantum phases of mn$_3\mathbf{o}_4$,” *Phys. Rev. Lett.*, vol. 104, p. 136402, Mar 2010.

[61] R. Roque-Malherbe, *The physical chemistry of materials: Energy and environmental applications*.
CRC Press, 2016.

[62] J.-X. Feng, S.-H. Ye, X.-F. Lu, Y.-X. Tong, and G.-R. Li, “Asymmetric paper supercapacitor based on amorphous porous mn3o4 negative electrode and ni(oh)2 positive electrode: A novel and high-performance flexible electrochemical energy storage device,” *ACS Applied Materials & Interfaces*, vol. 7, no. 21, pp. 11444–11451, 2015.
PMID: 25961565.

[63] G. Jin, X. Xiao, S. Li, K. Zhao, Y. Wu, D. Sun, and F. Wang, “Strongly coupled graphene/mn3o4 composite with enhanced electrochemical performance for supercapacitor electrode,” *Electrochimica Acta*, vol. 178, pp. 689–698, 2015.

[64] J. B. Goodenough and A. L. Loeb, “Theory of ionic ordering, crystal distortion, and magnetic exchange due to covalent forces in spinels,” *Phys. Rev.*, vol. 98, pp. 391–408, Apr 1955.

[65] L. Ren, S. Wu, M. Yang, W. Zhou, and S. Li, “Magnetic properties of mn3o4 film under compressive stress grown on mgal2o4 (001) by molecular beam epitaxy,” *Journal of Applied Physics*, vol. 114, no. 5, p. 053907, 2013.

[66] L. Ren, M. Yang, W. Zhou, S. Wu, and S. Li, “Influence of stress and defect on magnetic properties of mn3o4 films grown on mgal2o4 (001) by molecular beam epitaxy,” *The Journal of Physical Chemistry C*, vol. 118, no. 1, pp. 243–249, 2014.

[67] P. Gilbert, B. Frazer, A. Belz, P. Conrad, K. Nealson, D. Haskel, J. Lang, G. Srajer, and P. Gilbert, “Multiple scattering calculations of bonding and x-ray absorption spectroscopy of manganese oxides,” *J. Phys. Chem. A*, vol. 107, 2010.

[68] L. Laffont and P. Gibot., “High resolution electron energy loss spectroscopy of manganese oxides: Application to mn3o4 nanoparticles,” *Materials Characterization*, vol. 61, no. 11, pp. 1268 – 1273, 2010.

[69] K. Reichelt., “Influence of substrate temperature, deposition rate and surface conditions on the epitaxial growth of copper on mica,” *Surface Science*, vol. 36, no. 2, pp. 725 – 738, 1973.

[70] M. Mansoor, M. Ebadi, M. Mazhar, N. Huang, L. Mun, M. Misran, and W. Basirun, “Cadmium-manganese oxide composite thin films: Synthesis, characterization and photoelectrochemical properties,” *Materials Chemistry and Physics*, vol. 186, pp. 286–294, 2017.

[71] T. Larbi, A. Amara, L. Ben Said, B. Ouni, M. Haj Lakhdar, and M. Amlouk, “A study of optothermal and ac impedance properties of cr-doped mn3o4 sprayed thin films,” *Materials Research Bulletin*, vol. 70, pp. 254–262, 2015.

[72] M. A. Zamudio, N. Russo, and D. Fino., “Low temperature nh3 selective catalytic reduction of nox over substituted mncr2o4 spinel-oxide catalysts,” *Industrial & Engineering Chemistry Research*, vol. 50, no. 11, pp. 6668–6672, 2011.

[73] P. V. Samant and J. B. Fernandes., “Nickel-modified manganese oxide as an active electrocatalyst for oxidation of methanol in fuel cells,” *Journal of Power Sources*, vol. 79, no. 1, pp. 114 – 118, 1999.

[74] S. Ching, J. R. Carmichael, L. A. Eichelberger, D. A. Kriz, K. A. Alley, and S. E. Jackvony, “Influence of fe, cu, v, and ce doping on morphology and catalytic activity of amorphous manganese oxide hollow spheres,” *Polyhedron*, vol. 114, pp. 205–212, 2016.
Undergraduate Research in Inorganic Chemistry.

[75] D. Yang., “Pulsed laser deposition of cobalt-doped manganese oxide thin films for supercapacitor applications,” *Journal of Power Sources*, vol. 198, pp. 416 – 422, 2012.

[76] A. Jha, R. Thapa, and K. Chattopadhyay., “Structural transformation from mn3o4 nanorods to nanoparticles and band gap tuning via zn doping,” *Materials Research Bulletin*, vol. 47, no. 3, pp. 813 – 819, 2012.

[77] T. Gu, R. Jin, Y. Liu, H. Liu, X. Weng, and Z. Wu., “Promoting effect of calcium doping on the performances of mnox/tio2 catalysts for no reduction with nh3 at low temperature,” *Applied Catalysis B: Environmental*, vol. 129, pp. 30 – 38, 2013.

[78] T. Yoshinaga, M. Saruyama, A. Xiong, Y. Ham, Y. Kuang, R. Niishiro, S. Akiyama, M. Sakamoto, T. Hisatomi, K. Domen, and T. Teranishi, “Boosting photocatalytic overall

water splitting by co doping into mn3o4 nanoparticles as oxygen evolution cocatalysts," *Nanoscale*, vol. 10, pp. 10420–10427, 2018.

[79] T. R. Paudel, A. Zakutayev, S. Lany, M. d'Avezac, and A. Zunger, "Doping rules and doping prototypes in a2bo4 spinel oxides," *Advanced Functional Materials*, vol. 21, no. 23, pp. 4493–4501, 2011.

[80] "Transition metals." `https://jackwestin.com/resources/mcat-content/the-periodic-table-classification-of-elements-into-groups-by-electronic-structure/transition-metals`.
Accessed: 2021-10-21.

[81] H. Song and U. S. Ozkan., "Changing the oxygen mobility in co/ceria catalysts by ca incorporation: Implications for ethanol steam reforming," *The Journal of Physical Chemistry A*, vol. 114, no. 11, pp. 3796–3801, 2010.

[82] L. Xue, H. He, C. Liu, C. Zhang, and B. Zhang., "Promotion effects and mechanism of alkali metals and alkaline earth metals on cobalt- cerium composite oxide catalysts for n2o decomposition," *Environmental science & technology*, vol. 43, no. 3, pp. 890–895, 2009.

[83] A. Grupioni, E. Arashiro, and T. Lassali., "Voltammetric characterization of an iridium oxide-based system: the pseudocapacitive nature of the ir0.3mn0.7o2 electrode," *Electrochimica Acta*, vol. 48, no. 4, pp. 407 – 418, 2002.

[84] M.-T. Lee, J.-K. Chang, W.-T. Tsai, and C.-K. Lin., "In situ x-ray absorption spectroscopic studies of anodically deposited binary mn–fe mixed oxides with relevance to pseudocapacitance," *Journal of Power Sources*, vol. 178, no. 1, pp. 476 – 482, 2008.

[85] J.-K. Chang, M.-T. Lee, C.-H. Huang, and W.-T. Tsai., "Physicochemical properties and electrochemical behavior of binary manganese–cobalt oxide electrodes for supercapacitor applications," *Materials Chemistry and Physics*, vol. 108, no. 1, pp. 124 – 131, 2008.

[86] X. Han, T. Zhang, J. Du, F. Cheng, and J. Chen., "Porous calcium–manganese oxide microspheres for electrocatalytic oxygen reduction with high activity," *Chem. Sci.*, vol. 4, pp. 368–376, 2013.

[87] H. Lüth, *Solid Surfaces, Interfaces and Thin Films*.
Graduate Texts in Physics, Springer Berlin Heidelberg, 2010.

[88] S. Hüfner, *Photoelectron Spectroscopy: Principles and Applications*.
Springer Series in Solid-State Sciences, Springer Berlin Heidelberg, 2013.

[89] D. Vij, *Handbook of Applied Solid State Spectroscopy*.
Springer US, 2007.

[90] G. G. A. Holguin, S. Natividad, "X-ray photoelectron spectroscopy." `https://wiki.utep.edu/plugins/viewsource/viewpagesrc.action?pageId=51217510`.

[91] M. Russo, *Advances in Macromolecules: Perspectives and Applications*. SpringerLink : Bücher, Springer Netherlands, 2010.

[92] F. S. Roberts, S. L. Anderson, A. C. Reber, and S. N. Khanna., "Initial and final state effects in the ultraviolet and x-ray photoelectron spectroscopy (ups and xps) of size-selected pdn clusters supported on tio2(110)," *The Journal of Physical Chemistry C*, vol. 119, no. 11, pp. 6033–6046, 2015.

[93] R. J. Dallmeyer, C. Carbone, W. Eberhardt, C. Pampuch, O. Rader, W. Gudat, P. Gambardella, and K. Kern., "Electronic states and magnetism of monatomic Co and Cu wires," *Physical review / B*, vol. 61, p. R5133, 2000.

[94] S.-L. Liu., "Relations between photoionization cross sections and photon radius," *arXiv preprint arXiv:1611.04383*, 11 2016.

[95] M. VanHove, W. Weinberg, and C. Chan, *Low-Energy Electron Diffraction: Experiment, Theory and Surface Structure Determination*. Springer Series in Surface Sciences, Springer Berlin Heidelberg, 2012.

[96] H. Lüth, *Surfaces and Interfaces of Solid Materials*. Springer Study Edition, Springer Berlin Heidelberg, 2013.

[97] L. V. Goncharova, "Surface structure in real and reciprocal space," in *Basic Surfaces and their Analysis*, 2053-2571, pp. 3–1 to 3–16, Morgan and Claypool Publishers, 2018.

[98] D. E. Sayers, E. A. Stern, and F. W. Lytle., "New technique for investigating noncrystalline structures: Fourier analysis of the extended x-ray—absorption fine structure," *Physical review letters*, vol. 27, no. 18, p. 1204, 1971.

[99] T. Hayes and J. Boyce, "Extended x-ray absorption fine structure spectroscopy," in *Solid State Physics*, vol. 37, pp. 173–351, Elsevier, 1983.

[100] J. Stöhr and R. Gomer, *NEXAFS Spectroscopy*. Springer Series in Surface Sciences, Springer, 1992.

[101] D. Koningsberger and R. Prins, "X-ray absorption: principles, applications, techniques of exafs, sexafs, and xanes," 1988.

[102] C. Kumar, *Surface Science Tools for Nanomaterials Characterization*. Springer Berlin Heidelberg, 2015.

[103] M. R. Thuler, R. L. Benbow, and Z. Hurych., "Photoemission intensities at the $3p$ threshold resonance of nio and ni," *Phys. Rev. B*, vol. 27, pp. 2082–2088, 1983.

[104] G. Berner, M. Sing, H. Fujiwara, A. Yasui, Y. Saitoh, A. Yamasaki, Y. Nishitani, A. Sekiyama, N. Pavlenko, T. Kopp, *et al.*, "Direct k-space mapping of the electronic structure in an oxide-oxide interface," *Phys. Rev. Lett.*, vol. 110, p. 247601, 2013.

[105] M. Silly, F. Charra, F. Lux, G. Lemercier, and F. Sirotti., "The electronic properties of mixed valence hydrated europium chloride thin film," *Physical chemistry chemical physics : PCCP*, vol. 17, 2015.

[106] F. Mazzola, M. Nematollahi, Z. S. Li, S. Cooil, X. Yang, T. W. Reenaas, and J. W. Wells, "Resonant photoemission spectroscopy for intermediate band materials," *Applied Physics Letters*, vol. 107, no. 19, p. 192104, 2015.

[107] P. Jiang, D. Prendergast, F. Borondics, S. Porsgaard, L. Giovanetti, E. Pach, J. Newberg, H. Bluhm, F. Besenbacher, and M. Salmeron, "Experimental and theoretical investigation of the electronic structure of cu2o and cuo thin films on cu(110) using x-ray photoelectron and absorption spectroscopy," *The Journal of Chemical Physics*, vol. 138, no. 2, p. 024704, 2013.

[108] M. V. H. K.E. Hermann, "The software utility leedpat, version 4.2." `http://www.fhi-berlin.mpg.de/KHsoftware/LEEDpat/index.html`, 2014.

[109] C. Gattinoni and A. Michaelides, "Atomistic details of oxide surfaces and surface oxidation: the example of copper and its oxides," vol. 70, no. 3, pp. 424 – 447, 2015.

[110] J. Cezar, P. d. T. Fonseca, G. Rodrigues, A. Castro, R. Neuenschwander, F. Rodrigues, B. Meyer, L. Ribeiro, A. Moreira, J. Piton, M. Raulik, M. Donadio, R. Seraphim, M. Barbosa, A. De Siervo, R. Landers, and A. De Brito, "The u11 pgm beam line at the brazilian national synchrotron light laboratory," *Journal of Physics: Conference Series*, vol. 425, p. 072015, 03 2013.

[111] R. J. Lad and V. E. Henrich, "Electronic structure of mno studied by angle-resolved and resonant photoemission," *Phys. Rev. B*, vol. 38, pp. 10860–10869, Nov 1988.

[112] "NIST X-ray Photoelectron Spectroscopy Database, NIST Standard Reference Database Number 20, National Institute of Standards and Technology, Gaithersburg MD, 20899 (2000), howpublished = `http://dx.doi.org/10.18434/t4t88k`, note = Accessed: 2021-12-19."

[113] N. Fairley, V. Fernandez, M. R. Plouet, C. G. Deudon, J. Walton, E. Smith, D. Flahaut, M. Greiner, M. Biesinger, S. Tougaard, D. Morgan, and J. Baltrusaitis, "Systematic

and collaborative approach to problem solving using x-ray photoelectron spectroscopy," *Applied Surface Science Advances*, vol. 5, p. 100112, 2021.

[114] A. Audi and P. Sherwood, "Valence-band x-ray photoelectron spectroscopic studies of manganese and its oxides interpreted by cluster and band structure calculations," *Surface and Interface Analysis*, vol. 33, pp. 274 – 282, 03 2002.

[115] R. Ribeiro, S. de Lazaro, and S. Pianaro, "Density functional theory applied to magnetic materials: Mn3o4 at different hybrid functionals," *Journal of Magnetism and Magnetic Materials*, vol. 391, pp. 166–171, 2015.

[116] F. Lebreau, M. M. Islam, B. Diawara, and P. Marcus, "Structural, magnetic, electronic, defect, and diffusion properties of cr2o3: A dft+u study," *The Journal of Physical Chemistry C*, vol. 118, no. 31, pp. 18133–18145, 2014.

[117] H. Noura, "Gga+u–dft+u modeling structural, electronic and magnetic properties investigation on the ferromagnetic and anti-ferromagnetic bafeo3 characteristics: Insights from first-principle calculation," *Superlattices and Microstructures*, vol. 76, pp. 425–435, 2014.

[118] X. H. Tai, C. W. Lai, J. C. Juan, and K. M. Lee, "Chapter 7 - nanocatalyst-based catalytic oxidation processes," in *Nanomaterials for Air Remediation* (A. Abdeltif, A. A. Assadi, P. Nguyen-Tri, T. A. Nguyen, and S. Rtimi, eds.), Micro and Nano Technologies, pp. 133–150, Elsevier, 2020.

[119] "WebElements, howpublished =`https://www.webelements.com/index.html`, note = accessed February 2022.."

[120] S. C. Wi, J.-S. Kang, J. H. Kim, S.-B. Cho, B. J. Kim, S. Yoon, B. J. Suh, S. W. Han, K. H. Kim, K. J. Kim, B. S. Kim, H. J. Song, H. J. Shin, J. H. Shim, and B. I. Min, "Electronic structure of zn1−xcoxo using photoemission and x-ray absorption spectroscopy," *Applied Physics Letters*, vol. 84, no. 21, pp. 4233–4235, 2004.

[121] Y. Lykhach, S. Piccinin, T. Skála, M. Bertram, N. Tsud, O. Brummel, M. Farnesi Camellone, K. Beranová, A. Neitzel, S. Fabris, K. C. Prince, V. Matolín, and J. Libuda, "Quantitative analysis of the oxidation state of cobalt oxides by resonant photoemission spectroscopy," *The Journal of Physical Chemistry Letters*, vol. 10, no. 20, pp. 6129–6136, 2019.
PMID: 31553619.